THE UNIVERSITY OF CHICAGO

DYNAMICS OF EXTRATROPICAL STORM TRACKS ON DIFFERENT TIMESCALES

A DISSERTATION SUBMITTED TO
THE FACULTY OF THE DIVISION OF THE PHYSICAL SCIENCES
IN CANDIDACY FOR THE DEGREE OF
DOCTOR OF PHILOSOPHY

DEPARTMENT OF THE GEOPHYSICAL SCIENCES

BY
PRAGALLVA BARPANDA

CHICAGO, ILLINOIS
AUGUST 2020

To Ma and Bapa

"The astonishing thing about the Earth... is that it is alive... Aloft, floating free beneath the moist, gleaming membrane of bright blue sky, is the rising Earth, the only exuberant thing in this part of the cosmos... It has the organized, self-contained look of a live creature, full of information, marvelously skilled in handling the sun."

- Lewise Thomas, The Lives of a Cell

TABLE OF CONTENTS

LIST OF FIGURES

LIST OF TABLES

ACKNOWLEDGMENTS

First and foremost, I thank my advisors Tiffany Shaw and Noboru Nakamura for being the most wonderful mentors during my PhD journey. Tiffany played a major role during the formative years of my PhD. She was not only a great scientific advisor, but she also saw me through many highs and lows and understood when I needed her the most. I also consider myself fortunate to be advised by Noboru during the last year of my PhD. I learned a lot from his deep scientific insights on several topics of geophysical fluid dynamics. I am also thankful to the members of my committee, Malte Jansen and Dorian Abbot for shaping my research though their useful comments during committee meetings. I benefited greatly from their graduate courses and conversations during journal club meetings. I also thank the Department of Geophysical Sciences for providing a fun environment to learn and grow.

My PhD journey would have been incomplete without the support of my department friends, Zhihong, Todd, Orli, Osamu, Hailu, Lei, Clare and Predrag. I learned a great deal from them and enjoyed conversations in the department corridor on Friday evenings.

I am indebted to my parents, Ashok and Anusaya Barpanda for being a constant support throughout. Finally, I thank my best friend and husband, Tamaghna Hazra, who has been my most important pillar of support in this journey.

ABSTRACT

Extratropical storm tracks are collective paths of synoptic scale (~1000 km) cyclones (anticyclones) that exist in the midlatitudes of both hemispheres. Storm tracks shape the Earth's climate through their transport of energy, momentum and moisture. Locally, the eastward migrating cyclones within the storm track control the weather variability. Therefore, any changes to the storm track intensity and position or disruption in the eastward flow of extratropical cyclones will have important implications on the local and global climate. In this thesis we use atmosphere's energy and momentum budgets to understand how storm track respond to various climatic perturbations.

First, we develop a moist static energy framework for zonal-mean storm track that connects storm track position to external forcings like top-of-atmosphere radiation and surface fluxes. Using reanalysis dataset, we apply the framework to storm track shifts in response to seasonal insolation, El Nino Southern Oscillation and two hypothetical warming scenarios. We show that net energy input in the atmosphere is not a dominant contribution for storm track shifts across all timescales considered. The stationary eddy plays a dominant role in the Northern Hemisphere (NH) shifts in response to seasonal insolation, El Nino minus La Nina conditions and increased CO_2 over land. The mean meridional circulation also contribute to the shift in response to increased sea surface temperature during boreal winter. In contrast, the Southern Hemisphere (SH) storm track exhibits very small changes.

Next, we use the moist static energy framework to understand why zonal-mean storm tracks exhibit distinct hemispheric seasonality. We begin with an assumption that SH has higher heat capacity or effectively larger mixed layer depth due to greater ocean coverage than in the NH. We define a critical mixed layer depth d_c using scaling analysis and hypothesize that 1) large mixed layer depths ($d > d_c$) produce surface heat fluxes that are out of phase with shortwave absorption and 2) small mixed layer depths ($d < d_c$) produce surface heat fluxes that are in phase with shortwave absorption. Assuming MSE balance, storm track

seasonality must be small for large mixed layer depth and it should be large for small mixed layer depth. We test our hypotheses by varying the mixed layer depth in (1) a zonally symmetric slab-ocean aquaplanet with zero ocean energy transport and (2) a 1D energy balance model with fixed diffusivity. Our aquaplanet simulations confirm the large mixed layer depth hypothesis and yield a useful idealization of the SH storm track. However, the small mixed layer limit does not yield a useful idealization of the NH storm track due to unrealistic representation of Ferrel cell and large atmospheric storage. We corroborate our aquaplanet results with the energy balance model simulations. Overall, we establish the causal role of surface fluxes in damping the seasonality of SH storm track.

Finally, we focus on the question, why do storm tracks exhibit atmospheric blocking? Atmospheric blocking is a phenomena characterized by persistent meandering of the jet stream that often disrupt the eastward migration of extratropical cyclones and anticyclones. We use the finite-amplitude local wave activity (LWA) framework to identify signatures of traffic-jam mechanism during block formation. Using LWA budget and a feature tracking algorithm, we perform a careful analysis of major persistent anomalies in the jet streams during the NH winter in reanalysis data. We show that most of the persistent anomalies occur in clusters collocated with the quasi-stationary ridge over the Euro-Atlantic sector and the Pacific sector. In the Atlantic sector, the zonal LWA flux dominates for longer timescale (up to ~20 days), whereas in the Pacific sector, both diabatic heating and zonal LWA flux are equally important. Most persistent events are associated with stronger nonlinear modification of large-amplitude Rossby waves. In such cases the total LWA flux is effectively suppressed. In contrast, the short-lived anomalous events are associated with weaker nonlinear component of LWA flux which results in ineffective flux suppression. For both persistent and short-lived events the zonal LWA flux reaches a tipping point for spontaneous accumulation of LWA. Overall, we show that despite substantial variations among individual events most of the persistent events are consistent with the traffic jam mechanism.

CHAPTER 1

INTRODUCTION

Extratropical storm tracks are one of the most prominent features of the largescale atmospheric circulation in the Earth's midlatitudes (between 30° – 60° North and South) (Held, 2019). The storm tracks act as preferential regions for the midlatitude synoptic scale (~ 1000km) cyclones to grow, mature and decay on the 2-8 day timescale. The midlatitude cyclones are eastward migrating transient eddies whose speed and direction are controlled by the jet stream. In the Northern Hemisphere (NH), the storm tracks are localized over the Pacific and Atlantic sectors and in the Southern Hemisphere (SH), they form a roughly homogenous band over the Southern ocean (Hoskins & Hodges, 2002, 2005).

On the global scale, the storm tracks shape the Earth's climate through their transport of energy, momentum and moisture (Trenberth & Stepaniak, 2003a; Shaw *et al.*, 2016). Locally, the storm tracks control the day-to-day weather variability and lead to extreme temperature and precipitation events (Hawcroft *et al.*, 2012; Pfahl & Wernli, 2012). Therefore any changes to the storm track intensity and position will have serious implications on the local and global climate.

The most striking changes of the storm track occur in response to seasonal insolation. During winter, storm tracks are the most active and are shifted equatorward. During summer, they are weak and shifted poleward (Trenberth & Stepaniak, 2003a). However, the storm track seasonality is not symmetric between the two hemispheres. For example, the zonal-mean NH storm track exhibits ~ 13° poleward shift from winter to summer and the SH storm track exhibits < 3° shift (Barpanda & Shaw, 2017). Similar differences are observed for storm track intensity (Shaw *et al.*, 2018). Even though the Earth receives roughly the same solar radiation in both hemispheres, why do storm tracks exhibit such distinct seasonality in the NH and SH?

Previous works have attempted to address this question using thermodynamical frame-

works which identify storm tracks using maximum Eady growth rate (Nakamura, 1992; Chang *et al.*, 2002), isentropic slopes (Papritz & Spengler, 2015) or mean avalailable potential energy (MAPE) (O'Gorman, 2010; Mbengue & Schneider, 2013, 2017); all of which measure baroclinicity and are functions of mean meridional temperature gradient and static stability (vertical temperature gradient) (O'Gorman & Schneider, 2008). The thermodynamic frameworks thus posit that the stormtracks shift and weaken/strengthen as a result of changes in near surface mean temperature structure (O'Gorman, 2010). However, the causal connection between the mean temperature field and storm track is not straightforward as they both feedback on each other (Hoskins & Valdes, 1990; Shaw *et al.*, 2016). Additionally, these frameworks cannot connect radiation and surface fluxes to storm track intensity which ultimately drive changes in the storm track.

In addition to seasonal changes, storm tracks shift and weaken/strengthen in response to climate variability and forcings like El Nino Southern Oscillation (Seager *et al.*, 2003; Lu *et al.*, 2008) and increased CO_2 warming (McLandress *et al.*, 2011; Polvani *et al.*, 2011; Thompson *et al.*, 2011; Lee & Feldstein, 2013; Grise *et al.*, 2014). Previous studies attribute these changes to competing effects from radiative changes and dynamical feedback from the stationary circulation (Shaw *et al.*, 2016). However, no consensus has been reached on the processes that dominate the long-term storm track response.

On the other extreme, in synoptic timescales (few days to a week), internal dynamics of the storm tracks play an important role in controlling the midlatitude weather. Atmospheric blocking is one such phenomena in which the eastward migration of synoptic cyclones (anticyclones) is disrupted by persistent meandering of the jet streams (Rex, 1950; Woollings *et al.*, 2010; Berggren *et al.*, 1949). Such persistent events form nearly stationary anticyclones (cyclones) and often result in unusually high or cold temperatures in the midlatitudes and can have catastrophic impact on the society (Demirtaş, 2017).

It has long been understood that local nonlinear interaction between the high frequency

eddies and the background stationary waves play an important role for the formation and maintenance of atmospheric blocks (Berggren *et al.*, 1949; Green, 1977; Shutts, 1983; Colucci, 1985, 2001; Mullen, 1987; Altenhoff *et al.*, 2008). However, what conditions precisely lead to block formation is not well understood. The lack of a definitive theory for blocking onset and disagreement among blocking indices has led to several uncertainties about the frequency and distribution of atmosphere blocking in current and future climate states (Barnes *et al.*, 2014).

All the problems stated above are best resolved using frameworks that follow some conservation equations like the moist static energy (MSE) budget or the angular momentum budget. In chapters 2 and 3 we derive a moist static energy framework that connects storm track to top-of-atmosphere insolation. We use the MSE framework to address the questions above and test the hypotheses using reanalysis data and idealized model simulations.. In chapter 4 we examine the onset of atmospheric blocking in storm tracks using finite-amplitude local wave-activity framework (FAWA) which is based on the angular momentum budget. Each of the frameworks are discussed in detail in the relevant chapters. In what follows, we provide a brief summary of each chapter.

In Chapter 2, originally published as Barpanda & Shaw (2017), we formulate an MSE framework for storm track position and use it to understand storm track shifts in response to seasonal insolation, El Niño minus La Niña conditions, and direct (increased CO2 over land) and indirect (increased sea surface temperature) effects of increased CO_2. Two methods are developed to quantify storm track shifts and decompose them into contributions from net energy (energy input to the atmosphere minus atmospheric storage) and MSE transport by the mean meridional circulation and stationary eddies. We show that net energy is not a dominant contribution across the timescales considered. The stationary eddy contribution dominates the storm track shift in response to seasonal insolation, El Niño minus La Niña conditions, and CO_2 direct effect in the Northern Hemisphere. Whereas the mean meridional

circulation contribution dominates the shift in response to CO_2 indirect effect in the Northern Hemisphere during winter and in SH during May and October. Overall, the MSE framework shows that the seasonal storm track shift in the Northern Hemisphere is connected to the stationary eddy MSE flux evolution. We also show that the equatorward storm track shift in response to El Niño minus La Niña conditions during boreal winter involves a different regime than the poleward shift in response to increased CO_2 even though the tropical upper troposphere warms in both cases.

In Chapter 3, originally published as Barpanda & Shaw (2020), we use the MSE framework to explain why storm tracks exhibit hemispheric asymmetry in seasonal timescale. In a recent study, Shaw *et al.* (2018) use the MSE framework diagnostically to show that while shortwave absorption (insolation) govern the seasonal cycle of storm tracks, the surface heat fluxes damp the seasonality in the SH but amplify it in the NH. In this thesis, we establish the causal role of surface fluxes (ocean energy storage) by varying the mixed layer depth (d) in zonally symmetric 1) slab-ocean aquaplanet simulations with zero ocean energy transport and 2) energy balance model (EBM) simulations. Using scaling analysis we define a critical mixed layer depth d_c and hypothesize that 1) large mixed layer depths ($d > d_c$) produce surface heat fluxes that are out of phase with shortwave absorption resulting in small storm track seasonality and 2) small mixed layer depths ($d < d_c$) produce surface heat fluxes that are in phase with shortwave absorption resulting in large storm track seasonality. The aquaplanet simulations confirm the large mixed layer depth hypothesis and yield a useful idealization of the SH storm track. However, the small mixed layer depth hypothesis fails to account for the large contribution of the Ferrel cell and atmospheric storage. The small mixed layer limit does not yield a useful idealization of the NH storm track because the seasonality of the Ferrel cell contribution is opposite to the stationary eddy contribution in the NH. Varying the mixed layer depth in an EBM qualitatively supports the aquaplanet results.

In chapter 4, currently in preparation, we use the wave-activity budget to evaluate if persistent anomalies in the jet stream are formed by the traffic-jam mechanism. To that end, we test the three foundational principles of traffic-jam theory for all regions of Northern Hemisphere storm track. First, the column integrated LWA is driven by zonal convergence of LWA flux. Second, the LWA threshold which is a function of background stationary wave activity and nonlinear interaction strength, dictates the preferred locations of block formation. Third, once the threshold LWA is exceeded total LWA flux drops precipitously due to nonlinear modification of the flux by large amplitude waves. Consistent with Nakamura & Huang (2018), we find that the 1 day correlation between LWA and the convergence of zonal LWA flux is between 60-70% near the exit region of North Atlantic and North Pacific storm track suggesting that zonal convergence of LWA drives the LWA variance in synoptic timescales. Next, we show that the theoretically predicted LWA threshold qualitatively matches with the empirical estimates of LWA threshold except in the entrance region of North Pacific storm track. Using spatially varying LWA threshold and a feature-tracking algorithm to identify all the 'high LWA persistent events' and find them to be clustered in regions of maximum wave mean-flow interaction and minimum LWA threshold. All the 'persistent events' consistently exhibit a steep increase in the magnitude of nonlinear flux from the onset stage to the peak stage. This suggests the important role of Rossby-wave breaking in suppressing the total LWA flux and eventual jamming of large amplitude waves. However, the efficiency of flux suppression decreases with the decrease in persistence. Overall, we show that the most persistent events are good candidates of atmospheric blocks formed by traffic-jam mechanism.

Finally, in chapter 5, we summarize our results and conclude. Some of the notation is inconsistent between chapters 3 and 4. We chose to keep this notation in order to maintain consistency with the published papers.

CHAPTER 2

THE MOIST STATIC ENERGY FRAMEWORK TO UNDERSTAND STORM TRACK SHIFTS ACROSS A RANGE OF TIMESCALES

2.1 Introduction

Storm tracks dominate the extratropical circulation. They play a fundamental role in Earth's energy budget through their poleward energy flux, which alleviates the energy imbalance between the equator and the pole (Trenberth & Stepaniak, 2003a; Shaw *et al.*, 2016). In energy budget decompositions, storm track energy flux is isolated as transient eddy meridional moist static energy (MSE) flux with eddies defined as deviations from a monthly average (Peixoto & Oort, 1992; Trenberth & Stepaniak, 2003a). While there exist many climate-based definitions of storm tracks, including regions of maximum transient eddy surface pressure variance and transient eddy kinetic energy (Chang *et al.*, 2002), here we focus on transient eddy MSE flux and define storm track position as the extremum of area-weighted transient eddy MSE flux (zero flux divergence).

Storm tracks shift meridionally in response to forcing across a range of timescales. Seasonally the storm track shifts meridionally in the Northern Hemisphere (NH) but very little in the Southern Hemisphere (SH) (see Fig. 6 in Trenberth & Stepaniak, 2003a). Interannually, storm tracks shift equatorward in response to El Nino minus La Nina conditions (Seager *et al.*, 2003; Lu *et al.*, 2008). On decadal timescales, ozone depletion shifts the SH storm track poleward (McLandress *et al.*, 2011; Polvani *et al.*, 2011; Thompson *et al.*, 2011; Lee & Feldstein, 2013; Grise *et al.*, 2014) whereas ozone recovery is projected to shift it equatorward (Perlwitz *et al.*, 2008; Son *et al.*, 2008). Anthropogenic aerosols shift the NH storm track equatorward during boreal winter (Ming *et al.*, 2011). On centennial timescales anthropogenic climate change is projected to shift storm tracks poleward (Yin, 2005; Shaw

et al., 2016). Finally, on millennial timescales, the wintertime storm track was shifted equatorward relative to today during the mid-Holocene and Last Glacial Maximum (Brayshaw *et al.*, 2010; Li & Battisti, 2008). storm track intensity also changes in response to forcing (e.g. Chang, 2001; O'Gorman, 2010), however here we focus on storm track shifts.

What drives storm track shifts? Previous work focused on momentum budget, potential vorticity or eddy kinetic energy arguments. Examples include shifts due to changes in 1) Eady growth rate (Brayshaw *et al.*, 2008), 2) the subtropical jet (Son & Lee, 2005), 3) stratification (Lorenz & DeWeaver, 2007; Gerber & Son, 2014), 4) critical or reflection latitudes (Seager *et al.*, 2003; Chen & Held, 2007; Kidston & Vallis, 2012; Lorenz, 2014), 5) eddy diffusivity (Lu *et al.*, 2014), and 6) available potential energy (Mbengue & Schneider, 2013, 2017). These results represent significant advances in our understanding of storm track shifts.

A common theme amongst the shifts mentioned above is they are driven by energetic perturbations, e.g. seasonal insolation, changes in surface fluxes or top-of-atmosphere (TOA) radiation. An energetic framework is attractive for understanding storm track shifts because it connects energetic perturbations to a measure of storm track position (latitude of zero transient eddy MSE flux divergence). In the tropics, an MSE framework has been used to understand ITCZ shifts via its connection to the energy flux equator (EFE, latitude where MSE flux is zero in the tropics, Schneider *et al.*, 2014). Bischoff & Schneider (2014) derived an MSE framework for EFE shifts based on the Taylor series linearization of MSE flux about the equator. The framework has been applied to ITCZ shifts across timescales (Adam *et al.*, 2016a,b) as well as to aquaplanet models with idealized perturbations (Bischoff & Schneider, 2014; Shaw *et al.*, 2015; Bischoff & Schneider, 2016). Here we derive an MSE framework for storm track position and use it to understand storm track shifts across a range of timescales. We apply it to storm track shifts in response to seasonal insolation, El Nino minus La Nina conditions and increased CO_2. The response to increased CO_2 is decomposed into direct (increased CO_2 with fixed sea surface temperature or SST) and indirect (increased SST with

fixed CO_2) contributions using an Atmospheric General Circulation Model (AGCM). Our goal is to understand 1) why seasonal storm track shifts are larger in the NH than in SH and 2) why storm tracks shift equatorward in response to El Nino minus La Nina conditions but poleward in response to increased CO_2 even though the tropical upper troposphere warms in both cases. The chapter is organized as follows. We derive the MSE framework and describe the data sets in section 2. Our results for seasonal, interannual and centennial storm track shifts are presented in section 3. The conclusions and discussion are summarized in section 4.

2.2 Energetic framework and datasets

2.2.1 Energetic framework

We investigate storm track shifts using the atmospheric MSE budget. The time, zonally averaged and vertically integrated atmospheric MSE budget is

$$\partial_t \langle [\overline{h}] \rangle + \partial_y \langle [\overline{vm}] \rangle = EIA \tag{2.1}$$

(Neelin & Held, 1987) where t is time, h is the thermal energy ($h = c_p T + Lq$ where c_p is the specific heat at constant pressure, T is temperature, L is latent heat of vaporization and q is specific humidity), m is the MSE ($m = c_p T + Lq + \Phi$ where Φ is geopotential), v is the meridional wind, $\bar{\cdot}$ and $[\cdot]$ denote monthly time and zonal averages, respectively, $\langle \cdot \rangle$ denotes a mass-weighted vertical integration and $\partial_y(\cdot) \equiv \partial_\phi(\cos\phi\,(\cdot))/a\cos\phi$ is the meridional divergence in spherical coordinates where ϕ is latitude and a is the radius of Earth. The MSE input to the atmosphere (EIA) is the difference between TOA and surface fluxes.

The MSE flux is decomposed into three contributions, i.e. $\langle [\overline{vm}] \rangle = \langle [\overline{v}][\overline{m}] \rangle + \langle [\overline{v}^*\overline{m}^*] \rangle + \langle [\overline{v'm'}] \rangle$ where $'$ and * denote deviations from the time and zonal average, respectively (Peixoto & Oort, 1992). Following the usual convention, we refer to the different contri-

butions as mean meridional circulation (MM, $\langle[\overline{v}][\overline{m}]\rangle$), stationary eddy (SE, $\langle[\overline{v}^*\overline{m}^*]\rangle$) and transient eddy (TE, $\langle[\overline{v'm'}]\rangle$). The dominant terms in the MSE flux are different across the contributions. The MM flux is dominated by potential energy, i.e. $\langle[\overline{v}][\overline{\Phi}]\rangle > c_p\langle[\overline{v}][\overline{T}]\rangle + L\langle[\overline{v}][\overline{q}]\rangle$ whereas for eddies (Rossby waves) thermal energy flux dominates, i.e. $c_p\langle[\overline{v}^*\overline{T}^*]\rangle + L\langle[\overline{v}^*\overline{q}^*]\rangle > \langle[\overline{v}^*\overline{\Phi}^*]\rangle$ and $c_p\langle[\overline{v'T'}]\rangle + L\langle[\overline{v'q'}]\rangle > \langle[\overline{v'\Phi'}]\rangle$, because they are mostly geostrophic (Figs. A1 and A2). According to the MSE flux decomposition the atmospheric MSE budget (2.1) can be written as

$$F_{MM} + F_{SE} + F_{TE} = \left(EIA - \partial_t\langle[\overline{h}]\rangle\right) \equiv F_{NE} \tag{2.2}$$

where F_{NE} is the net energy (difference between MSE input to the atmosphere and atmospheric MSE storage), and $F_{MM} = \partial_y\langle[\overline{v}][\overline{m}]\rangle$, $F_{SE} = \partial_y\langle[\overline{v}^*\overline{m}^*]\rangle$ and $F_{TE} = \partial_y\langle[\overline{v'm'}]\rangle$ represent the MSE flux divergence by the different circulation components.

We define storm track position as the latitude of zero transient eddy MSE flux divergence, i.e. the latitude ϕ_o where $F_{TE}|_{\phi_o} = 0$ and consider two methods for quantifying storm track shifts. The first method is motivated by previous work that derived an MSE framework for EFE shifts based on the Taylor series linearization of MSE flux about the equator (Bischoff & Schneider, 2014). Here we consider Taylor series linearization of the transient eddy MSE flux divergence about a reference latitude near the storm track position. The second method does not involve a Taylor series or reference latitude. Instead, changes in MSE flux divergence at all latitudes are added to the climatological transient eddy MSE flux divergence.

Method 1

Linearizing F_{TE} about a reference latitude ϕ_r near the storm track position ϕ_o we have

$$0 = F_{TE}|_{\phi_o} \approx F_{TE}|_{\phi_r} + a\partial_y F_{TE}|_{\phi_r}\delta \tag{2.3}$$

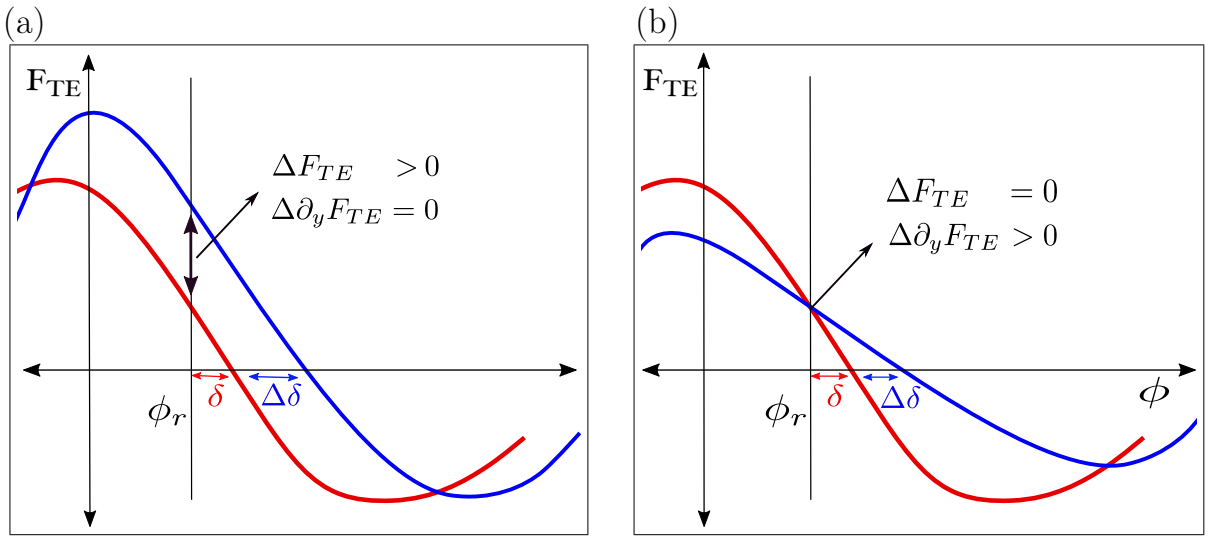

Figure 2.1: Schematic illustrating a storm track shift between two climates (red and blue) due to the first two terms of the linearized Taylor series framework [Method 1, (2.5)]. storm track shift $\Delta\delta$ due to a change in the (a) transient eddy MSE flux divergence (ΔF_{TE}) and (b) slope of transient eddy MSE flux divergence ($\Delta\partial_y F_{TE}$) at the reference latitude ϕ_r.

where $\delta = \phi_o - \phi_r$ such that the storm track position about a reference latitude δ is

$$\delta_1 = -\frac{1}{a}\frac{F_{TE}|_{\phi_r}}{\partial_y F_{TE}|_{\phi_r}}. \tag{2.4}$$

where the subscript indicates Method 1. Hence, the position of storm track is determined by the ratio of transient eddy MSE flux divergence and the slope of the flux divergence at the reference latitude. The denominator is negative definite in the NH and positive definite in the SH because the storm track represents a local maximum and minimum of area-weighted transient eddy MSE flux, respectively. The reference latitude is chosen to ensure the accuracy of the linearization (see Appendix C). Since the Taylor series linearization is accurate for latitudes near the storm track position we consider reference latitudes equal to the storm track position ± 1° in 0.5° increments and show the mean and standard deviation across that range.

A shift of storm track position is given by

$$\Delta\delta_1 = -\frac{1}{a}\frac{\Delta F_{TE}|_{\phi_r}}{\partial_y F_{TE}|_{\phi_r}} + \frac{1}{a}\frac{F_{TE}|_{\phi_r}\Delta\partial_y F_{TE}|_{\phi_r}}{(\partial_y F_{TE}|_{\phi_r})^2} + \frac{1}{a}\frac{\Delta F_{TE}|_{\phi_r}\Delta\partial_y F_{TE}|_{\phi_r}}{(\partial_y F_{TE}|_{\phi_r})^2}. \tag{2.5}$$

where the terms on the right-hand side represent 1) change in transient eddy MSE flux divergence, 2) change in the slope of transient eddy MSE flux divergence and 3) nonlinear change term. Figure 2.1 illustrates a shift of the NH storm track due to a change in the first two terms. Increased transient eddy MSE flux divergence at the reference latitude, i.e. $\Delta F_{TE}|_{\phi_r} > 0$, shifts the storm track poleward (Fig. 2.1a). Increased slope at the reference latitude, i.e. $\Delta\partial_y F_{TE}|_{\phi_r} > 0$, also induces a poleward shift (Fig. 2.1b).

The MSE budget provides a physical interpretation of storm track shifts. According to the MSE budget (2.2) a change in the transient eddy MSE flux divergence or slope of transient eddy MSE flux divergence is related to changes in net energy and the flux divergence by other circulation components, i.e. $\Delta F_{TE} = \Delta F_{NE} - \Delta F_{MM} - \Delta F_{SE}$ and $\Delta\partial_y F_{TE} = \Delta\partial_y F_{NE} - \Delta\partial_y F_{MM} - \Delta\partial_y F_{SE}$. Thus any storm track shift can be decomposed into contributions from net energy, mean meridional circulation, stationary eddies and a cross term (CT)

$$\Delta\delta_1 = \Delta\delta_{1,NE} + \Delta\delta_{1,MM} + \Delta\delta_{1,SE} + \Delta\delta_{1,CT} \tag{2.6}$$

where

$$\begin{aligned}\Delta\delta_{1,NE} = &-\frac{1}{a}\frac{\Delta F_{NE}|_{\phi_r}}{\partial_y F_{TE}|_{\phi_r}} + \frac{1}{a}\frac{F_{TE}|_{\phi_r}\Delta\partial_y F_{NE}|_{\phi_r}}{\left(\partial_y F_{TE}|_{\phi_r}\right)^2} \\ &+ \frac{1}{a}\frac{\Delta F_{NE}|_{\phi_r}\Delta\partial_y F_{TE}|_{\phi_r}}{\left(\partial_y F_{TE}|_{\phi_r}\right)^2},\end{aligned} \tag{2.7}$$

$$\Delta\delta_{1,MM} = + \frac{1}{a}\frac{\Delta F_{MM}|_{\phi_r}}{\partial_y F_{TE}|_{\phi_r}} - \frac{1}{a}\frac{F_{TE}|_{\phi_r}\Delta\partial_y F_{MM}|_{\phi_r}}{\left(\partial_y F_{TE}|_{\phi_r}\right)^2} + \frac{1}{a}\frac{\Delta F_{MM}|_{\phi_r}\Delta\partial_y F_{MM}|_{\phi_r}}{\left(\partial_y F_{TE}|_{\phi_r}\right)^2}, \tag{2.8}$$

$$\Delta\delta_{1,SE} = + \frac{1}{a}\frac{\Delta F_{SE}|_{\phi_r}}{\partial_y F_{TE}|_{\phi_r}} - \frac{1}{a}\frac{F_{TE}|_{\phi_r}\Delta\partial_y F_{SE}|_{\phi_r}}{\left(\partial_y F_{TE}|_{\phi_r}\right)^2} + \frac{1}{a}\frac{\Delta F_{SE}|_{\phi_r}\Delta\partial_y F_{SE}|_{\phi_r}}{\left(\partial_y F_{TE}|_{\phi_r}\right)^2}, \text{and} \tag{2.9}$$

$$\begin{aligned}\Delta\delta_{1,CT} = &- \frac{1}{a}\frac{\Delta F_{NE}|_{\phi_r}\Delta\partial_y F_{MM}|_{\phi_r}}{\left(\partial_y F_{TE}|_{\phi_r}\right)^2} - \frac{1}{a}\frac{\Delta F_{NE}|_{\phi_r}\Delta\partial_y F_{SE}|_{\phi_r}}{\left(\partial_y F_{TE}|_{\phi_r}\right)^2} \\ &- \frac{1}{a}\frac{\Delta F_{SE}|_{\phi_r}\Delta\partial_y F_{NE}|_{\phi_r}}{\left(\partial_y F_{TE}|_{\phi_r}\right)^2} + \frac{1}{a}\frac{\Delta F_{MM}|_{\phi_r}\Delta\partial_y F_{NE}|_{\phi_r}}{\left(\partial_y F_{TE}|_{\phi_r}\right)^2} \\ &- \frac{1}{a}\frac{\Delta F_{MM}|_{\phi_r}\Delta\partial_y F_{SE}|_{\phi_r}}{\left(\partial_y F_{TE}|_{\phi_r}\right)^2} + \frac{1}{a}\frac{\Delta F_{SE}|_{\phi_r}\Delta\partial_y F_{MM}|_{\phi_r}}{\left(\partial_y F_{TE}|_{\phi_r}\right)^2}\end{aligned} \tag{2.10}$$

The cross term arises from simultaneous changes in the different shift contributions. The error for Method 1, called the Taylor series linearization error below, is quantified as the difference between the actual shift ($\Delta\delta$) and the Method 1 shift ($\Delta\delta_1$), e.g. $\Delta\delta - \Delta\delta_1$.

Method 2

Method 1 is based on a linearized Taylor series and may depend on the choice of reference latitude. In order to ensure the results are independent of Taylor series linearization and choice of reference latitude we consider a second method. Let the initial storm track position

be ϕ_o, i.e. $F_{TE}|_{\phi_o} = 0$, and let the storm track position in response to a change of transient eddy MSE flux divergence ΔF_{TE} be ϕ_{TE}, i.e. $(F_{TE} + \Delta F_{TE})|_{\phi_{TE}} = 0$ such that the storm track shift is $\Delta\delta_2 = \phi_{TE} - \phi_o = \Delta\delta$ where the subscript indicates Method 2 and the actual shift is $\Delta\delta$. According to the MSE budget (2.2) any change in transient eddy MSE flux divergence can be expressed as $\Delta F_{TE} = \Delta F_{NE} - \Delta F_{MM} - \Delta F_{SE}$. Hence the shift can once again be decomposed into contributions from net energy, mean meridional circulation, stationary eddies and a cross term

$$\Delta\delta_2 = \Delta\delta_{2,NE} + \Delta\delta_{2,MM} + \Delta\delta_{2,SE} + \Delta\delta_{2,CT} \tag{2.11}$$

where the subscript refers to Method 2 and

$$\Delta\delta_{2,NE} = \phi_{NE} - \phi_o \quad \text{where} \quad (F_{TE} + \Delta F_{NE})|_{\phi_{NE}} = 0 \tag{2.12}$$

$$\Delta\delta_{2,MM} = \phi_{MM} - \phi_o \quad \text{where} \quad (F_{TE} - \Delta F_{MM})|_{\phi_{MM}} = 0 \tag{2.13}$$

$$\Delta\delta_{2,SE} = \phi_{SE} - \phi_o \quad \text{where} \quad (F_{TE} - \Delta F_{SE})|_{\phi_{SE}} = 0 \tag{2.14}$$

$$\Delta\delta_{2,CT} = \Delta\delta - (\Delta\delta_{2,NE} + \Delta\delta_{2,MM} + \Delta\delta_{2,SE}). \tag{2.15}$$

Once again, the cross term arises from nonlinear change involving simultaneous changes in the different shift contributions [See (2.10)].

In summary, Method 1 is based on a linearized Taylor series and was motivated by the success of the linearized Taylor series framework for EFE shifts (Bischoff & Schneider, 2014). The advantage of Method 1 is that it quantifies whether linear changes at the reference latitude (change in F_{TE} and its slope) accurately capture the storm track shift. This allows for a clear geometric interpretation of the shift (see Fig. 2.1) and can be related to the changes in amplitude and latitudinal width of the transient eddy MSE flux. Note this is similar to the Bischoff & Schneider (2014) linearized EFE framework, which has a clear

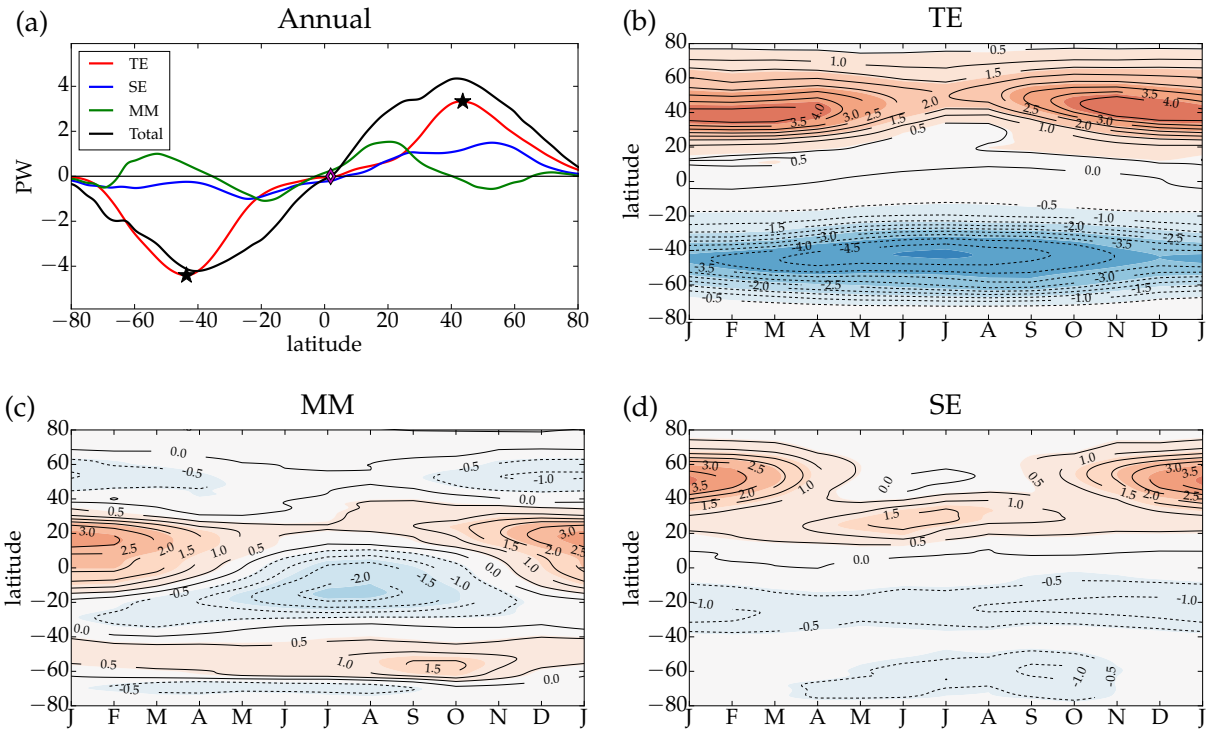

Figure 2.2: (a) Vertically integrated, annual and zonal mean MSE flux (PW) in the NCEP reanalysis dataset for 1970 to 2015 decomposed into different dynamical contributions. Diamond in (a) shows the location of the EFE and the stars denote the storm track position, i.e. latitude ϕ_0 where $F_{TE}|_{\phi_0} = 0$. Seasonal evolution of (b) transient eddy, (c) mean meridional circulation and (d) stationary eddy MSE flux. MSE flux is multiplied by $2\pi a \cos\phi$ in all panels.

geometric interpretation (see their Fig. 1). The disadvantages of Method 1 include the use of a linearized Taylor series and reference latitude. Method 2 is more accurate because 1) it effectively includes all orders of the Taylor series, and 2) is independent of a reference latitude. However it lacks the simple geometric interpretation as provided by Method 1.

2.2.2 Datasets

Reanalysis data

We use monthly atmospheric MSE flux data from the NCEP reanalysis (Kalnay & Coauthors, 1996) covering the period 1970 to 2015. The data were processed and decomposed following

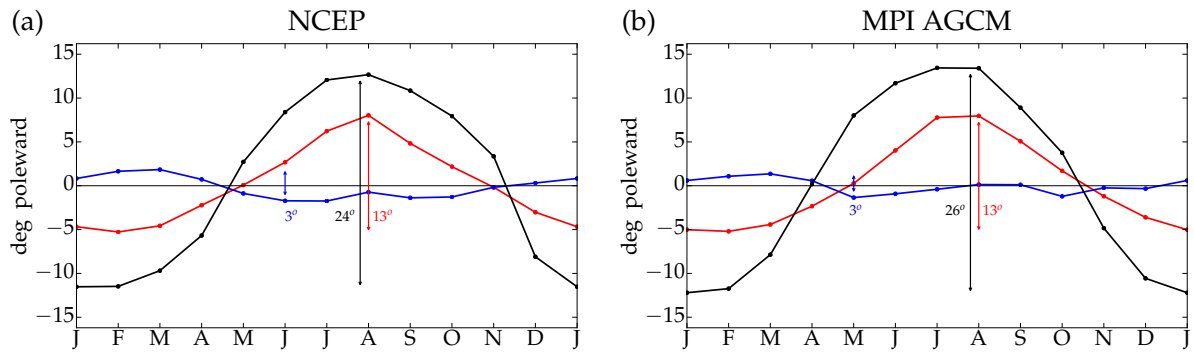

Figure 2.3: Seasonal evolution of storm track position (latitude ϕ_0 where $F_{TE}|_{\phi_0}$ = 0) in the Northern (red), Southern (blue) Hemispheres and EFE position (black) relative to the annual mean position for (a) NCEP reanalysis and (b) MPI AGCM. The annual mean EFE and storm track positions are (a) 1.9°, 43.3° , -43.8° and (b) 1.9°, 42.9°, -41.5°, respectively.

Marshall *et al.* (2013). The annual, zonal mean total MSE flux and its decomposition into mean meridional circulation, stationary eddy and transient eddy components is shown in Fig. 2.2a. The seasonal evolution is shown in Fig. 2.2b-d. There is larger seasonality of transient eddy MSE flux in the NH than in the SH. The NH storm track position, i.e. the latitude ϕ_0 where $F_{TE}|_{\phi_0} = 0$, exhibits a seasonal amplitude of 13.3° about its annual mean position of 43.3°N, which reflects an equatorward shift in winter and poleward shift in summer (red line, Fig. 2.3a). In contrast, the seasonal amplitude of SH storm track position is only 3.6° about its annual mean position of 43.8°S (blue line, Fig. 2.3a). In both hemispheres, the seasonal cycle of storm track position is of similar amplitude for the latent and sensible heat MSE flux components (Fig. 2.14).

The mean meridional circulation MSE flux reflects the seasonal evolution of the Hadley circulation in the tropics (Fig. 2.2c), which coincides with seasonal shifts of the EFE that has an amplitude of 24.2° (black line, Fig. 2.3a) about its annual mean position of 1.9°N. The Ferrel cell dominates the mean meridional circulation MSE flux in the extratropics and opposes the transient eddy MSE flux. The seasonal evolution of stationary eddy MSE flux in the NH (Fig. 2.2d) reflects large amplitude wintertime stationary eddies driven by diabatic heating, topography and transient eddy vorticity flux (see Fig.13 in Wang & Ting, 1999;

Held *et al.*, 2002) whereas summertime stationary eddies are driven by Monsoonal diabatic heating (see Fig. 15 Wang & Ting, 1999). The SH exhibits a much weaker seasonal evolution of stationary eddy MSE flux (Fig. 2.2d) consistent with its smaller land area. The seasonal evolution of the MSE flux in the NCEP reanalysis is robust when compared to the ERA-Interim reanalysis (Dee *et al.*, 2011) covering the period 1979 to 2015 (compare Figs. 2.2-2.3 with Figs. 2.16-2.17).

The NCEP reanalysis data is used to examine storm track shifts in response to seasonal insolation and the El Nino Southern Oscillation (ENSO). The ENSO response is quantified by the difference between El Nino minus La Nina years following Lu *et al.* (2008). In our analysis we used a December, January and February averaged NINO3.4 index value $\geq 0.5°$C to identify El Nino years (1972, 1976, 1977, 1979, 1982, 1986, 1987, 1991, 1994, 1997, 2002, 2004, 2006 and 2009) and an index value $\leq 0.5°$C to identify La Nina years (1971, 1973, 1974, 1975, 1984, 1988, 1998, 1999, 2000, 2007, 2010 and 2011)[1]. The NCEP data is interpolated onto a 0.1° degree grid.

2.2.3 Atmospheric general circulation model experiments

In order to examine storm track shifts on longer timescales, i.e. in response to increased CO_2, we conduct simulations with the MPI-ESM-LR AGCM, hereafter referred to as MPI AGCM (Stevens *et al.*, 2013). The AMIP configuration of the MPI AGCM with prescribed historical forcings (i.e., radiative forcing, SST, sea ice, etc.) from 1979 to 2008 (Gates *et al.*, 1999) does a reasonable job of reproducing the seasonal cycle of MSE flux (Fig. 2.4), EFE and storm track position (Fig. 2.3b).

Following previous work we consider the direct and indirect (fast and slow) effect of increased CO_2 on storm track position using AGCMs (He *et al.*, 2014; Shaw & Voigt, 2015; He & Soden, 2016). The direct effect involves increasing CO_2 by 4 times its climatological

1. See http://www.cpc.noaa.gov/products/analysis_monitoring/ensostuff/ensoyears.shtml for more information.

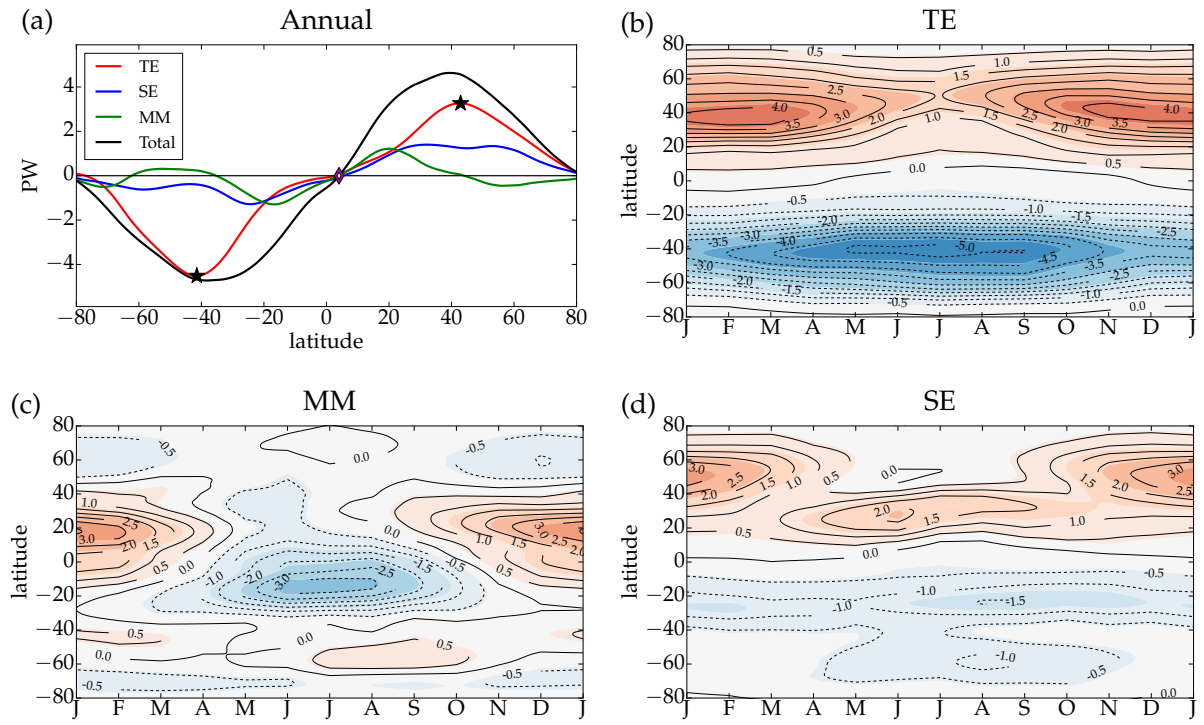

Figure 2.4: As in Fig. 2.2 but for the MPI-ESM AGCM.

value with fixed SST. Shaw & Voigt (2016a) showed that increased CO_2 over land dominates the storm track shift in response to the CO_2 direct effect (see their Table 1). Thus, the direct effect will focus on the response to increased CO_2 over land. The indirect effect involves increased SST with fixed CO_2. The simplest SST warming is uniform warming by 4K, which we will refer to as increased SST. The MPI-AGCM simulations used here are the same as those in Shaw & Voigt (2016a). The data are interpolated onto a 0.1° degree grid.

2.3 Results

The MSE framework provides a connection between storm track shifts and energetic perturbations. The importance of this connection can be illustrated by making a falsifiable prediction of month-to-month storm track shifts in response to seasonal insolation. Given the transient eddy MSE flux divergence F_{TE} and storm track position ϕ_0 during month

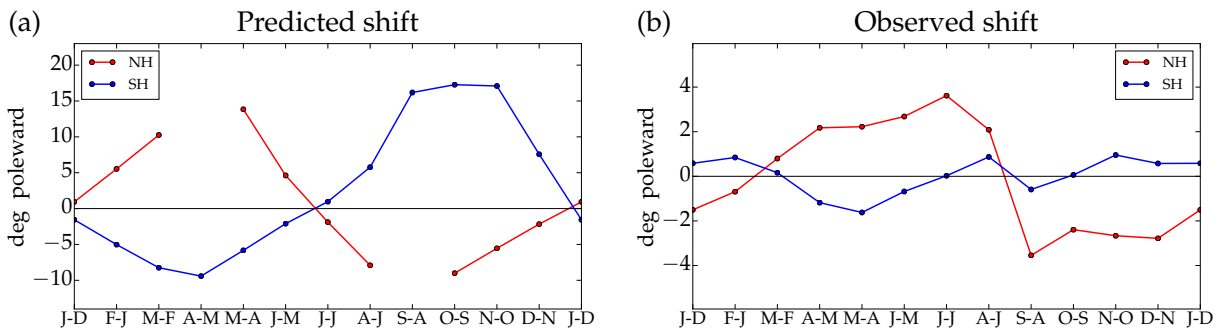

Figure 2.5: Month-to-month storm track shift as (a) predicted using Method 2 in response to TOA insolation with fixed TOA albedo and (b) observed in the NCEP reanalysis.

m, Method 2 is used to predict the storm track shift between months m and $m+1$ due to TOA insolation change $\Delta F^{\downarrow}_{TOA,SW}$. Assuming fixed TOA albedo α_{TOA} for the adjacent months, the storm track shift is $\Delta\delta \approx \Delta\delta_{NE} = \phi_{NE} - \phi_0$ where $(F_{TE} + \Delta F_{NE})|_{\phi_{NE}} = (F_{TE} + (1-\alpha_{TOA})\Delta F^{\downarrow}_{TOA,SW})|_{\phi_{NE}} = 0$. Figure 2.5a shows the predicted seasonal storm track shift. Note for some months there is no latitude where the transient eddy MSE flux divergence equals zero after adding the insolation change, i.e. ϕ_{NE} does not exist for some months. If insolation dominated storm track shifts then there would be a poleward shift between winter and summer and an equatorward shift between summer and winter in both hemispheres. Interestingly the observed NH shift is smaller and out-of-phase with the predicted shift. In the SH the observed shift is much weaker and does not exhibit clear seasonality (Fig. 2.5b). Hence, TOA insolation alone does not determine seasonal storm track shifts.

In the following subsections the MSE framework is applied diagnostically across three timescales (seasonal, interannual and centennial) to determine the dominant contributions in (2.6). Since the MSE framework is based on the MSE budget, it does not imply causality. However it can be used to formulate hypotheses to test causality as discussed in section 4. The goal is to find shifts involving one or two dominant contributions. In order to extract robust behavior we focus on large amplitude shifts, i.e. shifts larger than 1° latitude (shifts

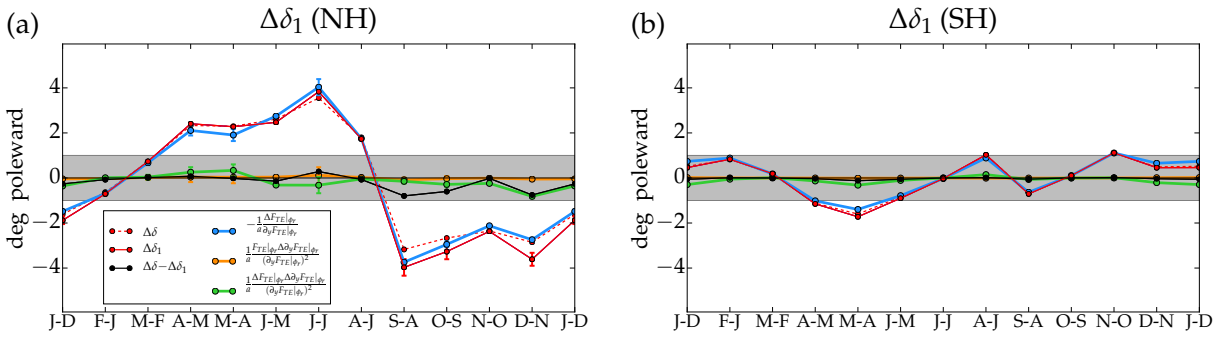

Figure 2.6: Month-to-month storm track shift according to Method 1 [see (2.5)] in the (a) Northern and (b) Southern Hemispheres in NCEP reanalysis. The actual storm track shift ($\Delta\delta$) and Taylor series linearization error ($\Delta\delta - \Delta\delta_1$) are shown for comparison.

less than 1° latitude involve gray shading in all figures).

2.3.1 Seasonal shift

On seasonal timescales we focus on month-to-month storm track shifts. Figure 2.6 shows the storm track shift computed following Method 1 [see (2.5)]. The transient eddy MSE flux divergence change dominates the storm track shift (blue line, Fig. 2.6a,b) and the contribution from slope and nonlinear seasonal changes (orange and green lines, Fig. 2.6a,b) is small. The Taylor series linearization error (black line, 2.6a,b) is also small.

The decomposition of NH seasonal storm track shifts into net energy, mean meridional circulation, stationary eddy, and cross term contributions following Method 1 [see (2.6)] is shown in Fig. 2.7a. Once again the MSE flux divergence dominates over slope and nonlinear seasonal changes for each contribution [see (2.7)-(2.9) and Fig. 2.22]. A large amplitude poleward shift emerges from April minus March to August minus July and an equatorward shift emerges from September minus August to December minus November in the NH (red line, Fig. 2.7a)

The dominant contribution to the seasonal shift is from stationary eddy MSE flux divergence (blue line, Fig. 2.7a). During other times, the shift is less than ±1° and all contributions are important. According to Method 2 stationary eddy MSE flux divergence

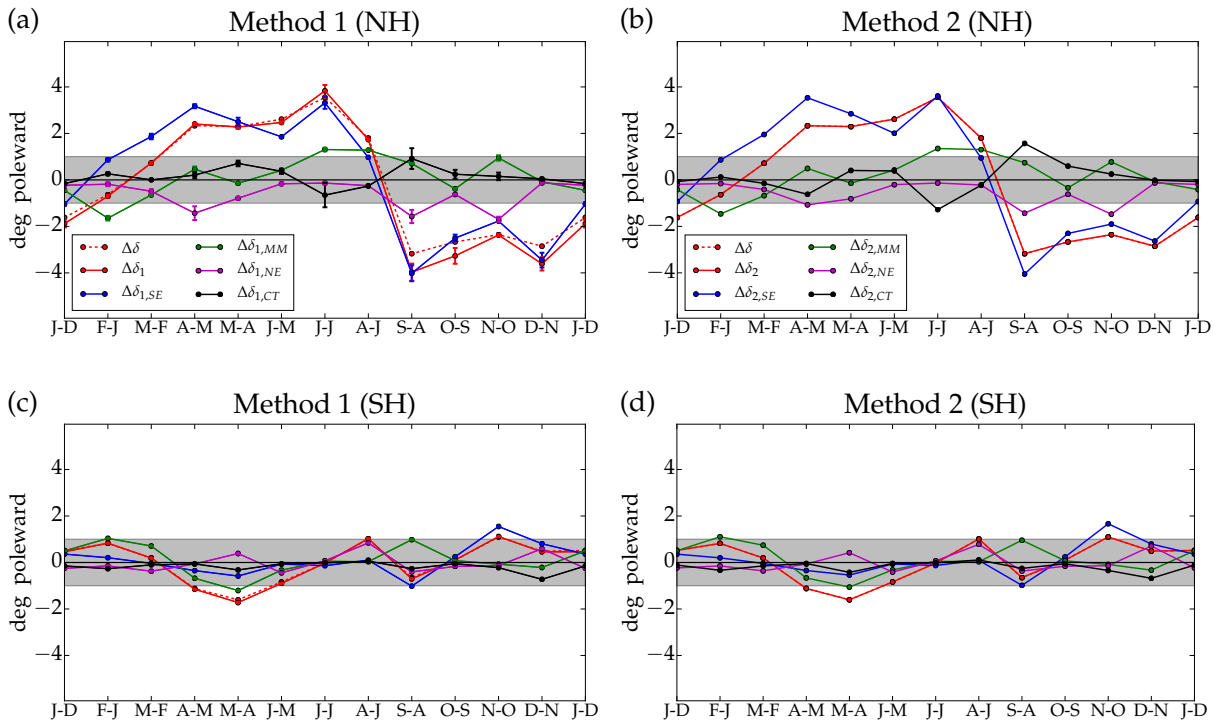

Figure 2.7: Month-to-month storm track shift decomposed into net energy, mean meridional circulation, stationary eddy and cross term contributions following (a,c) Method 1 [see (2.6)] and (b,d) Method 2 [see (2.11)] in the Northern (top) and Southern (bottom) Hemispheres for the NCEP reanalysis. Actual shift ($\Delta\delta$) is shown for comparison. For Method 1 circles and bars indicate the mean and ±1 standard deviation over a range of reference latitudes (see section 2a).

is also the dominant NH shift contribution (Fig. 2.7b). In the SH, the month-to-month shift is less than ±1° with the exception of May minus April when there is an equatorward shift, however no contribution dominates according to both Methods (Fig. 2.7c,d). The cross term for Method 2 is consistent with Method 1 and is small in both hemispheres (black line, Fig. 2.7a-d).

Overall, the MSE framework for storm track shifts suggests that the seasonal storm track shift in the NH is connected to the seasonal evolution of stationary eddy MSE flux divergence. The latitudinal structure of compensation for July minus June, September minus August and December minus November is shown in Fig. 2.8. Between July and June, stationary eddies diverge MSE flux in the subtropics and converge it in midlatitudes (blue

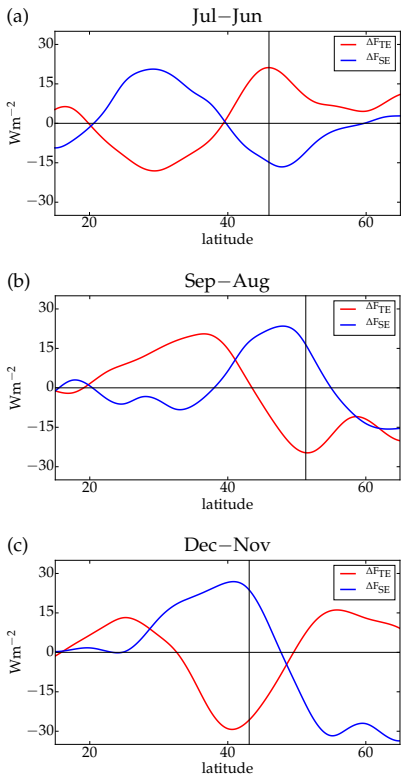

Figure 2.8: Change in transient eddy (ΔF_{TE}) and stationary eddy (ΔF_{SE}) MSE flux divergence in the Northern Hemisphere for (a) July minus June, (b) September minus August and (c) December minus November for the NCEP reanalysis. The vertical black line denotes the climatological storm track position during (a) June, (b) August and (c) November.

line, Fig. 2.8a). Transient eddies compensate by diverging MSE flux in midlatitudes (red line, Fig. 2.8a) resulting in a poleward shift of the storm track. Between September and August, stationary eddies diverge MSE flux in midlatitudes and converge it in the subtropics and high latitudes (blue line, Fig. 2.8b). Transient eddies compensate by converging MSE flux in midlatitudes (red line, Fig. 2.8b) resulting in an equatorward shift of the storm track. Finally, between December and November, stationary eddies diverge MSE flux in midlatitudes and converge it in high latitudes (blue line, Fig. 2.8c). Transient eddies compensate by converging MSE flux in midlatitudes (red line, Fig. 2.8c) resulting in an equatorward shift of the storm track. The seasonal shifts in the NCEP reanalysis are in general agreement with those from the ERA-Interim reanalysis (compare Figs. 2.7 & 2.8 to

Table 2.1: Stormtrack shift in response to El Nino minus La Nina conditions.

Hemisphere	Method1	Method2
NH	$\Delta\delta_1 = -1.61° \pm 0.17°$	$\Delta\delta_2 = -1.45°$
	$\Delta\delta_{1,NE} = 0.61° \pm 0.07°$	$\Delta\delta_{2,NE} = 0.65°$
	$\Delta\delta_{1,MM} = -0.78° \pm 0.14°$	$\Delta\delta_{2,MM} = -0.65°$
	$\Delta\delta_{1,SE} = -1.49° \pm 0.14°$	$\Delta\delta_{2,SE} = -1.45°$
	$\Delta\delta_{1,CT} = -0.05° \pm 0.08°$	$\Delta\delta_{2,CT} = 0.00°$
SH	$\Delta\delta_1 = -0.69° \pm 0.00°$	$\Delta\delta_2 = -0.80°$
	$\Delta\delta_{1,NE} = -0.17° \pm 0.00°$	$\Delta\delta_{2,NE} = -0.15°$
	$\Delta\delta_{1,MM} = -0.36° \pm 0.00°$	$\Delta\delta_{2,MM} = -0.35°$
	$\Delta\delta_{1,SE} = -0.16° \pm 0.00°$	$\Delta\delta_{2,SE} = -0.25°$
	$\Delta\delta_{1,CT} = 0.00° \pm 0.00°$	$\Delta\delta_{2,CT} = -0.05°$

Figs. 2.18 & 2.19).

2.3.2 Interannual shift

On interannual timescales we consider the storm track shift due to ENSO, which is the dominant mode of climate variability. The jet stream shifts equatorward in response to El Nino minus La Nina conditions during NH winter (December, January and February, Seager *et al.*, 2003; Lu *et al.*, 2008). Consistent with the jet shift, the storm track position defined as the latitude of zero transient eddy MSE flux divergence, shifts equatorward by 1.5° and 0.8° in the NH and SH respectively. Table 1 summarizes the storm track shifts computed following Methods 1 and 2.

According to both methods the dominant contribution to the equatorward shift of the NH storm track in response to El Nino minus La Nina conditions is from stationary eddy MSE flux divergence. Stationary eddies diverge MSE flux in midlatitudes near the storm track position during NH winter and converge it in the subtropics and high latitudes (blue line, Fig. 2.9a). Transient eddies compensate by converging MSE flux in midlatitudes (red line, Fig. 2.9a), which shifts the storm track equatorward.

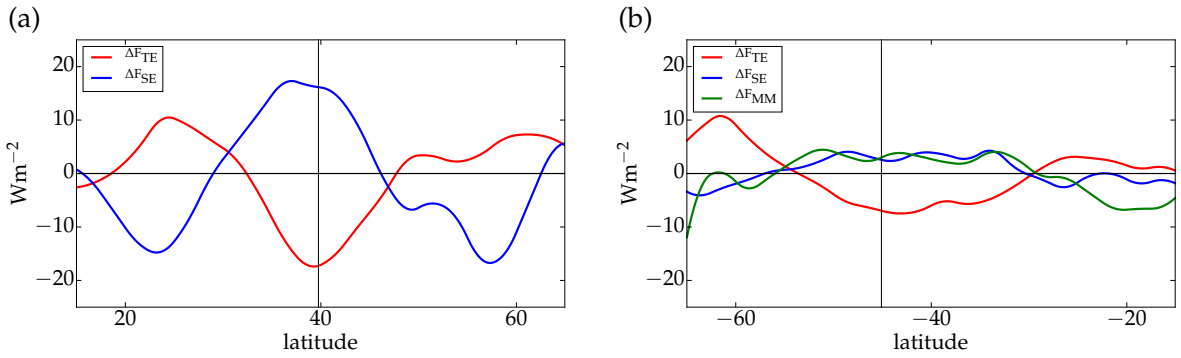

Figure 2.9: El Nino minus La Nina response of wintertime (DJF) transient eddy (ΔF_{TE}), stationary eddy (ΔF_{SE}) and mean meridional circulation (ΔF_{MM}) MSE flux divergence in the (a) Northern and (b) Southern Hemispheres for the NCEP reanalysis. The vertical black line denotes the climatological storm track position for La Nina conditions.

In the SH, the mean meridional circulation and stationary eddy MSE flux divergence both contribute to the equatorward shift of the SH storm track in response to El Nino minus La Nina conditions. However the shift is less than 1°. The mean meridional circulation and stationary eddies diverge MSE flux in midlatitudes (blue and green line, Fig. 2.9b), which is compensated by transient eddy MSE flux convergence (red line, Fig. 2.9b). Once again, the ENSO shift in the NCEP reanalysis is in general agreement with that from the ERA-Interim reanalysis (compare Fig. 2.9 to Fig. B5).

2.3.3 Centennial shift

On centennial timescales we consider the response to increased CO_2. As discussed in section 2b, we separate the direct (increased CO_2 over land) and indirect (increased SST with fixed CO_2) effects of CO_2 on the storm track. The direct effect produces a poleward storm track shift during NH summer but does not significantly impact the SH storm track (Fig. 2.10a,b). The indirect effect produces an equatorward shift during June in the NH and a poleward shift during January in the NH and during May and October in the SH (Fig. 2.10c,d). Consistent with the seasonal shifts, the transient eddy MSE flux divergence change dominates the Method 1 shift (blue line, Fig. 2.10) and the Taylor series linearization error

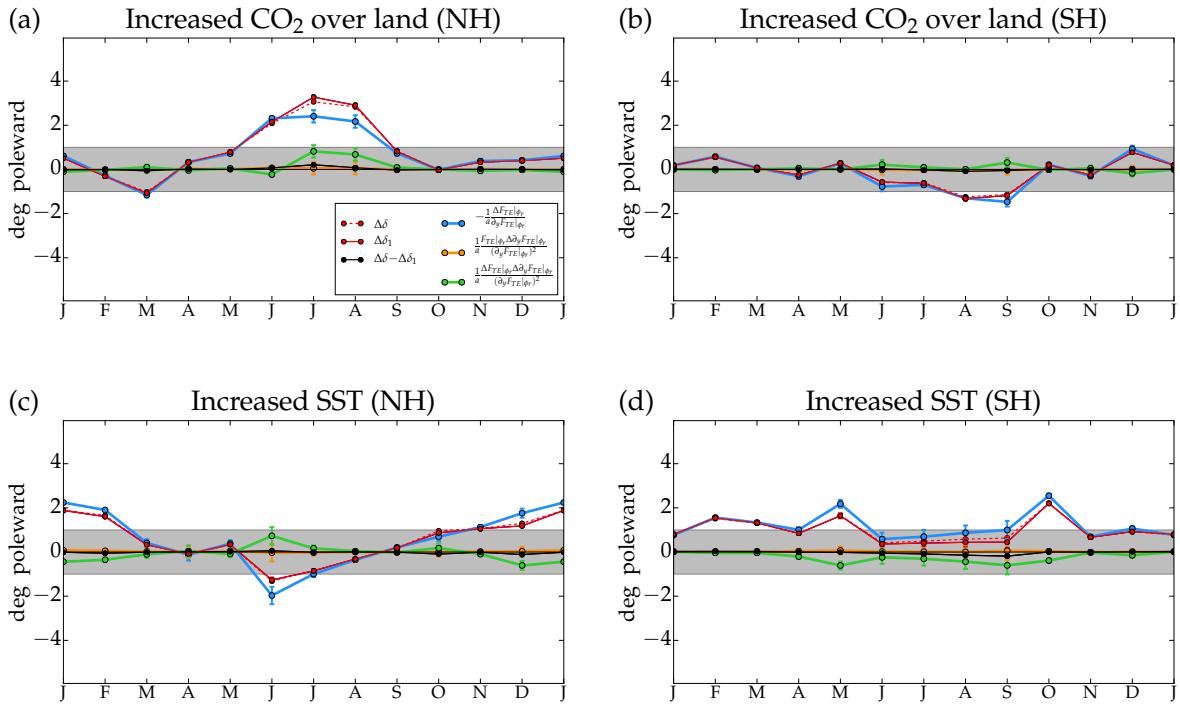

Figure 2.10: As in Fig. 2.6 but for the response to (a,b) increased CO_2 over land and (c,d) increased SST for the MPI-AGCM.

(black line, 2.10) is small.

The decomposition of storm track shifts in response to increased CO_2 into net energy, mean meridional circulation, stationary eddy, and cross term contributions following Method 1 [see (2.6)] is shown in Figs. 2.11a,b and 2.12a,b. Once again the MSE flux divergence change dominates the Method 1 shift decomposition (Fig. 2.24 and 2.24). According to both methods the dominant contribution to the poleward shift during NH summer in response to increased CO_2 over land is from stationary eddy MSE flux divergence (blue line in Fig. 2.11a,b). In response to increased CO_2 over land, stationary eddies diverge MSE flux in the subtropics and converge it in midlatitudes (blue line, Fig. 2.13a). Transient eddies compensate by diverging MSE flux in midlatitudes (red line, Fig. 2.13a) resulting in a poleward shift of the storm track. The response to increased CO_2 over land is similar to the seasonal response between July and June (see Fig. 2.8a).

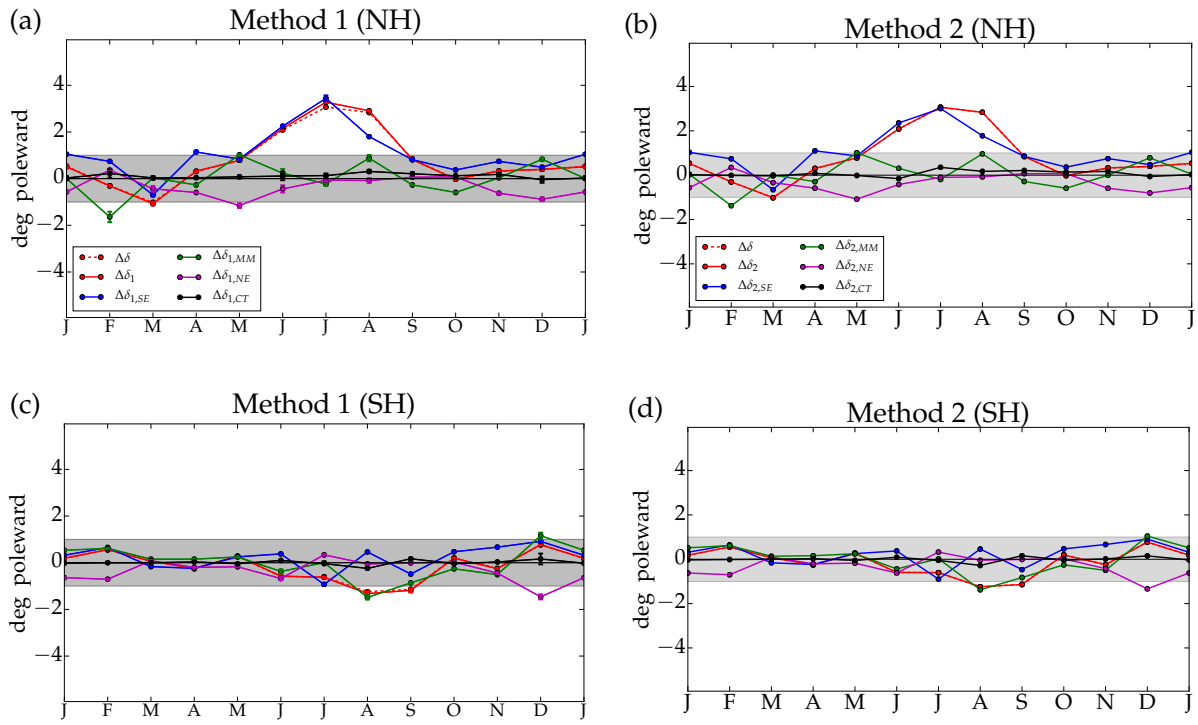

Figure 2.11: As in Fig. 2.7 but for the response to increased CO_2 over land for the MPI-AGCM.

According to both methods the dominant contribution to the equatorward shift of the NH storm track during June in response to increased SST is from stationary eddy MSE flux divergence (blue line in Fig. 2.12a,b). Stationary eddies diverge MSE flux in the midlatitudes and converge it in the subtropics (blue line, Fig. 2.13b). Transient eddies compensate by converging MSE flux in midlatitudes (red line, Fig. 2.13b). The response to increased SST during June is opposite to the response to increased CO_2 over land during July suggesting increased CO_2 and increased SST exert a tug of war on storm track position (Shaw *et al.*, 2016). According to both methods the dominant contribution to the poleward shift of the NH storm track in response to increased SST during January is from mean meridional circulation MSE flux divergence (Fig. 2.12a,b). The mean meridional circulation diverges MSE flux in midlatitudes and converges it in the subtropics and high latitudes (green line, Fig. 2.13c). Transient eddies compensate by diverging MSE flux in the midlatitudes (red line, Fig. 2.13c),

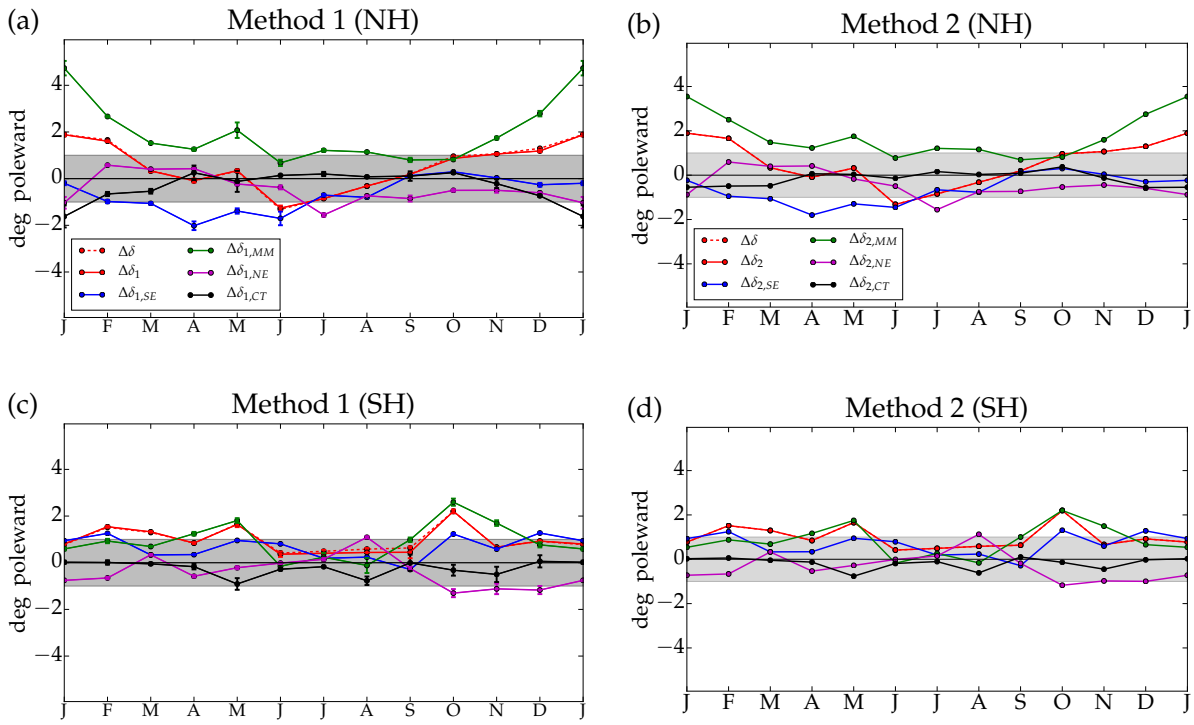

Figure 2.12: As in Fig. 2.7 but for the response to increased SST for the MPI-AGCM.

which shifts the storm track poleward in response to increased SST.

The mean meridional circulation is also the dominant contribution to the poleward shift of the SH storm track in response to increased SST during October (Fig. 2.12c,d). Once again, the mean meridional circulation diverges MSE flux in the midlatitudes during October and converges it in the subtropics and high latitudes (green line, Fig. 2.13d). The transient eddies compensate by diverging MSE flux in the midlatitudes (red line, Fig. 2.13d).

2.4 Conclusions and discussion

A framework was developed for understanding shifts of the zonal-mean storm track using the atmospheric MSE budget. The results build upon an MSE framework for EFE shifts (Schneider *et al.*, 2014; Bischoff & Schneider, 2014). storm track position was defined as the latitude of zero transient eddy MSE flux divergence. Two methods were developed to

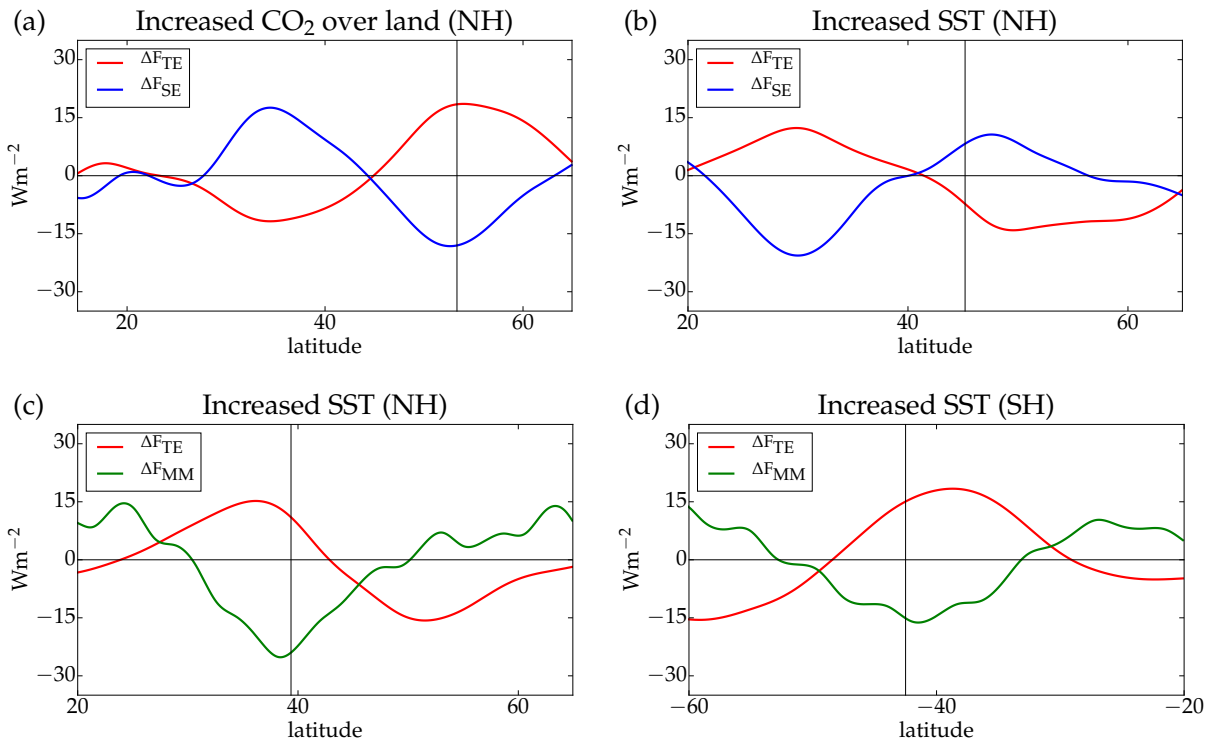

Figure 2.13: Response of MSE flux divergence to (a) increased CO_2 over land during July in the Northern Hemisphere and to increased SST during (b) June in the Northern Hemisphere, (c) January in the Northern Hemisphere and (d) October in the Southern Hemisphere for the MPI-AGCM. The vertical black line denotes the climatological storm track position.

understand storm track shifts. The first method is based on the Taylor series linearization of transient eddy MSE flux divergence about a reference latitude near the storm track position. According to this method, storm track shifts are driven by changes in transient eddy MSE flux divergence and its slope at the reference latitude. The transient eddy MSE flux divergence at the reference latitude dominates the storm track shifts. Thus, a poleward shift of the storm track occurs due to a transient eddy MSE flux divergence response near the storm track position whereas an equatorward shift occurs due to a flux convergence. The Taylor series linearization error was small across the timescales considered.

The second method for quantifying storm track shifts does not involve a Taylor series or a reference latitude. It imposes a change in transient eddy MSE flux divergence at all latitudes to the climatological transient eddy MSE flux. According to the MSE budget, any change

in transient eddy MSE flux divergence is balanced by the sum of changes in net energy (MSE input to the atmosphere minus atmospheric MSE storage) and MSE flux divergence by longitudinally-symmetric mean meridional circulation and longitudinally-asymmetric stationary eddies. Thus, both methods decompose the storm track shift into contributions from net energy, mean meridional circulation, stationary eddies and a cross term. The cross term involves changes in multiple contributions and was small across the timescales considered.

The MSE framework was applied to storm track shifts across timescales, including month-to-month seasonal shifts, interannual shifts in response to ENSO and centennial shifts in response to increased CO_2. The response to increased CO_2 was decomposed into direct (increased CO_2 over land with fixed SST) and indirect (increased SST with fixed CO_2) contributions. Seasonal and ENSO shifts were quantified using NCEP and ERA-Interim reanalysis data whereas shifts in response to increased CO_2 were quantified using the MPI AGCM. Changes in net energy were a small contribution across the timescales considered. Stationary eddies are the dominant contribution to storm track shifts in response to seasonal insolation in the NH, El Nino minus La Nina conditions during NH winter and direct and indirect effects of increased CO_2 during NH summer. The mean meridional circulation is the dominant contribution to storm track shifts in response to the CO_2 indirect effect during NH winter and in SH during May and October.

The insignificance of net energy changes is consistent with previous work that highlighted the importance of ocean surface energy storage (Fasullo & Trenberth, 2008; Donohoe & Battisti, 2013). The dominance of circulation contributions to storm track shifts suggests that compensation between different circulation components is important for shifts across the timescales considered. Understanding the importance of net energy changes and compensation in response to forcings on different timescales (e.g. decadal and millennial), e.g. ozone depletion, aerosol and paleoclimate changes, is work in progress.

Since compensation does not imply causality one cannot draw causal conclusions from the

results. However, the results can be used to formulate hypotheses regarding causality. For example, the results show that the seasonal storm track shifts are connected to stationary eddy evolution. Thus one could hypothesize that in the absence of significant net energy and stationary eddy changes there is no seasonal shift. Furthermore, if net energy changes are small but there is a significant stationary eddy signal that is not driven by transient eddies then stationary eddies may cause a seasonal shift. Current research is focused on this interpretation for the NH where summertime stationary eddies reflect Monsoon diabatic heating over land and not transient eddy vorticity sources according to stationary wave models (see Fig. 15 of Wang & Ting, 1999). Consistently, when the summertime Monsoon circulation and its stationary eddy MSE flux are amplified in response to the CO_2 direct effect, the storm track shifts poleward (Shaw & Voigt, 2015, 2016b). Idealized model experiments show that imposed subtropical zonally-asymmetric perturbations shift the storm track poleward (Shaw, 2014; Shaw & Voigt, 2015, 2016b). Along similar lines, the equatorward shift in response to El Nino minus La Nina conditions during NH winter involves changes in stationary eddies, which may be driven directly by the weakening of the Walker circulation. However, changes in zonal-mean tropical diabatic heating and the Hadley circulation may directly impact MSE and temperature gradients (Seager *et al.*, 2003; Tandon *et al.*, 2013; Lu *et al.*, 2014).

The compensation between the mean meridional circulation and transient eddies in response to the CO_2 indirect effect suggests transient eddy momentum fluxes, which drive the Ferrel circulation (Schneider, 2006), may cause the storm track shift. This compensation requires a better understanding of the connection between storm track and eddy driven jet shifts, which is an active area of research (Lu *et al.*, 2010; Donohoe *et al.*, 2014; Yamada & Pauluis, 2016; Dwyer & O'Gorman, 2016). Alternatively, changes in zonal-mean tropical diabatic heating and Hadley circulation may directly impact the storm track (Butler *et al.*, 2010; Lu *et al.*, 2014; Tandon *et al.*, 2013; Mbengue & Schneider, 2017). Assessing the

causality of compensation using idealized model simulations is work in progress.

Circulation compensation has a long history in the literature going back at least to Manabe & Terpstra (1974) who noted compensation between stationary and transient eddy MSE flux in response to flattening the continents in an AGCM. More recent examples of stationary-transient eddy compensation include: compensation on climatological and interannual timescales in reanalysis data (Trenberth & Stepaniak, 2003a,b), wintertime compensation in response to zonally localized surface heat flux perturbations in aquaplanet simulations (Kaspi & Schneider, 2013), wintertime compensation due to flattening Tibet (Park *et al.*, 2013) and summertime compensation in response to climate change over land versus ocean across the model hierarchy (Shaw & Voigt, 2015, 2016b). Mechanistically, compensation can occur via increased stationary eddy MSE flux that reduces baroclinicity and transient eddy MSE flux (Kaspi & Schneider, 2013) or it can occur through opposing diffusivity responses (see Fig. 8 and 10 of Shaw & Voigt, 2016b). While compensation does not occur at each longitude it does occur in longitudinal sectors.

The MSE framework is based on the MSE budget and is therefore diagnostic. Using the framework to predict shifts of the storm track requires 1) a better understanding of circulation compensation using idealized models and 2) closures for the net energy, mean meridional circulation and stationary eddy contributions. Our results suggest zonal-mean net energy is not a useful closure, however previous work suggests energy input over land may be a useful closure for stationary eddy MSE flux during NH summer (Shaw & Voigt, 2016a,b). While the energetic perspective of storm track shifts is attractive because it connects storm track position and energetic perturbations, a complete understanding of shifts must include the momentum budget. Our results also do not account for shifts of zonally-localized storm tracks, which are known to occur in response to ENSO, anthropogenic aerosol and CO_2 changes. The MSE framework is currently being extended to address localized shifts. Overall the MSE framework represents a step toward a complete understanding of storm track shifts

across a range of timescales.

2.5 Appendices

2.5.1 Appendix A

The transient and stationary eddy MSE flux is decomposed into latent heat, sensible heat and potential energy flux components in Figs. 2.14 and 2.15. The results show thermal energy flux dominates for eddies (Rossby waves), i.e. $c_p\langle[\overline{v}^*\overline{T}^*]\rangle + L\langle[\overline{v}^*\overline{q}^*]\rangle > \langle[\overline{v}^*\overline{\Phi}^*]\rangle$ and $c_p\langle[\overline{v'T'}]\rangle + L\langle[\overline{v'q'}]\rangle > \langle[\overline{v'\Phi'}]\rangle$, because they are mostly geostrophic.

2.5.2 Appendix B

In addition to the NCEP reanalysis we also used monthly atmospheric MSE flux data from the ERA-Interim renalysis covering the period 1979 to 2015. The data were processed and decomposed following Marshall *et al.* (2013) and interpolated onto a 0.1° grid. The annually averaged and seasonal evolution of the MSE flux for ERA-Interim reanalysis compares well with the NCEP reanalysis (compare Fig. 2.16 to Fig. 2.2). Consistently there is also good agreement between the seasonal positions of the EFE and storm track position in the two reanalysis data sets (compare 2.17 and Fig. 2.3a).

According to the ERA-Interim data set, stationary eddy MSE flux divergence dominates the seasonal shifts of the NH storm track consistent with the NCEP reanalysis (compare Fig. 2.18 to Fig. 2.3). However, the largest month-to-month poleward shift occurs between June minus May in the ERA-Interim data instead of between July minus June as in the NCEP data. Figs. 2.19 and 2.20 should be compared with Figs. 2.8 and 2.9, respectively; see the discussion in the main text.

2.5.3 Appendix C

Method 1 is based on a first order Taylor series expansion of F_{TE} about a reference latitude, ϕ_r. The reference latitude is a mathematical concept that has no physical significance. It is

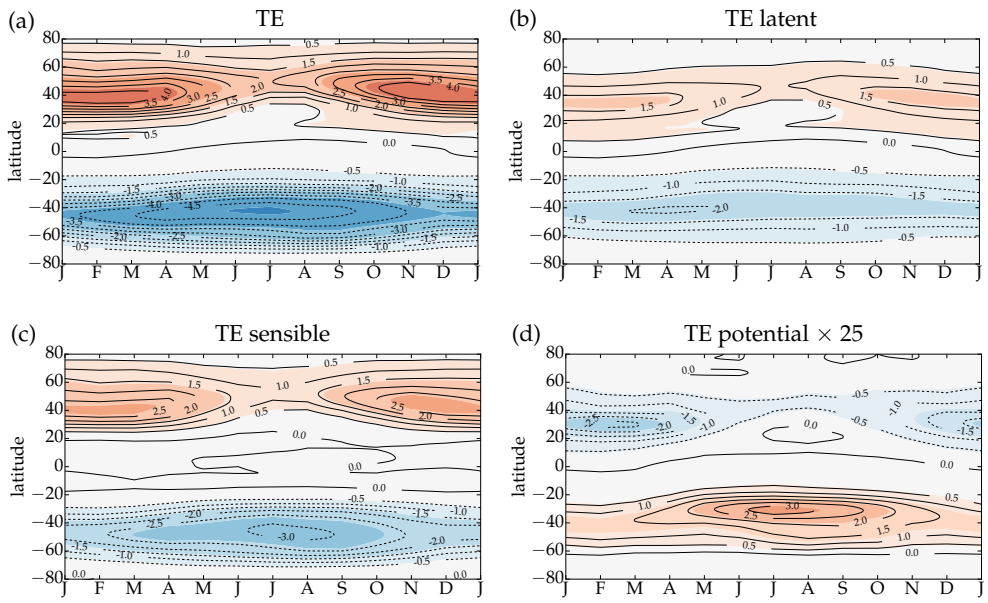

Figure 2.14: Seasonal evolution of vertically integrated and zonal mean transient eddy (a) MSE flux (PW) in the NCEP reanalysis dataset for 1979 to 2015 decomposed into (b) latent heat, (c) sensible heat and (d) potential energy flux. Note that the potential energy flux has been multiplied by 25 and all flux components have been multiplied by $2\pi a \cos\phi$.

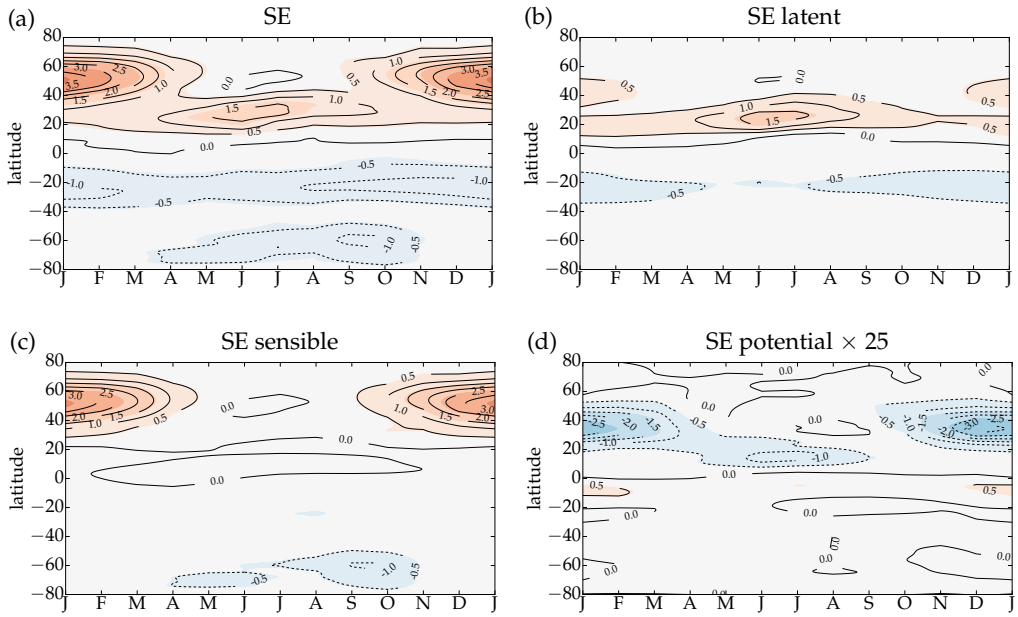

Figure 2.15: As in Fig. 2.14 but for the seasonal evolution of vertically integrated and zonal mean stationary eddy flux.

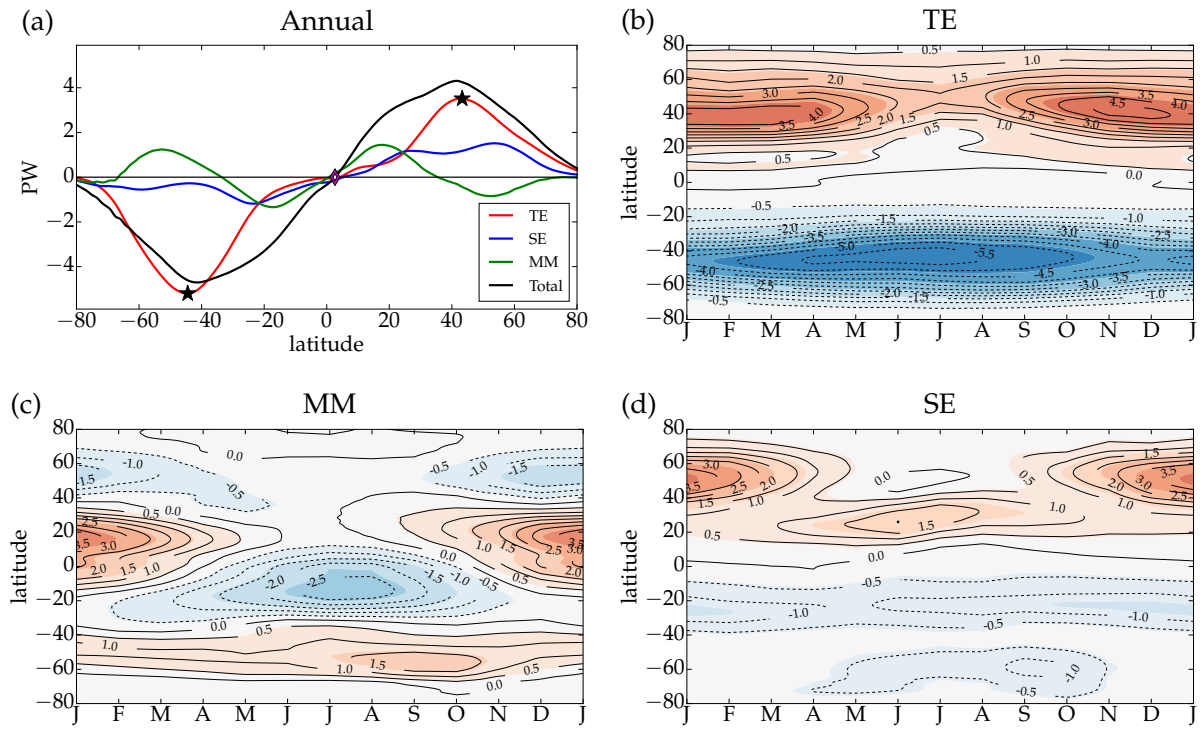

Figure 2.16: As in 2.2 but for the ERA-Interim renalysis.

chosen to minimize the Taylor series linearization error. For example, the error associated with the Taylor series linearization as a function of reference latitude during August is shown in . The linearization is only accurate in the vicinity of the storm track position (51.3°N). A similar linear regime exists for other months. In order to capture the range of latitudes representative of the linear regime, Method 1 uses a reference latitude defined as the current storm track position ± 1° in 0.5° increments (see gray shading in 2.21). The results for Method 1 are summarized by the mean (circle) and ±1 standard deviation (vertical bar) across the range of reference latitudes in Figs. 6, 7, 10-12, 2.18, 2.22 - 2.24.

A reference latitude corresponding to the annual mean storm track position and Hadley cell edge (latitude where the 10 m zonal-mean zonal wind is zero) were considered but not used because the associated Taylor series linearization error is very large at those latitudes during some months, e.g. August. While the Taylor series could be extended to include higher order terms we do not feel it is necessary because Method 2 effectively includes all

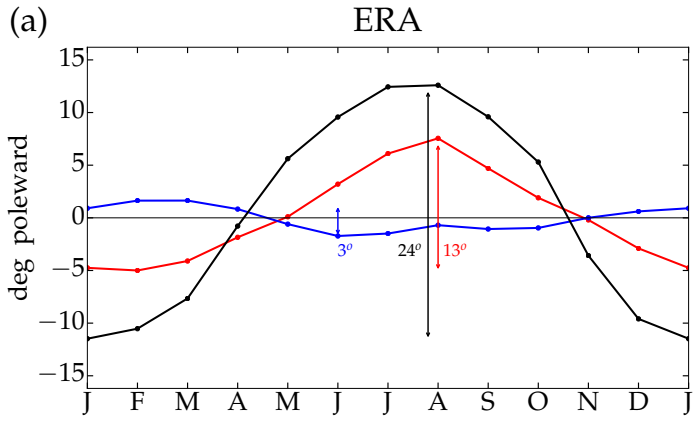

Figure 2.17: As in Fig. 2.3 but for the ERA-Interim renalysis.

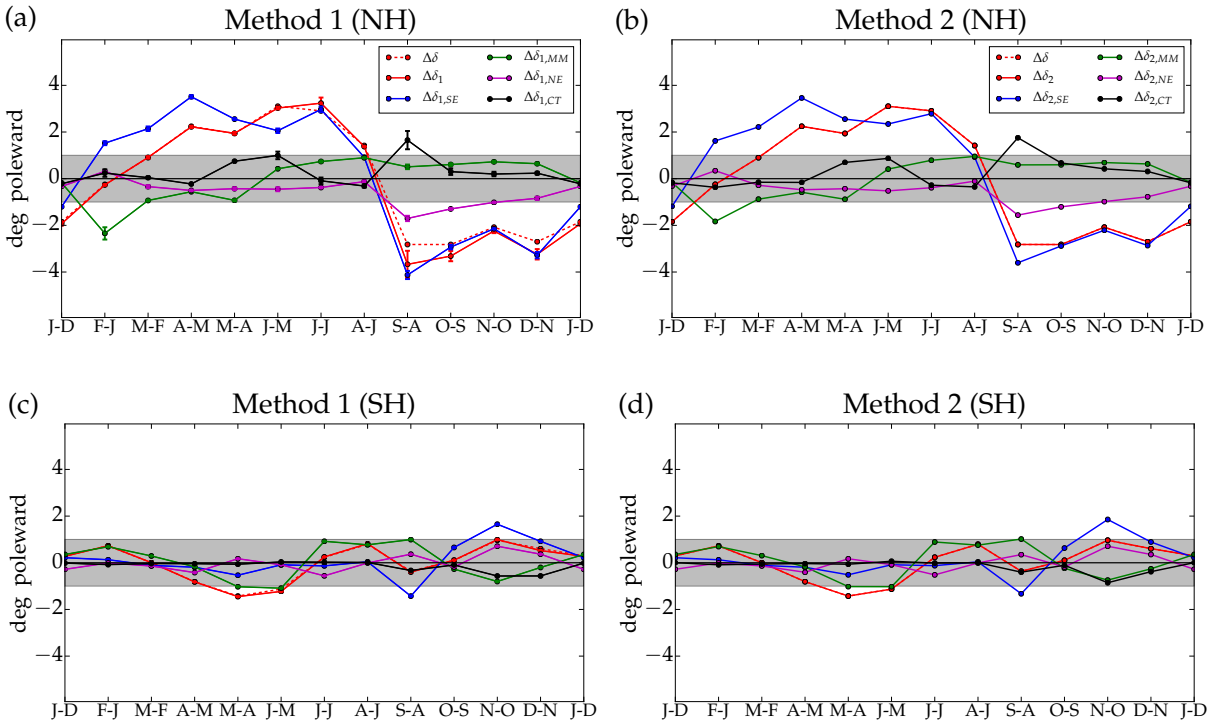

Figure 2.18: As in Fig. 2.7 but for the ERA-Interim renalysis.

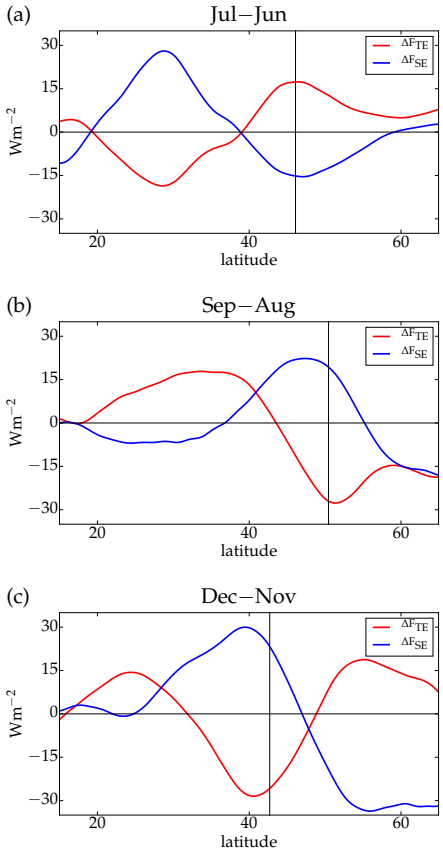

Figure 2.19: As in Fig.2.8 but for the ERA-Interim renalysis.

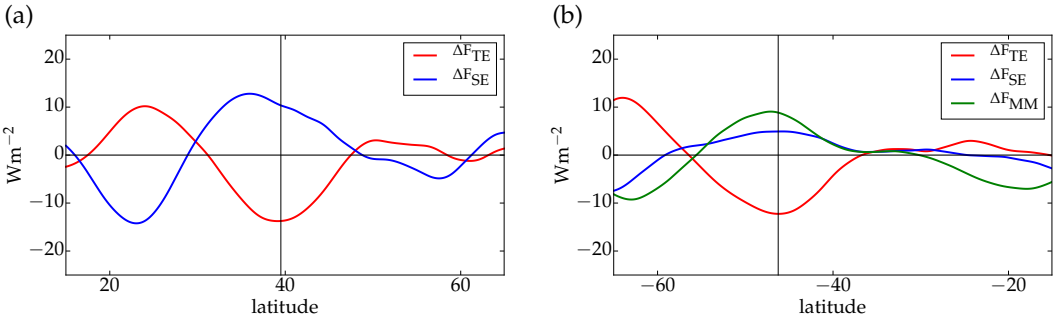

Figure 2.20: As in Fig. 2.9 but for the ERA-Interim renalysis.

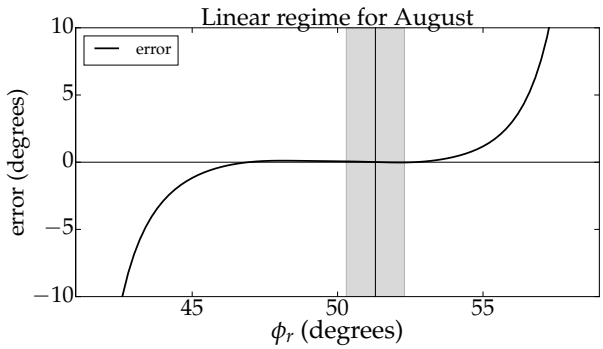

Figure 2.21: Error due to first order Taylor series approximation ($\delta - \delta_1$) during August as a function of the reference latitude ϕ_r [see (2.11)]. The vertical black line denotes the climatological storm track position (ϕ_o = 51.3°) in August. The gray shaded region shows the range of reference latitudes used for Method 1, e.g. $\phi_o - 1°$ to $\phi_o + 1°$.

orders of the Taylor series. Furthermore, the Hadley cell edge does not exhibit a clear connection to the storm track position interannually in the NH or during winter in the SH (Kang & Polvani, 2011).

Method 1 decomposes storm track shifts into contributions from net energy, mean meridional circulation, stationary eddies and a cross term [see (2.7)-(2.9)]. In all decompositions, the MSE flux divergence change (blue line, Fig. 2.22-2.24) dominates the total shift (red line, Fig. 2.22-2.24) and the difference between Method 1 and 2 is small (black line, Fig. 2.22-2.24).

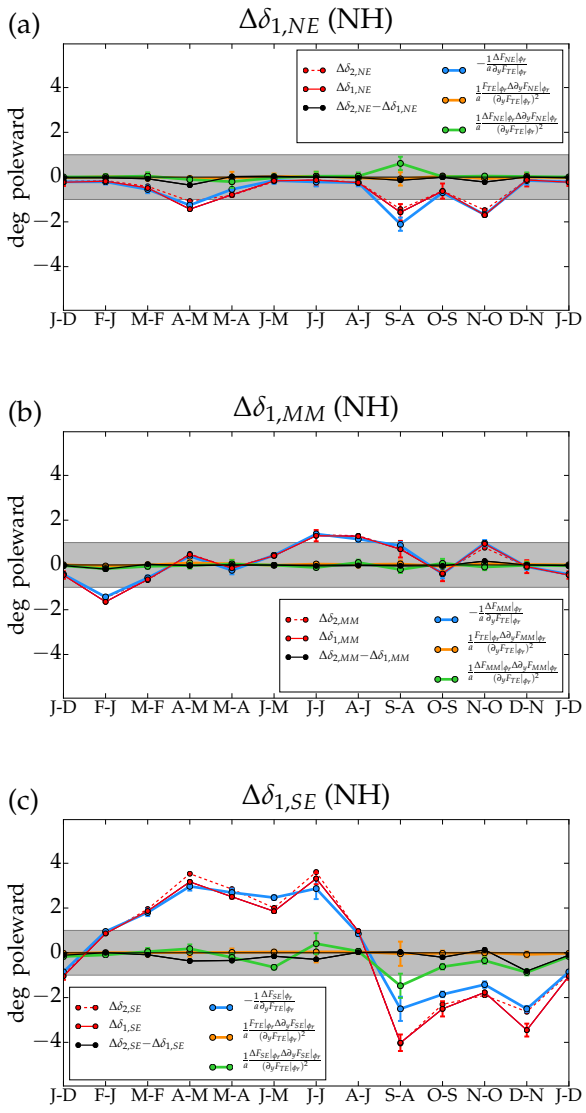

Figure 2.22: Month-to-month storm track shift due to (a) net energy [see (2.7)], (b) mean meridional circulation [see (2.8)], and (c) stationary eddy [see (2.9)] according to Method 1 for the Northern Hemisphere in NCEP reanalysis. The Method 2 decomposition ($\Delta\delta_2$) and Method 1 error relative to Method 2 ($\Delta\delta_2 - \Delta\delta_1$) are shown for comparison.

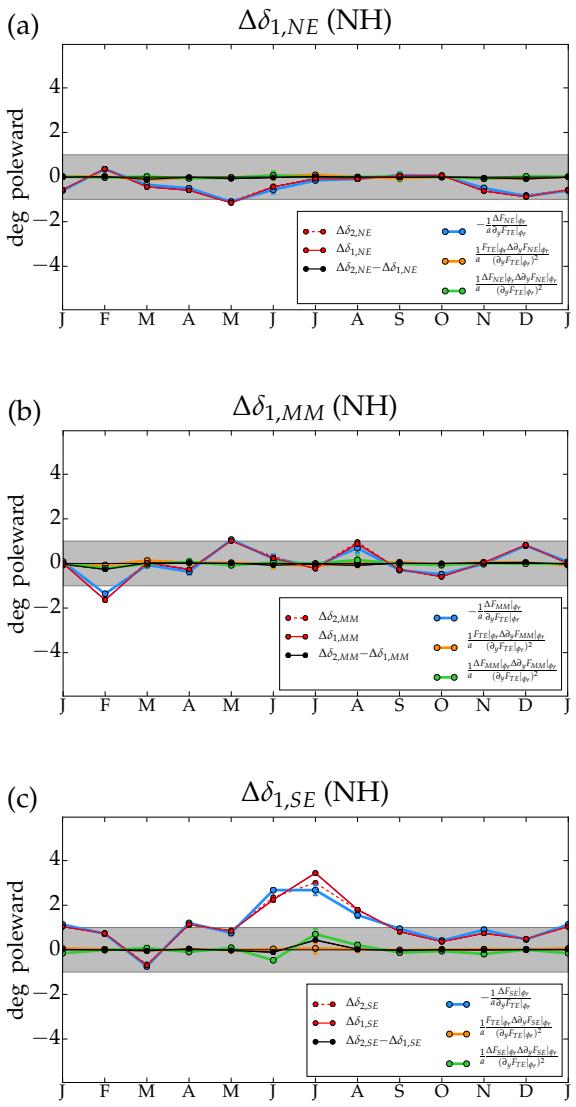

Figure 2.23: As in Fig. 2.22 but for the response to increased CO_2 over land in the MPI-AGCM.

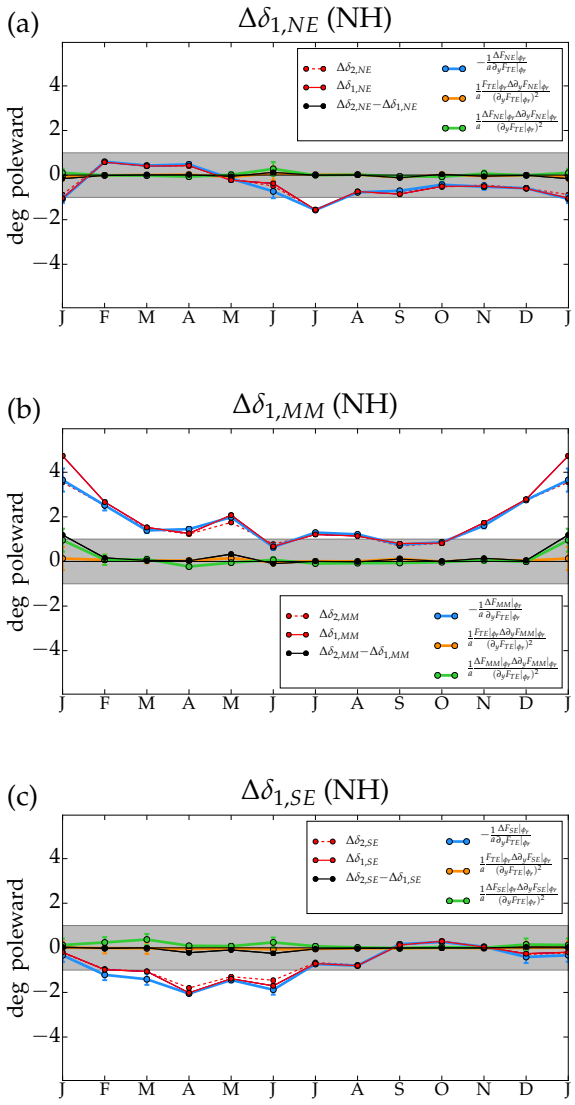

Figure 2.24: As in Fig. 2.22 but for the response to increased SST over land in the MPI-AGCM.

CHAPTER 3

SURFACE FLUXES MODULATE THE SEASONALITY OF ZONAL-MEAN STORMTRACKS

3.1 Introduction

The zonal-mean extratropical stormtracks exhibit distinct hemispheric seasonality. In the Northern Hemisphere (NH) the stormtrack weakens by ~ 2.5 PW and shifts poleward by ~ 10° from winter to summer. The Southern Hemisphere (SH) stormtrack shows much smaller seasonality (< 1 PW intensity change and < 3° shift, Chang *et al.*, 2002; Shaw *et al.*, 2016). Overall, stormtrack seasonality is much larger than changes due to global warming or inter-annual variability (O'Gorman, 2010; Barpanda & Shaw, 2017; Shaw *et al.*, 2018).

Several frameworks have been used to diagnose the factors affecting zonal-mean stormtrack seasonality. The first group focuses on the seasonality of time- and zonal-mean temperature. For example, the Eady parameter, which peaks where baroclinicity is largest, has been used to explain stormtrack seasonality excluding the midwinter minimum (Nakamura, 1992; Chang *et al.*, 2002). In addition, Kushner & Held (1998) showed that the seasonality of the stormtracks in the lower troposphere follow a down-gradient diffusive model, i.e. they follow the seasonality of the time-mean temperature gradient. Finally, O'Gorman (2010) showed that the seasonality of zonal-mean stormtrack intensity follows Mean Available Potential Energy (MAPE). MAPE is related to the vertical and meridional structure of the zonal- and time-mean temperature and is proportional to the square of the Eady growth rate (O'Gorman & Schneider, 2008).

The second group focuses on Moist Static Energy (MSE). Recently, Barpanda & Shaw (2017) and Shaw *et al.* (2018), hereafter B17 and S18, developed a framework for zonal-mean stormtrack position and intensity based on the MSE budget. It provides a clear connection between stormtracks and seasonal insolation. In particular, stormtrack position

and intensity are related to net energy input (top of atmosphere radiation minus surface fluxes and atmospheric storage) and MSE transport by the stationary circulation (mean meridional circulation and stationary eddies). B17 and S18 showed that the MSE framework could be used to test the hypothesis that top-of-atmosphere (TOA) insolation controls stormtrack seasonality. The test revealed insolation controls the phase of stormtrack seasonality but not the amplitude. The MSE framework was subsequently used diagnostically to show shortwave absorption (TOA minus surface shortwave) dominates the seasonality of stormtrack intensity and the factor accounting for the hemispheric difference was surface heat fluxes (turbulent surface latent and sensible heat flux plus surface longwave radiation), which are part of the net energy input. Surface heat fluxes are out of phase with shortwave absorption in the SH leading to small seasonal intensity whereas surface heat fluxes are in phase with shortwave absorption in the NH leading to large seasonal intensity. According to the MSE framework, the dominant factor accounting for hemispheric differences in seasonal position is the stationary eddy MSE flux, which offsets the equator-to-pole energy imbalance implied from the net energy input.

It is difficult to interpret the results mentioned above for several reasons. First, the seasonal mean temperature-stormtrack relationship is not causal because stormtracks' feedback on the mean temperature structure (Hoskins & Valdes, 1990; Shaw *et al.*, 2016). Second, stormtracks interact with components of the MSE framework: stormtracks produce clouds which impact the cloud radiative effect (Ceppi & Hartmann, 2015), stormtracks affect the amplitude of stationary eddies (Held *et al.*, 2002) and eddy momentum fluxes drive the Ferrel cell (Schneider, 2006). Nevertheless the MSE framework is appealing because it includes external control parameters, e.g. insolation and surface albedo. These parameters can form the basis of predictions as shown by B17 and S18. Unfortunately, frameworks based on mean temperature cannot be easily related to external parameters, such as insolation, which is the main driver of stormtrack seasonality.

Here we hypothesize that surface fluxes (surface shortwave radiation minus surface heat fluxes) modulate the seasonality of zonal-mean stormtracks. We focus on surface fluxes because 1) they can be controlled by an external parameter (the mixed layer depth) in slab-ocean aquaplanet models and in Energy Balance Models (EBMs) and 2) they affect the seasonality of surface heat fluxes, which S18 showed was important for the hemispheric difference in seasonal stormtrack intensity. We are also motivated by previous work that demonstrated the impact of mixed layer depth on the zonally-symmetric slab-ocean aquaplanet climate. In particular, aquaplanet simulations with a 50 m mixed layer depth capture the seasonality of atmospheric temperature in the SH, which is mostly ocean and therefore has a large effective heat capacity (Donohoe *et al.*, 2014). Whereas aquaplanet simulations with a 1 m mixed layer depth capture the seasonality of the Asian Monsoon in the NH, which has more land and therefore a small effective heat capacity (Bordoni & Schneider, 2008).

We test our hypothesis by varying the mixed layer depth in zonally-symmetric slab-ocean aquaplanet simulations without ocean energy transport. In addition we vary the mixed layer depth in an EBM to understand connections to stormtrack frameworks based on mean surface temperature. We focus on zonally-symmetric stormtracks as a first step in understanding the different hemispheric seasonality of zonal-mean stormtracks on Earth. While the NH stormtrack is clearly influenced by stationary eddies, zonally-symmetric dynamics may still be useful if the impact of stationary circulations that are present on Earth are similar to the zonal-mean meridional circulation in the zonally-symmetric aquaplanet.

The chapter is organized as follows. We review the MSE framework and outline our hypotheses in section 2. We describe the details of the aquaplanet and EBM simulations in section 3. In section 4, we test our hypotheses using the aquaplanet simulations, fully diagnose stormtrack seasonality using the MSE framework and relate the aquaplanet results to the observed stormtracks. We also examine the response of the EBM to changes in mixed layer depth, including its impact on mean surface temperature. The conclusions and

discussion are summarized in section 5.

3.2 Energetic framework and hypotheses

B17 and S18 derived an energetic framework for stormtrack position and intensity based on the atmospheric MSE budget:

$$F_{MM} + F_{SE} + F_{TE} = \left(\overline{[F_{EIA}]}\right) - \partial_t \langle \overline{[h]} \rangle \equiv F_{NE}, \tag{3.1}$$

where $F_{MM} = \partial_y \langle [\overline{v}] [\overline{m}] \rangle$, $F_{SE} = \partial_y \langle [\overline{v}^* \overline{m}^*] \rangle$ and $F_{TE} = \partial_y \langle \left[\overline{v'm'}\right] \rangle$ are the MSE flux divergence by the mean meridional circulation, stationary and transient eddies; v is meridional wind; m is MSE ($m = c_p T + Lq + \Phi$), where c_p is specific heat of air at constant pressure, T is temperature, L is the latent heat of vaporization, q is specific humidity, and Φ is geopotential; the overbar and square brackets denote monthly and zonal averages, respectively, with the prime and the asterisk representing deviations from those averages, respectively; angle brackets denote mass-weighted vertical integration; $\partial_y (\cdot) \equiv \partial_\phi \{cos\phi (\cdot)\} / a\, cos\phi$ is the meridional divergence in spherical coordinates, where ϕ is latitude and a is the radius of Earth; t is time; and h is the thermal energy ($h = c_p T + Lq$). The net energy input F_{NE} is the difference between energy input to the atmosphere [$F_{EIA} = F_{TOA} - F_{SFC}$] and atmospheric storage $\partial_t \langle \overline{[h]} \rangle$, i.e. $F_{NE} = F_{TOA} - F_{SFC} - \partial_t \langle \overline{[h]} \rangle$ where F_{TOA} is TOA radiation and F_{SFC} is surface fluxes. The net energy input can be further decomposed following Donohoe & Battisti (2013), i.e.

$$F_{NE} = F_{SWABS} + F_{SHF} - F_{OLR} - \partial_t \langle \overline{[h]} \rangle \tag{3.2}$$

where F_{SWABS} is shortwave absorption in the atmosphere (TOA minus surface shortwave radiation), F_{SHF} is surface heat flux (surface longwave radiation plus turbulent surface latent and sensible heat fluxes) and F_{OLR} is outgoing longwave radiation (OLR).

The stormtrack position (ϕ_s) is identified as the latitude where the transient eddy MSE flux divergence is zero, i.e. $F_{TE}|_{\phi_s} = 0$. The stormtrack intensity (I) is the value of zonal-mean transient eddy MSE flux at the stormtrack position, i.e. $I = 2\pi a\, cos\phi_s \langle [\overline{v'm'}] \rangle|_{\phi_s}$. Note that storm-track intensity is negative in the SH and thus $\Delta I > 0$ indicates a weakening of the SH stormtrack. S18 showed that defining stormtracks using a monthly average produced similar results to defining them using a 10-day high pass filter (see Appendix A of S18). We find similar agreement in our aquaplanet simulations (see Appendix A in section‘3.6.1, Figs. 3.15 & 3.16).

According to the MSE framework, a change in stormtrack intensity (ΔI) is decomposed into contributions from net energy input integrated poleward of the stormtrack and MSE fluxes by the mean meridional circulation and stationary eddies at the stormtrack position:

$$\Delta I = \Delta I_{NE} - \Delta I_{MM} - \Delta I_{SE}, \tag{3.3}$$

where $I_{NE} = 2\pi a^2 cos\phi \int_{\pi/2}^{\phi_s} cos\phi F_{NE} d\phi$, $I_{MM} = 2\pi a cos\phi_s \langle [\overline{v}]\, [\overline{m}] \rangle|_{\phi_s}$ and $I_{SE} = 2\pi a cos\phi_s \langle [\overline{v}^* \overline{m}^*] \rangle|_{\phi_s}$ (S18, section 2). Similarly, a change in stormtrack position ($\Delta\phi$) is decomposed into contributions from net energy input ($\Delta\phi_{NE}$), mean meridional circulation ($\Delta\phi_{MM}$), stationary eddies ($\Delta\phi_{SE}$) and a cross term ($\Delta\phi_{CT}$):

$$\Delta\phi = \Delta\phi_{NE} + \Delta\phi_{MM} + \Delta\phi_{SE} + \Delta\phi_{CT}. \tag{3.4}$$

where $\Delta\phi_{CT}$ arises from nonlinearities (see B17 section 2 Method 2 for details).

To illustrate a diagnostic application of the MSE framework, we quantify the seasonal evolution of stormtrack intensity as an anomaly relative to the annual mean for 2000 to 2015. (Note, this seasonal analysis is different from S18 who quantified month-to-month seasonality.) Following S18, we combine Clouds and the Earth's Radiant Energy System (CERES) energy balanced and filled (EBAF) radiation (TOA longwave, shortwave and sur-

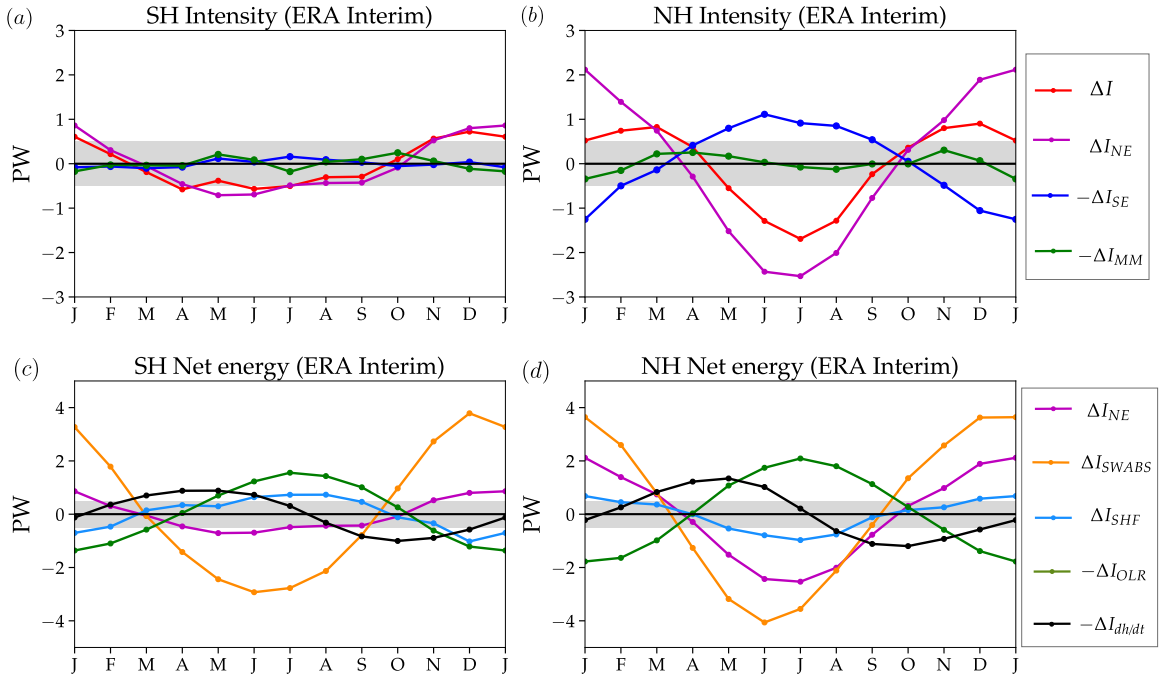

Figure 3.1: (a,b) Decomposition of stormtrack intensity as an anomaly relative to the annual mean (ΔI) into contributions from net energy input (ΔI_{NE}), stationary eddies (ΔI_{SE}) and mean meridional circulation (ΔI_{MM}). (c,d) Decomposition of net energy input (ΔI_{NE}) contribution to stormtrack intensity anomaly into atmospheric shortwave absorption (ΔI_{SWABS}), surface heat flux (ΔI_{SHF}), outgoing longwave radiation ($-\Delta I_{OLR}$), and atmospheric storage ($-\Delta I_{dh/dt}$). Left panels show SH and right panels show NH for ERA-Interim Reanalysis.

face shortwave) data with MSE flux and atmospheric storage data from ERA-Interim. The surface heat flux is calculated as a residual of the MSE budget (1). Following S18, when computing the contributions to I_{NE} the global mean is subtracted prior to computing the spatial integral over the polar cap to ensure the implied energy transport at ϕ_s is independent of whether the integral is computed from the South Pole to ϕ_s or the North Pole to ϕ_s. In addition, the reanalysis uncertainty is defined as the difference between ERA-Interim and NCEP over the 2000 to 2015 period and is ~ 0.3 PW.

According to the MSE framework, the seasonality of SH stormtrack intensity is negligible and follows the evolution of net energy input (compare red and magenta lines, Fig. 3.1a).

The seasonality of NH stormtrack intensity is large and mostly follows the evolution of net energy input (compare red and magenta lines, Fig. 3.1b). Stationary eddies contribute to a midwinter minimum in the NH (blue line, Fig. 3.1b). Therefore, from a zonally-symmetric perspective, the different hemispheric seasonality of stormtrack intensity is connected to the seasonality of net energy input. Decomposing the net energy input following (3.2) shows that shortwave absorption (insolation) dominates seasonality in both hemispheres (orange line, Fig. 3.1c,d). In the SH, the seasonality of net energy input is negligible because surface heat fluxes are out of phase with shortwave absorption along with OLR and atmospheric storage (Fig. 3.1c). In contrast, in the NH the seasonality of net energy input is large because surface heat fluxes are in phase with shortwave absorption (Fig. 3.1d). Thus, the different hemispheric seasonality of stormtrack intensity is dominated by the different seasonality of surface heat fluxes. Shortwave absorption is also somewhat different between the hemispheres but it is not important throughout the seasonal cycle. OLR and atmospheric storage do not exhibit hemispheric differences larger than reanalysis uncertainty.

To build a causal understanding of surface heat fluxes for stormtrack seasonality we focus on surface fluxes. Surface fluxes and surface heat fluxes are connected via the surface energy budget:

$$F_{SFC} = F_{SW_{sfc}} - F_{SHF} = d\rho_o c_{p_o} \frac{\partial T_s}{\partial t} + \nabla \cdot \mathbf{F}_o \tag{3.5}$$

where $F_{SW_{sfc}}$ is surface shortwave radiation, d is mixed layer depth of the ocean, ρ_o is density of water, c_{p_o} is specific heat capacity of water, T_s is sea surface temperature (SST) and $\nabla \cdot \mathbf{F}_o$ is the ocean energy flux convergence. If ocean energy transport ($\mathbf{F}_o$) is negligible (a reasonable assumption for the extratropics and seasonal timescale, see Figs. 4c and 5c in Roberts *et al.*, 2017) then the mixed layer depth controls surface fluxes.

Assuming the stationary circulation and atmospheric storage contributions are negligible, we hypothesize the mixed layer depth (surface fluxes) modulates stormtrack seasonality as follows:

1. If the mixed layer depth is large then surface fluxes become large enough to compensate TOA radiation, i.e. $\Delta F_{SFC} \approx \Delta F_{TOA}$, the seasonality of net energy input is small, shortwave absorption is out of phase with surface heat fluxes, and stormtrack seasonality is small.

2. If the mixed layer depth is small then surface fluxes are small, i.e. $\Delta F_{SFC} < \Delta F_{TOA}$, the seasonality of net energy input is large, shortwave absorption is in phase with surface heat fluxes, and stormtrack seasonality is large.

The phase relationships between shortwave absorption and surface heat fluxes were deduced as follows. If the mixed layer depth is large then

$$\begin{aligned} \Delta F_{SFC} \approx \Delta F_{TOA} \quad &\Rightarrow \quad \Delta F_{TOA} \approx F_{SW_{sfc}} - \Delta F_{SHF} \\ &\Rightarrow \quad \Delta F_{SWABS} - \Delta F_{OLR} \approx -\Delta F_{SHF} \\ &\Rightarrow \quad \Delta F_{SWABS} \approx -\Delta F_{SHF} \end{aligned} \tag{3.6}$$

assuming shortwave absorption dominates over OLR. If the mixed layer depth is small then

$$\begin{aligned} \Delta F_{SFC} \approx 0 \quad &\Rightarrow \quad \Delta F_{SW,sfc} - \Delta F_{SHF} \approx 0 \\ &\Rightarrow \quad \Delta F_{SW,sfc} \approx \Delta F_{SHF} \\ &\Rightarrow \quad \Delta F_{SWABS} \approx \Delta F_{SHF} \end{aligned} \tag{3.7}$$

assuming surface shortwave radiation is in phase with shortwave absorption.

The different mixed layer depth limits are relative to a critical depth, which we estimate using a scaling analysis of the MSE budget that assumes TOA insolation and surface fluxes are the same order of magnitude, i.e.

$$d_c \approx \frac{(1-\alpha)S_0 T}{\rho_o c_{p_o} T_s} \approx 10 \text{ m} \tag{3.8}$$

where α = 0.3 is the planetary albedo, S_0 = 500 Wm^{-2} is the maximum insolation in the extratropics, T_s = 300 K and T = 1 year. Here we use the absolute values instead of seasonal changes following scaling conventions in Vallis (2006).

3.3 Model simulations

3.3.1 Aquaplanet

We perform zonally-symmetric slab-ocean aquaplanet simulations using two different General Circulation Models (GCMs): (1) Isca (Vallis *et al.*, 2018) and (2) Geophysical Fluid Dynamics Laboratory, Atmospheric Model 2.1 (GFDL) (Anderson *et al.*, 2004; Delworth *et al.*, 2006). The Isca simulations use clear-sky RRTMG radiation (Mlawer *et al.*, 1997), the Betts Miller convection scheme (Betts & Miller, 1993) and are configured with spectral T42 resolution and 40 unevenly spaced sigma levels. A constant planetary albedo of α = 0.3 is prescribed in Isca. The GFDL simulations use a multi-band radiation parameterization (Freidenreich & Ramaswamy, 1999), the relaxed Arakawa Schubert convection scheme (Moorthi & Suarez, 1992) and are configured with finite volume grid with uniform horizontal resolution of 2.8° (equivalent to T42 spectral), and 48 unevenly spaced sigma levels. Thus the two GCMs differ in their convection schemes and the inclusion of cloud radiative effects.

Both aquaplanets are configured as follows: ocean energy flux convergence is zero, obliquity is 23.4°, eccentricity is zero and the concentration of greenhouse gases are: CO_2 = 348 ppmv, CH_4 = 1650 ppbv, N_2O = 306 ppbv, and CFCs are zero. A climatological stratospheric ozone layer is also added to the model which is hemispherically and zonally symmetric following Geen *et al.* (2018). We test the hypotheses outlined in section 2 by varying the mixed layer depth from 4 m to 100 m. All simulations are run for 40 years with the results representing the average over the last 30 years and both hemispheres (with SH data shifted by 6 months). The two GCMs yield consistent results, thus we present the Isca simulations

in the section 3.4 and the GFDL simulations in Appendix B (see section 3.6.2).

3.3.2 Energy Balance Model

We use the Climlab EBM (Rose, 2018), which solves an equation for surface temperature (T_s) based on the TOA energy budget:

$$C\frac{\partial T_s}{\partial t} = (1-\alpha)Q - (A + BT_s) + \frac{1}{cos\ \phi}\frac{\partial}{\partial \phi}\left(D_{ebm}\frac{\partial T_s}{\partial \phi}cos\ \phi\right) \tag{3.9}$$

where $C = d\rho_o c_{p_o}$ is the effective (ocean plus atmosphere) heat capacity, α is the planetary albedo, Q is the seasonally evolving solar insolation, $A + BT_s$ is a parameterization of OLR, D_{ebm} is the total diffusivity in units of $Wm^{-2}K^{-1}$. We used the following parameter values: A = 210 Wm^{-2}, B = 2 $Wm^{-2}K^{-1}$, and $\alpha = 0.3$. Following Mbengue & Schneider (2018), the total diffusivity is

$$D_{ebm}(\phi, \phi_h) = D_x + (D_t - D_x)S(\phi, \phi_h) \tag{3.10}$$

where $\phi_h = 25°$ is the Hadley Cell edge, $D_x = 1.6\ Wm^{-2}K^{-1}$ is the extratropical diffusivity, $D_t = 3.2\ Wm^{-2}K^{-1}$ is the tropical diffusivity and

$$S(\phi, \phi_h) = \frac{1}{2}\left[1 - \tanh\left(\pi\frac{\phi - \phi_h}{\phi_h}\right)\tanh\left(\pi\frac{\phi + \phi_h}{\phi_h}\right)\right]$$

.

The EBM is a dry model, thus the stormtrack is defined differently than in the MSE framework. The stormtrack position (ϕ_s) is defined as the latitude where the extratropical eddy energy flux divergence is zero, i.e. $\frac{\partial}{\partial \phi}\left(cos\ \phi\frac{\partial T_s}{\partial \phi}\right)\Big|_{\phi_s} = 0$. The stormtrack intensity (I_{EBM}) is the value of extratropical energy flux at the stormtrack position, i.e. $I_{EBM} = -2\pi a^2\ cos\ \phi_s\ D_x\frac{\partial T_s}{\partial \phi}\Big|_{\phi_s}$. In the EBM, TOA energy balance means that the intensity can be

decomposed as follows

$$\Delta I_{EBM} = \Delta I_{NE} = \Delta I_{TOA} - \Delta I_{CdT/dt} \tag{3.11}$$

where ΔI_{TOA} and $\Delta I_{CdT/dt}$ are the TOA radiation and the effective storage contributions, respectively. In the EBM the mixed layer depth controls the effective storage contribution, which cannot be separated into surface flux (ocean storage) and atmospheric storage contributions because the EBM is based on TOA energy balance.

3.4 Results

3.4.1 Testing mixed layer depth hypothesis in the aquaplanet

The slab-ocean aquaplanet simulations show that in the limit of large mixed layer depth TOA and surface fluxes are of similar magnitude, i.e. $\Delta F_{TOA} \approx \Delta F_{SFC}$ (Fig. 3.2a), and net energy input is small (Fig. 3.2b). Shortwave absorption is five months out of phase with surface heat fluxes (Fig. 3.2c). This agrees well with the hypothesized six month phase lag between shortwave absorption and surface heat fluxes for large mixed layer depth. The one-month discrepancy is attributed to the small but non-zero OLR contribution (see equation 6). Thus the simulations confirm the large mixed layer depth hypothesis thus far. In addition, the slab-ocean aquaplanet simulations show that in the limit of small mixed layer depth TOA fluxes are larger than surface fluxes, i.e. $\Delta F_{TOA} > \Delta F_{SFC}$ (Fig. 3.2a), and net energy input is large (Fig. 3.2b). The change in surface flux with mixed layer depth is not associated with surface shortwave radiation (compare blue and dashed red lines, Fig. 3.2a). Furthermore, shortwave absorption is in phase with surface heat fluxes (Fig. 3.2c) for small mixed layer depth. Thus the simulations also confirm the small mixed layer depth hypothesis thus far. Finally, the critical depth, estimated as the e-folding depth of the net energy input as a function of mixed layer depth, is 6.5 m (black vertical line, Fig. 3.2b).

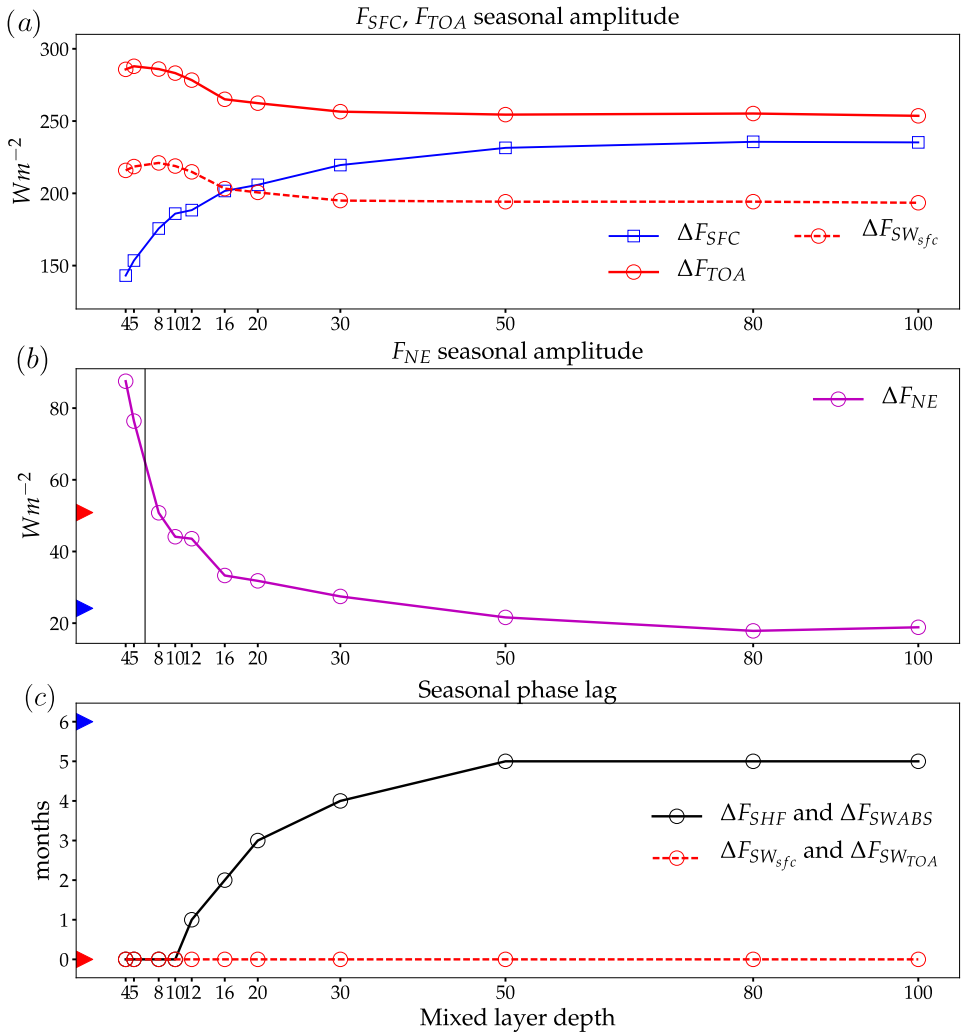

Figure 3.2: Seasonal amplitude of (a) TOA radiation (red), surface flux (blue), surface shortwave radiation (red dashed) and (b) net energy input (magenta) as a function of slab-ocean mixed layer depth. The black vertical line denotes e-folding depth for net energy input. (c) Phase difference between seasonal evolution of atmospheric shortwave absorption and surface heat flux (black) and surface shortwave radiation and TOA shortwave radiation (red dashed) as a function of slab-ocean mixed layer depth. Data from Isca simulations. The triangles on the y axis denote values in the NH (red) and SH (blue) in the ERA-Interim reanalysis.

This agrees well with the 10 m scaling estimate (see equation 3.8).

In what follows we choose 5 m and 50 m as representative small and large slab-ocean mixed layer depths. The large mixed layer depth limit is reminiscent of the SH where the seasonality of net energy input is small and surface heat fluxes are out of phase with shortwave absorption (blue triangles, Fig. 3.2b,c). In contrast, the small mixed layer depth limit is reminiscent of the NH where the seasonality of net energy input is large and surface heat fluxes are in phase with shortwave absorption (red triangles, Fig. 3.2b,c).

Effect of mixed layer depth on stormtrack intensity

The slab-ocean aquaplanet simulations with large mixed layer depth exhibit small seasonality of stormtrack intensity (red line, Fig. 3.3a) following small seasonality of net energy input (magenta line, Fig. 3.3a). The seasonality of net energy input is small because shortwave absorption is out of phase with surface heat fluxes and OLR (compare orange, blue and green lines, Fig. 3.3b). The surface heat flux seasonality is dominated by the latent heat flux contribution (Fig. 3.4a). In addition, the mean meridional circulation (green line, Fig. 3.3a), stationary eddy (blue line, Fig. 3.3a) and atmospheric storage (black line, Fig. 3.3b) contributions are small. Thus the simulations confirm the intensity hypothesis for large mixed layer depth.

The slab-ocean aquaplanet simulations with small mixed layer depth exhibit large stormtrack seasonality (red line, Fig. 3.3c) following the large seasonality of net energy input (magenta line, Fig. 3.3c). Net energy input is large because shortwave absorption is in phase with surface heat fluxes (compare orange and blue lines, Fig. 3.3d). The surface heat flux seasonality is very large and dominated by the latent heat flux contribution (Fig. 3.4b). However, contrary to the assumptions underlying our hypothesis the mean meridional circulation (green line, Fig. 3.3c) and atmospheric storage (black line, Fig. 3.3d) contributions are large. Thus, the simulations do not exactly confirm the intensity hypothesis for small

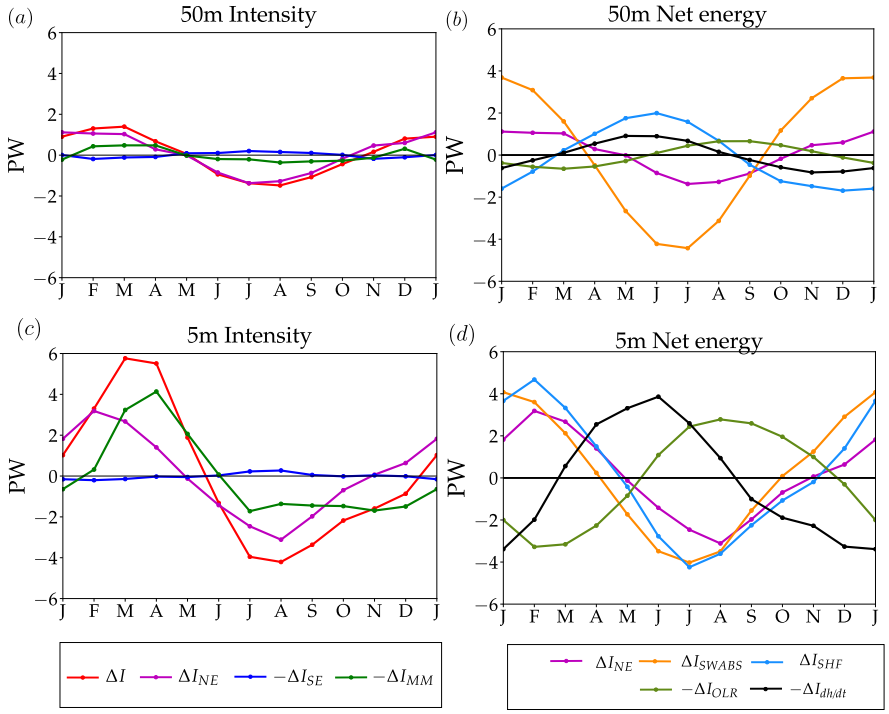

Figure 3.3: (a,c) Decomposition of stormtrack intensity as an anomaly relative to the annual mean (ΔI) into contributions from net energy input (ΔI_{NE}), stationary eddies (ΔI_{SE}) and mean meridional circulation (ΔI_{MM}). (b,d) Decomposition of net energy input (ΔI_{NE}) contribution to stormtrack intensity anomaly into atmospheric shortwave absorption (ΔI_{SWABS}), surface heat flux (ΔI_{SHF}), outgoing longwave radiation ($-\Delta I_{OLR}$) and atmospheric storage ($-\Delta I_{dh/dt}$). Data from Isca simulations with 50 m (top) and 5 m (bottom) slab-ocean mixed layer depth.

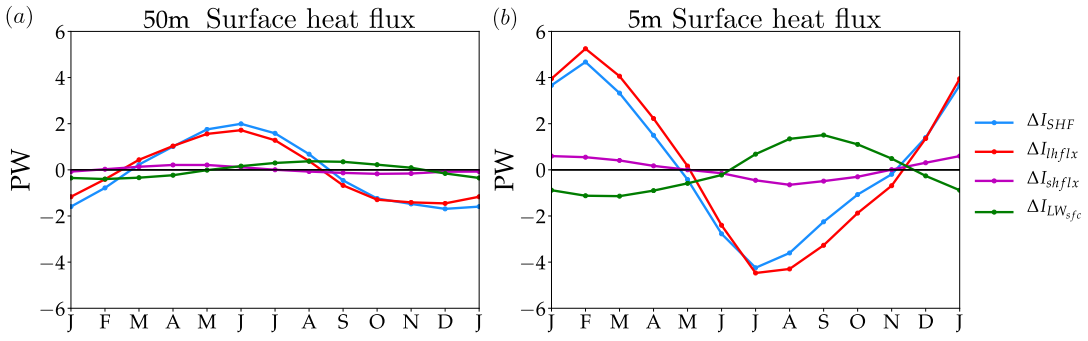

Figure 3.4: Decomposition of surface heat flux contribution to stormtrack intensity as an anomaly relative to the annual mean (ΔI_{SHF}) into latent heat flux (ΔI_{lhflx}), sensible heat flux (ΔI_{shflx}) and surface longwave radiation ($\Delta I_{LW_{sfc}}$) contributions. Data from Isca simulations with 50 m (left) and 5 m (right) slab-ocean mixed layer depth.

mixed layer depth.

The slab-ocean aquaplanet simulations show that in the limit of small mixed layer depth, surface heat fluxes are not solely responsible for the large seasonality of stormtrack intensity, the mean meridional circulation and atmospheric storage contributions are both important. The large atmospheric storage contribution with small mixed layer depth is consistent with the seasonal amplitude of atmospheric temperature increasing with decreasing mixed layer depth (Donohoe *et al.*, 2014). In order to better understand the mean meridional circulation contribution to stormtrack intensity for small mixed layer depth we consider two additional questions: 1) Is the mean meridional circulation contribution driven locally by Ferrel cell dynamics or non-locally via interactions with the Hadley cell? and 2) Is the seasonality of the mean meridional circulation MSE flux associated with thermodynamic or dynamic changes?

In order to quantify the role of non-local Hadley cell seasonality for the mean meridional MSE flux in the extratropics, we configure two additional slab-ocean aquaplanet simulations: 1) 5 m mixed layer depth in the tropics (20°S to 20°N) with 50 m mixed layer depth elsewhere and 2) 50 m mixed layer depth in the tropics with 5 m mixed layer depth elsewhere. The results show that the seasonal stormtrack intensity and mean meridional circulation contribution are mostly independent of tropical mixed layer depth (Fig. 3.5). Thus, local Ferrel cell dynamics control the mean meridional circulation contribution to stormtrack intensity for small mixed layer depth.

In order to understand the importance of thermodynamic versus dynamic changes for the seasonality of mean meridional circulation MSE flux, we decompose the flux into dynamic and thermodynamic contributions (cf. Seager *et al.*, 2010), i.e.

$$\Delta\langle[\bar{v}]\,[\bar{m}]\rangle \approx \underbrace{\langle(\Delta\,[\bar{v}])\,[m]_a\rangle}_{dynamic} + \underbrace{\langle[v]_a\,\Delta\,([\bar{m}])\rangle}_{thermodynamic} \tag{3.12}$$

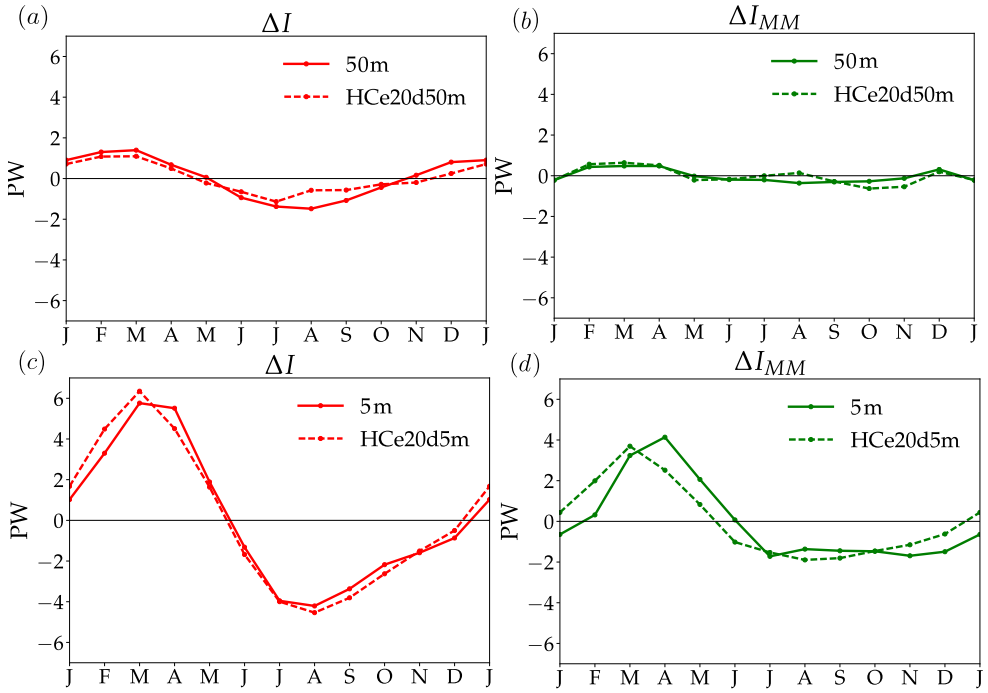

Figure 3.5: Seasonal evolution of (a) stormtrack intensity (ΔI) as an anomaly relative to the annual mean and (b) contribution from mean meridional circulation (ΔI_{MM}) with 50 m slab-ocean mixed layer depth (solid) and HC experiment with 5 m mixed layer depth equatorward of 20° and 50 m depth elsewhere (dashed). Seasonal evolution of (c) stormtrack intensity (ΔI) as an anomaly relative to the annual mean and (d) contribution from mean meridional circulation with 5 m slab-ocean mixed layer depth (solid) and HC experiment with 50 m mixed-layer depth equatorward of 20° and 5 m elsewhere (dashed). Data from Isca simulations.

where $[m]_a$ and $[v]_a$ are annual, zonal-mean MSE and meridional wind respectively. Overall, the dynamic contribution dominates over the thermodynamic contribution for small mixed layer depth (Fig. 3.6). Thus, the seasonal dynamical changes in the Ferrel cell are important for stormtrack intensity in the limit of small mixed layer depth.

In order to better understand what controls the dynamical changes in the Ferrel cell, we use the zonal-mean zonal momentum budget to decompose the mean meridional flow into mean meridional circulation, stationary eddy and transient eddy contributions (cf. Seager

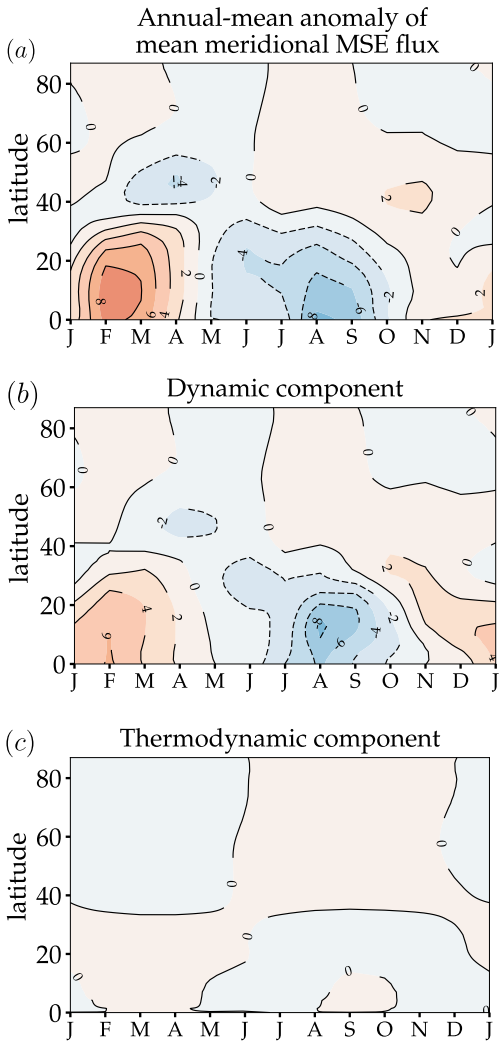

Figure 3.6: Seasonal evolution of (a) mean meridional MSE flux ($\langle [\overline{v}]\,[\overline{m}] \rangle$) contribution to stormtrack intensity as an anomaly relative to the annual mean decomposed into (b) dynamic $\langle (\Delta\,[\bar{v}])\,[m]_a \rangle$ and (c) thermodynamic $\langle [v]_a\,\Delta\,([\bar{m}]) \rangle$ contributions for Isca simulation with 5 m slab-ocean mixed layer depth.

et al., 2003; Schneider & Bordoni, 2008):

$$
\begin{aligned}
[\overline{v}] = & \underbrace{\frac{1}{f}\left[\frac{\partial[\overline{u}]}{\partial t} - \left[\overline{\zeta}\right][\overline{v}] + [\overline{\omega}]\frac{\partial[\overline{u}]}{\partial p}\right]}_{[\overline{v_{MM}}]} \\
& + \underbrace{\frac{1}{f}\left[\frac{\partial[\overline{u}^*\overline{\omega}^*]}{\partial p} + \frac{1}{a\ cos^2\phi}\frac{\partial}{\partial\phi}\left(cos^2\phi\,[\overline{u}^*\overline{v}^*]\right)\right]}_{[\overline{v_{SE}}]} \\
& + \underbrace{\frac{1}{f}\left[\frac{\partial[\overline{u'\omega'}]}{\partial p} + \frac{1}{a\ cos^2\phi}\frac{\partial}{\partial\phi}\left(cos^2\phi\,[\overline{u'v'}]\right)\right]}_{[\overline{v_{TE}}]}
\end{aligned}
\tag{3.13}
$$

where f is the Coriolis parameter, ζ is relative vorticity, and ω is vertical velocity. Overall, the transient eddy component ($[\overline{v_{TE}}]$) dominates the seasonality of the mean meridional flow (Ferrel cell) in the upper troposphere (250 hPa) for small mixed layer depth (Fig. 3.7) consistent with previous work (Bordoni & Schneider, 2008). The mean meridional flow in the upper troposphere reaches its extremum during April (Fig. 3.7a) consistent with the mean meridional circulation contribution to stormtrack intensity (green line, Fig. 3.3c). According to the momentum budget decomposition, the mean meridional flow extremum in April is due to both the transient eddy ($[\overline{v_{TE}}]$) and mean meridional circulation ($[\overline{v_{MM}}]$) contributions.

Effect of mixed layer depth on stormtrack position

The slab-ocean aquaplanet simulations with large mixed layer depth exhibit small seasonal stormtrack shift (red line, Fig. 3.8a) following the small seasonality of net energy input (magenta, Fig. 3.8a). The mean meridional circulation (green line, Fig. 3.8a), stationary eddy (blue line, Fig. 3.8a) and atmospheric storage (black line, Fig. 3.8a) contributions are small. Thus the simulations confirm the stormtrack position hypothesis for the large mixed layer depth limit.

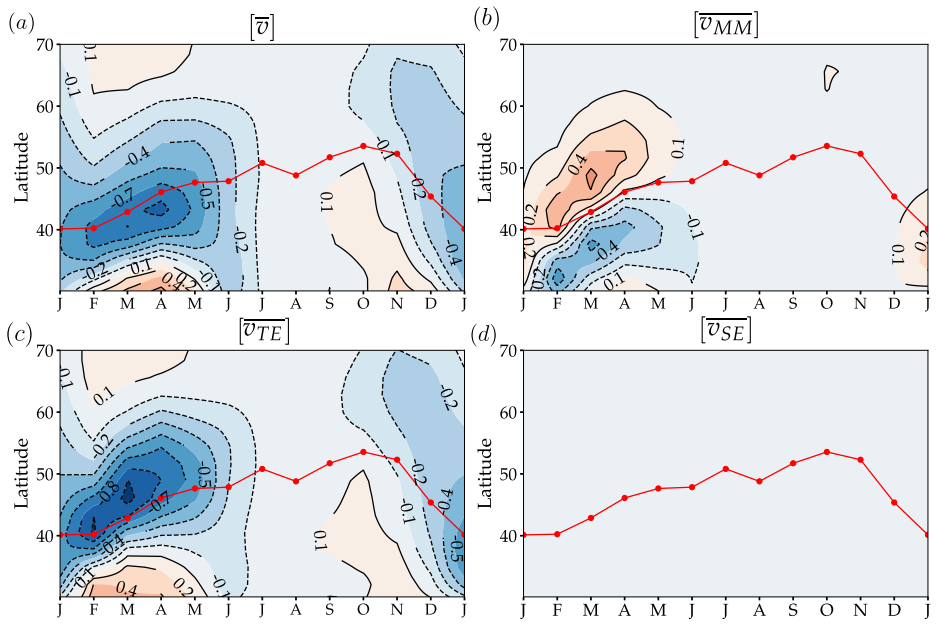

Figure 3.7: Decomposition of the (a) mean meridional flow at 250 hPa into contributions from the (b) mean meridional circulation ($[\overline{v_{MM}}]$), (c) transient eddy ($[\overline{v_{TE}}]$) and (d) stationary eddy ($[\overline{v_{SE}}]$) momentum flux divergence using the zonal-mean zonal momentum budget for Isca simulation with 5 m slab-ocean mixed layer depth.

The slab-ocean aquaplanet simulations with small mixed layer depth exhibit a large seasonal stormtrack shift (red line, Fig. 3.8b). The seasonal shift is so large that the MSE framework breaks down (the cross term is very large). Therefore we cannot confirm that the large shift is due to large net energy input as hypothesized. However, it is clear that the mean meridional circulation (green line, Fig. 3.8b) and cross term (black line, Fig. 3.8b) contributions are not small.

In order to avoid large shifts and a breakdown of the MSE framework, we quantify the seasonal stormtrack shift between large (50 m) and intermediate (10 m) mixed layer depths. Since the annual mean stormtrack position for the intermediate mixed layer depth is poleward of the position for the large depth, the shift difference is always positive. The intermediate minus large mixed layer depth shows that the net energy input contribution dominates during summer (June, July and August) and the mean meridional circulation

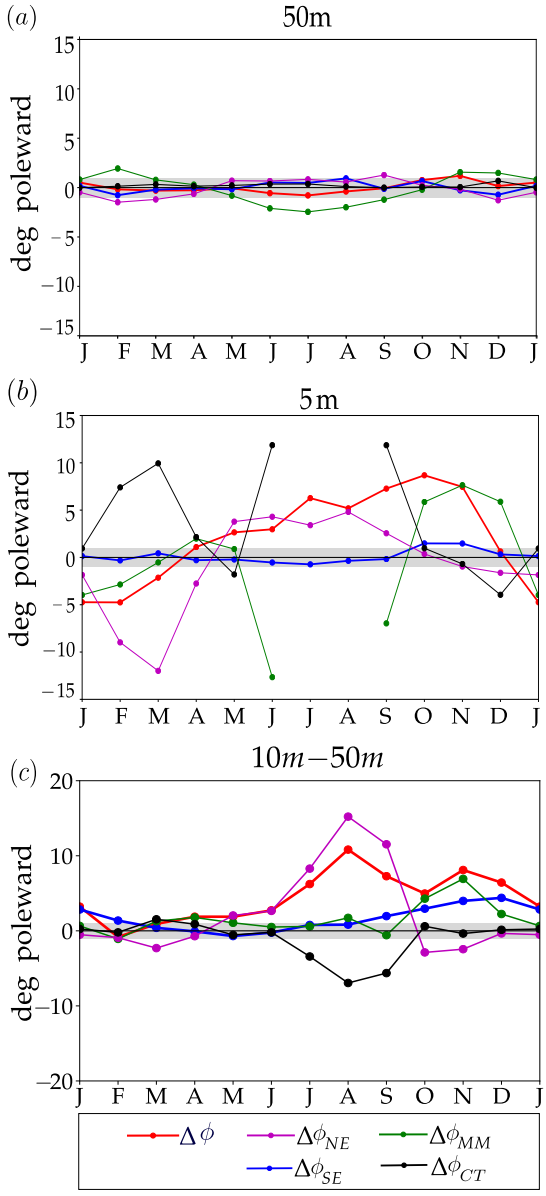

Figure 3.8: Seasonal evolution of stormtrack position as an anomaly relative to the annual mean ($\Delta\phi$) decomposed into contributions from net energy input ($\Delta\phi_{NE}$), mean meridional circulation ($\Delta\phi_{MM}$) and stationary eddies ($\Delta\phi_{SE}$) for Isca simulations with (a) 50 m, (b) 5 m, and (c) 10 m minus 50 m slab-ocean mixed layer depth.

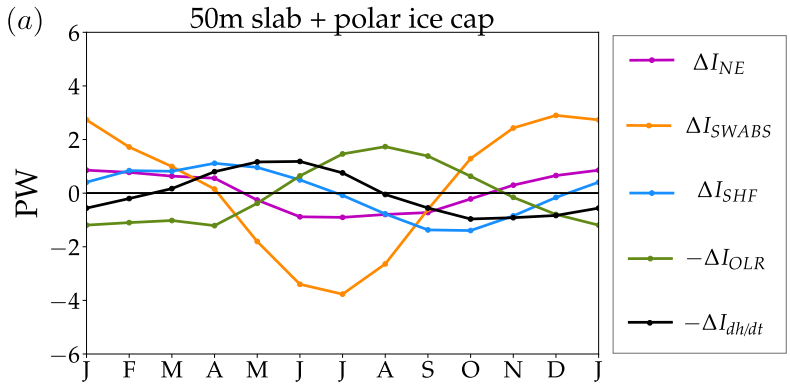

Figure 3.9: As in Fig. 3.3c but for 50 m slab-ocean mixed layer depth equatorward of 55° and 2m depth poleward of 55°.

contribution dominates during November (Fig. 3.8c). Thus, consistent with the intensity results, in the limit of small mixed layer depth surface fluxes are not solely responsible for seasonal shifts of the stormtrack, the mean meridional circulation contribution is also important and is dominated by seasonal dynamical changes in the Ferrel cell.

Connection to the observed stormtracks

The stormtrack seasonality for the slab-ocean aquaplanet simulation with large mixed layer depth exhibits several similarities with the SH stormtrack on Earth. First, the large mixed layer depth simulation reproduces the small seasonality of stormtrack intensity and position (compare red lines, Figs. 3.1a, 3.3a and 3.8a) associated with the small seasonality of net energy input (compare magenta lines, Figs. 3.1a and 3.3a). Second, the large mixed layer depth simulation also reproduces the out-of-phase relationship between the shortwave absorption and surface heat flux contributions to seasonal intensity seen in the SH (compare orange and blue lines, Figs. 3.1c and 3.3b). However, the amplitudes of the OLR and surface heat flux contributions to intensity for the large mixed layer depth simulation are different than those in the SH (compare green and blue lines, Fig. 3.1c to 3.3b). More specifically, the surface heat flux contribution is larger than the OLR contribution in the SH, whereas

the opposite is true for the large mixed layer depth simulation.

An important difference between the SH and an aquaplanet simulation with large mixed layer depth is Antarctica. To test whether Antarctica is important for stormtrack seasonality in the SH, we configured a simulation with a large mixed layer depth (50 m) and a polar region that mimics Antarctica. The Antarctic region is mimicked by a region with high albedo (α = 0.7) small mixed layer depth (2 m) and zero latent heat flux poleward of 55 degrees (latent heat flux is multiplied by β = 0 poleward of 55 degrees). The seasonal stormtrack intensity with a polar region that mimics Antarctica exhibits an OLR contribution which is larger than the surface heat flux contribution consistent with the SH (Fig. 3.9). Thus, the stormtrack seasonality in a zonally-symmetric slab-ocean aquaplanet with a large mixed layer depth (50 m) and a polar region that mimics Antarctica is a good idealization of the SH stormtrack.

The stormtrack seasonality for the small mixed layer depth slab-ocean aquaplanet simulation is large similar to the NH stormtrack (compare red lines, Figs. 3.1b, 3.3c and 3.8b) and associated with the large seasonality of net energy input (compare magenta lines, Figs. 3.1b and 3.3c). However, there are also important differences. First, net energy input seasonality dominates the intensity in the NH whereas in the aquaplanet simulations with small mixed layer depth, net energy input and mean meridional circulation play an equal role (compare magenta and green lines, Fig. 3.1b and 3.3c). Second, while the phase relationship between shortwave absorption and surface heat fluxes is similar, the aquaplanet surface heat fluxes, OLR and atmospheric storage contributions are much larger than those in the NH (compare blue, green and black lines, Fig. 3.1d and 3.3d). Third, while the seasonality of stormtrack intensity in the NH and the small mixed layer depth aquaplanet simulations both involve a contribution from the stationary circulation (mean meridional circulation for the slab-ocean aquaplanet and stationary eddies for the NH), the effects are opposite. In the NH the stationary eddy contribution opposes the seasonality of stormtrack intensity (blue

and red lines, Fig. 3.1b), consistent with stationary eddies generating down-gradient MSE fluxes, and accounts for a mid winter minimum. Whereas for the small mixed layer depth, the mean meridional circulation is approximately in phase with stormtrack intensity (green and red lines, Fig. 3.3c), consistent with the Ferrel cell generating upgradient MSE fluxes, and there is no mid winter minimum (Figs. 3.3c, C1 & C2, Appendix C). Thus, the NH and aquaplanet simulation with small mixed layer depth are in different regimes. Similar differences occur for stormtrack position.

3.4.2 Connecting the aquaplanet and EBM results

As discussed in the Introduction, several stormtrack frameworks are based on mean temperature. Unfortunately those frameworks do not predict temperature and do not include external parameters. Thus, it is difficult to interpret the aquaplanet simulations using mean frameworks. In order to get around this issue we use an EBM because it depends on mixed layer depth and it predicts mean surface temperature (see section 3b). Here we quantify how varying the mixed layer depth in the EBM affects 1) stormtrack seasonality and 2) the mean surface temperature as compared to the aquaplanet. A comparison between the EBM, which has fixed annual-mean diffusivity, and the aquaplanet reveals the role of dynamical feedbacks for stormtrack seasonality. Since the mixed layer depth controls the effective storage [sum of surface fluxes (ocean storage) and atmospheric storage in the aquaplanet] in the EBM we use the EBM intensity decomposition (see equation 3.11) when comparing it to the aquaplanet.

Effect of mixed layer depth on stormtrack and comparison with aquaplanet

The EBM with large mixed layer depth exhibits small seasonality of stormtrack intensity and position consistent with the aquaplanet (compare black and red lines, Fig. 3.10a,b). The small seasonality of stormtrack intensity in the EBM with large mixed layer depth is

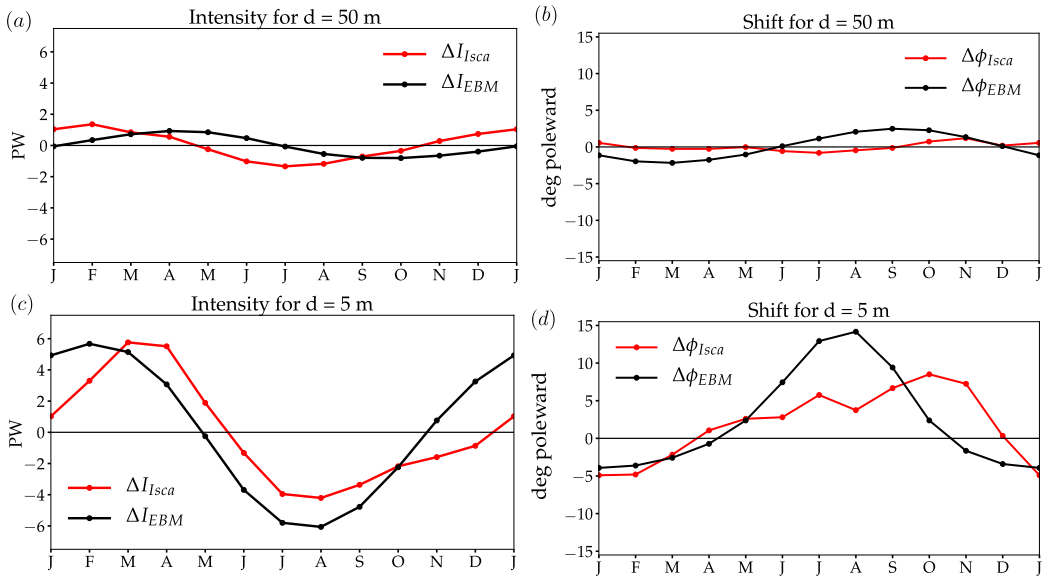

Figure 3.10: stormtrack (a,c) intensity and (b,d) shift as an anomaly relative to the annual mean for the 50 m (top) and 5 m (bottom) mixed layer depth for Isca (red) and EBM (black) simulations.

associated with small net energy input seasonality consistent with the aquaplanet (compare magenta lines, Fig. 3.11a,b). The net energy input seasonality is small because effective storage damps TOA radiation (compare orange and black lines, Fig. 3.11a,b). In the aquaplanet the effective storage is dominated by surface fluxes (compare black and blue lines, Fig. 3.11b), i.e. atmospheric storage is small. Thus the compensation of TOA radiation by effective storage reflects the compensation of TOA radiation by surface fluxes (Fig. 3.2a), which is consistent with the large mixed layer depth hypothesis.

The EBM with small mixed layer depth exhibits large seasonality of stormtrack intensity and position consistent with the aquaplanet (compare black and red lines, Fig. 3.10c,d). The large stormtrack seasonal intensity in the EBM is associated with large net energy input seasonality (Fig. 3.11c,d). The net energy input seasonality is large for small mixed layer depth because the effective storage contribution is phase-shifted by one month relative to the large mixed layer depth (compare orange and black lines, Fig. 3.11a,c). In the

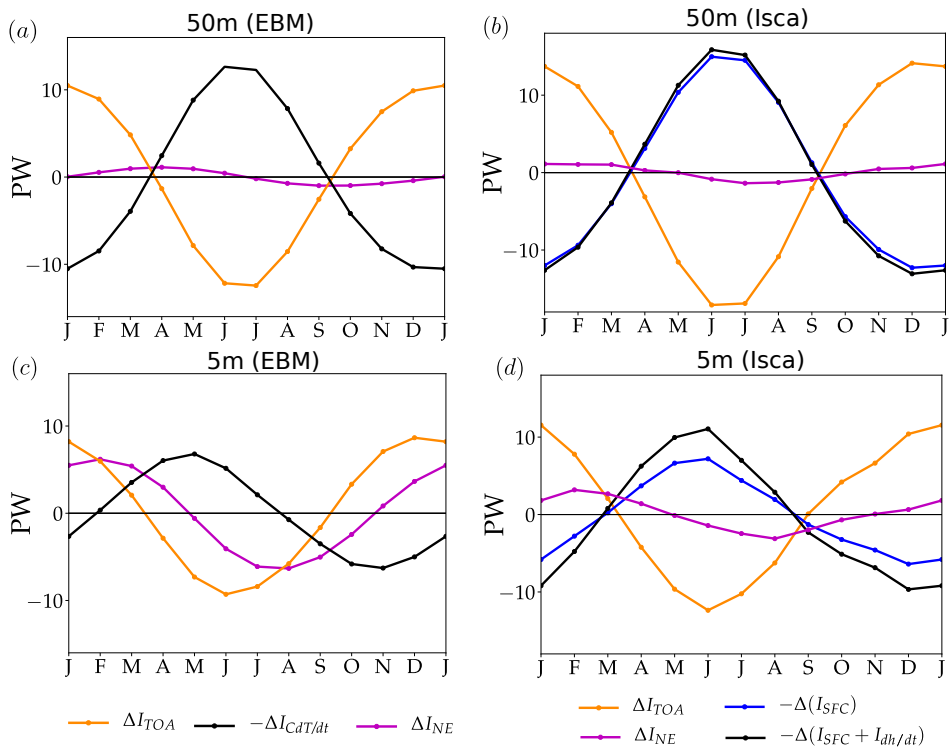

Figure 3.11: Decomposition of stormtrack intensity as an anomaly relative to the annual mean (ΔI) into contributions from net energy input (ΔI_{NE}), TOA radiation (ΔI_{TOA}), effective storage ($-\Delta I_{CdT/dt}$) and surface fluxes (ΔI_{SFC}). Data from (a,c) EBM and (b,d) Isca simulations for 50 m (top) and 5 m (bottom) slab-ocean mixed layer depth.

aquaplanet the changes in seasonality of effective storage from large to small mixed layer depth reflect 1) a larger atmospheric storage contribution (difference between black and blue lines, Fig. 3.11b,d) and 2) a one-month phase-shift of the surface flux contribution (compare blue lines, Fig. 3.11b,d). The surface flux changes in the aquaplanet are due to surface heat flux changes rather than changes in surface shortwave radiation (red dashed line, Fig. 3.2a,c), which is consistent with the small mixed layer depth hypothesis.

While the EBM qualitatively captures the mixed layer depth dependence of stormtrack seasonality in the aquaplanet, it does not capture the quantitative behavior. In particular, the seasonality of stormtrack intensity and position in the aquaplanet are delayed relative to the EBM for small mixed layer depth (compare black and red lines, Fig. 3.10). In order

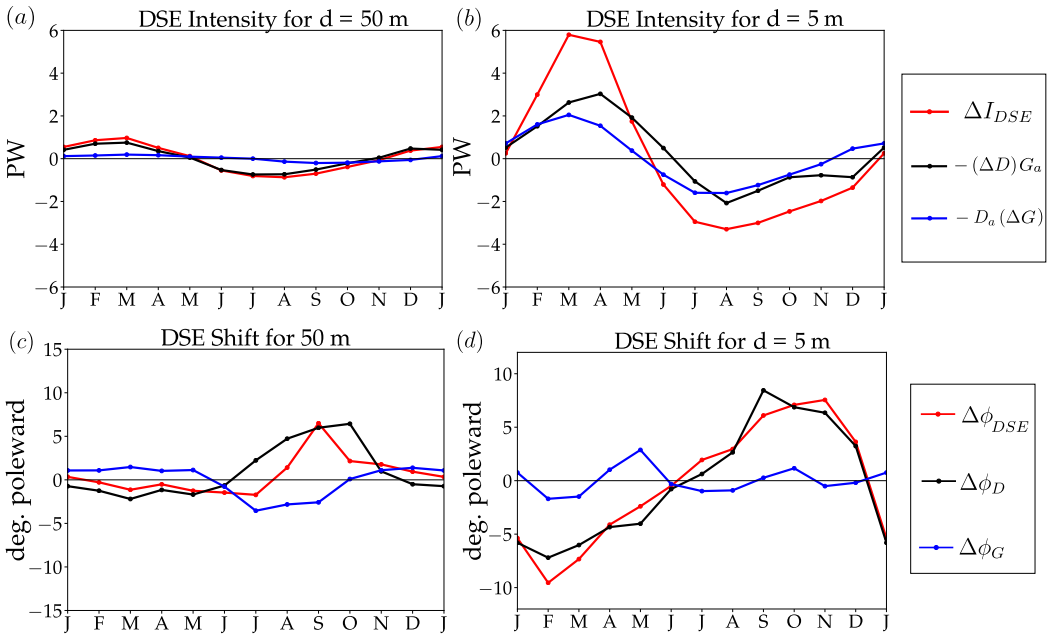

Figure 3.12: Decomposition of stormtrack (a,b) intensity and (c,d) position defined using transient eddy DSE flux (ΔI_{DSE}) as an anomaly relative to the annual mean into contribution from changes in diffusivity ($-(\Delta D)G_a, \Delta\phi_D$) and changes in gradient ($-D_a(\Delta G), \Delta\phi_G$). Data from Isca simulations with 50 m (left) and 5 m (right) slab-ocean mixed layer depth.

to better understand the different stormtrack seasonality in the aquaplanet and EBM we diagnose the aquaplanet diffusivity:

$$D = -\frac{2\pi a\ cos\phi\langle\left[\overline{v's'}\right]\rangle}{\frac{1}{a}\frac{\partial s}{\partial\phi}|_{925hPa}} \tag{3.14}$$

where s is dry static energy (DSE). We focus on DSE because the EBM is dry. We separate stormtrack intensity anomalies relative to the annual mean into gradient and diffusivity contributions:

$$\Delta I_{DSE} \approx -D_a(\Delta G) - (\Delta D)G_a \tag{3.15}$$

where the subscript 'a' refers to the annual mean value and G is the meridional DSE gradient at 925 hPa. According to the EBM the gradient term should dominate [first term on the right

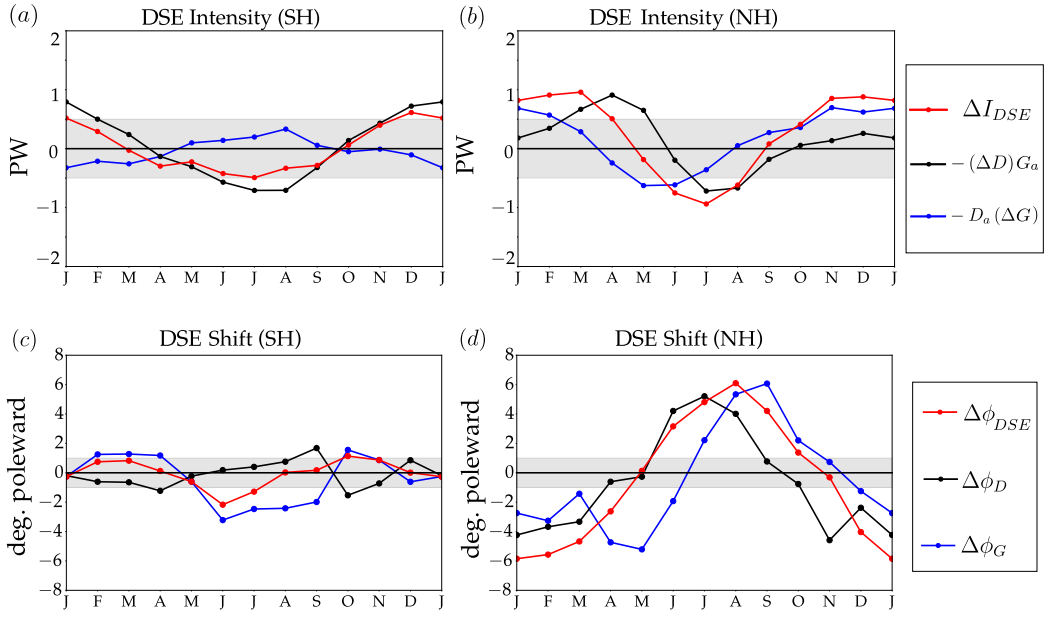

Figure 3.13: Decomposition of stormtrack (a,b) intensity and (c,d) position defined using transient eddy DSE flux as an anomaly relative to the annual mean into contribution from changes in diffusivity $(-(\Delta D)G_a, \Delta\phi_D)$ and changes in gradient $(-D_a(\Delta G), \Delta\phi_G)$. Left panels show SH and right panels show NH for ERA-Interim Reanalysis.

hand side of (3.15)]. The decomposition shows that diffusivity changes dominate stormtrack seasonality in the aquaplanet with large mixed layer depth (red line, Fig. 3.12a) similar to the SH (red line, Fig. 3.13a). Gradient and diffusivity changes are important in the aquaplanet with small mixed layer depth (red and blue lines, Fig. 3.12b) similar to the NH (red line, Fig. 3.13b). They lead to a delay of stormtrack intensity relative to TOA radiation. Recall that the delayed stormtrack intensity in the aquaplanet with small mixed layer depth was associated with the mean meridional circulation contribution (green line, Fig. 3.3c). This suggests that the EBM does not capture the delayed seasonality of stormtrack intensity in the aquaplanet because it does not include dynamical feedbacks.

The seasonal stormtrack shift in the aquaplanet can also be decomposed into gradient and diffusivity contributions. In particular, the seasonal evolution of the transient eddy DSE

flux divergence relative to the annual mean is

$$\Delta F_{TE,DSE} \approx -\underbrace{\partial_y(D_a \Delta G)}_{\Delta F_G} - \underbrace{\partial_y(G_a \Delta D)}_{\Delta F_D} \tag{3.16}$$

such that the stormtrack shift $\Delta\phi$ can be decomposed as

$$\Delta\phi \approx \Delta\phi_G + \Delta\phi_D \tag{3.17}$$

where

$$\Delta\phi_G = \phi_G - \phi_a \quad \text{where} \quad (F_{TE,DSE,a} + \Delta F_G)|_{\phi_G} = 0 \tag{3.18}$$

$$\Delta\phi_D = \phi_D - \phi_a \quad \text{where} \quad (F_{TE,DSE,a} + \Delta F_D)|_{\phi_D} = 0. \tag{3.19}$$

and ϕ_a is the annual mean stormtrack position. Diffusivity changes dominate the seasonal stormtrack shift for large and small mixed layer depths (Fig. 3.12c,d). They also dominate seasonal shifts in the SH and NH (Fig. 3.13c,d). This suggests that the EBM does not capture the delayed seasonality of stormtrack position in the aquaplanet because it does not include dynamical feedbacks.

Effect of mixed layer depth on surface temperature

The EBM mean surface temperature seasonality is small with large mixed layer depth and large with small mixed layer depth consistent with the aquaplanet (Fig. 3.14). This suggests that one could interpret the mixed layer depth control on stormtrack seasonality via surface baroclinity. However, the EBM does not quantitatively capture the mean surface temperature seasonality in the aquaplanet. In particular, the temperature in the aquaplanet is delayed relative to the EBM in the limit of small mixed layer depth (Fig. 3.14c,d). The mean surface temperature delay in the aquaplanet is also consistent with delayed stormtrack

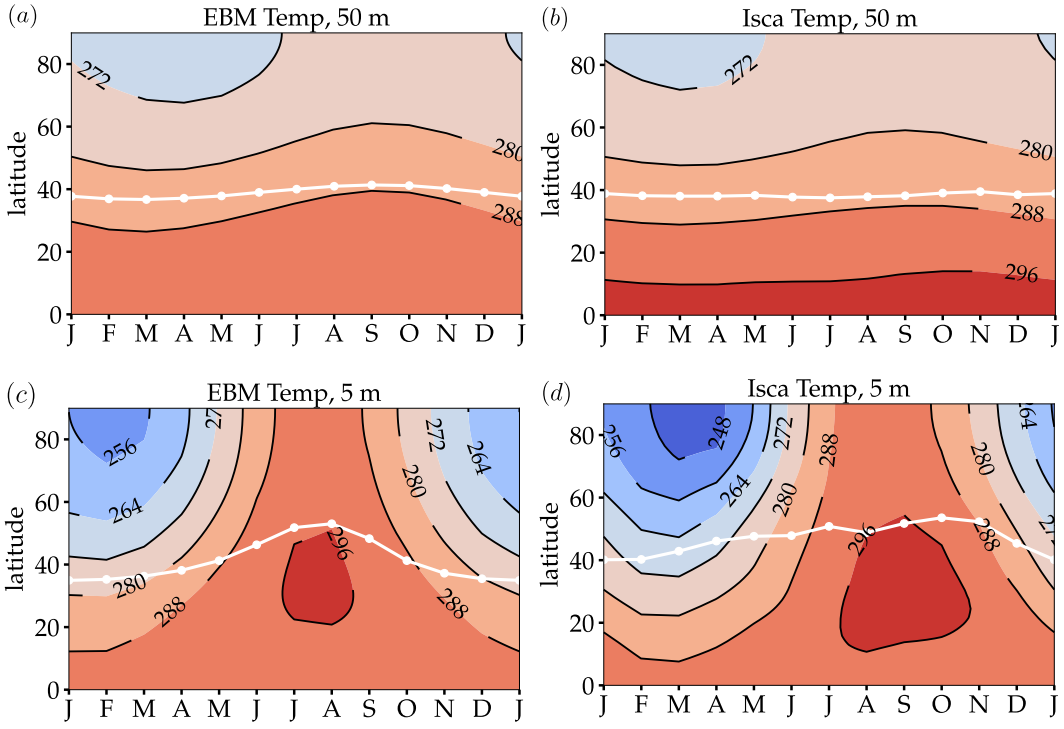

Figure 3.14: Seasonal evolution of mean surface temperature for (a,c) EBM and (b,d) Isca simulations with 50 m and 5 m mixed layer depth. White lines show the stormtrack position.

seasonality. Since the thermodynamic component of the mean meridional circulation contribution to stormtrack intensity is small (Fig. 3.6c) the results suggest that the stormtrack feeds back on the mean surface temperature in the aquaplanet, which is not accounted for in the EBM. Thus, the stormtrack and mean surface temperature are responding to changes in mixed layer depth in the aquaplanet and also influencing each other.

3.5 Conclusions and discussion

3.5.1 Conclusions

Previous work has shown that the observed hemispheric differences in stormtrack seasonality cannot be explained by insolation alone (B17 and S18). Diagnostic analysis using the MSE

framework for zonal-mean stormtracks suggested an important role for differences in surface heat flux (S18). Here we consider the causal role of surface fluxes in determining the intensity and position of the zonal-mean stormtracks. We focus on surface fluxes because 1) they can be controlled by an external parameter (the mixed layer depth) and 2) they affect the seasonality of surface heat fluxes. Assuming the stationary circulation and atmospheric storage do not contribute to stormtrack seasonality, we hypothesize that surface fluxes modulate stormtracks via two different limits of mixed layer depth:

1. For large mixed layer depth, surface flux is large enough to compensate TOA insolation, net energy input seasonality is small, surface heat fluxes are out of phase with shortwave absorption and stormtrack seasonality is small.

2. For small mixed layer depth, surface flux is small, net energy input seasonality is large, surface heat fluxes are in phase with shortwave absorption and stormtrack seasonality is large.

Using a scaling analysis of the MSE budget, we estimate a critical mixed layer depth ~10 m separates these two limits (see equation 3.8). The hypotheses are tested by varying the mixed layer depth in zonally-symmetric slab-ocean aquaplanet simulations with zero ocean energy transport. We also examine the impact of varying the mixed layer depth on stormtrack and mean surface temperature seasonality in an EBM.

The slab-ocean aquaplanet simulations confirm the large mixed layer depth hypothesis. Namely, for large mixed layer depth the seasonality of net energy input is small, surface heat fluxes are out of phase with shortwave absorption and stormtrack seasonality is small. The stationary circulation and atmospheric storage contributions are also small. The simulations also confirm some aspects of the small mixed layer depth hypothesis. Namely, for small mixed layer depth the seasonality of net energy input is large, surface heat flux is in phase with shortwave absorption and stormtrack seasonality is large. However, the hypothesis fails

to capture the large contributions from dynamical changes in the Ferrel cell and atmospheric storage.

The slab-ocean aquaplanet simulation with large mixed layer depth captures many aspects of the zonal-mean stormtrack in the SH, i.e. small seasonality of net energy input, surface heat fluxes that are out of phase with shortwave absorption, small seasonality of stormtrack intensity and position and mean surface temperature. Our results are consistent with Donohoe *et al.* (2014) who showed that a 50 m mixed layer depth aquaplanet simulation reproduces the seasonality of SH atmospheric temperature. The addition of an idealized polar ice cap that mimics Antarctica better captures the seasonality of the surface heat flux and OLR contributions to stormtrack intensity.

The slab-ocean aquaplanet simulation with small mixed layer depth captures some aspects of the zonal-mean stormtrack in the NH, i.e. large seasonality of net energy input, surface heat fluxes that are in phase with shortwave absorption and large seasonality of stormtrack intensity, position and mean surface temperature. However, the detailed evolution is different from the zonal-mean stormtrack in the NH. In particular, atmospheric storage is much larger in the aquaplanet consistent with the seasonal amplitude of atmospheric temperature increasing with decreasing mixed layer depth (Donohoe *et al.*, 2014). Furthermore, the NH stationary eddies oppose stormtrack seasonality, consistent with stationary eddies generating down-gradient MSE fluxes. Whereas in the aquaplanet with small mixed layer depth, the mean meridional circulation contribution is in phase with stormtrack intensity consistent with the Ferrel cell generating up gradient MSE fluxes. We show that the mean meridional circulation contribution in the small mixed layer depth simulation arises from dynamical (eddy momentum flux divergence) changes in the Ferrel cell and not from interactions with the Hadley cell.

We focused on the MSE framework for stormtracks because external parameters such as insolation and mixed layer depth do not appear in mean thermodynamic frameworks. Instead

we showed that an EBM can be used to understand the impact of mixed layer depth on the seasonality of the stormtrack and mean surface temperature in the aquaplanet qualitatively. More specifically, the EBM captures the large stormtrack and mean surface temperature seasonality for small mixed layer depth and small stormtrack and mean temperature seasonality for large mixed layer depth. However, a detailed comparison with the aquaplanet revealed that the EBM could not quantitatively capture the seasonality in the aquaplanet because it assumes constant annual-mean diffusivity. The diffusivity changes in the aquaplanet are likely related to the interactions between the stormtrack and mean meridional circulation.

3.5.2 Discussion

Previous work using reanalysis data suggested the hemispheric difference in zonal-mean stormtrack seasonality is connected to hemispheric differences in mean surface temperature seasonality (O'Gorman, 2010). However, mean surface temperature is not an external parameter. Our EBM suggests the underlying reason for the different mean surface temperature seasonality is most likely hemispheric differences in surface heat capacity (mixed layer depth). Furthermore, since the aquaplanet and EBM results show the feedback of the stormtrack on mean surface temperature is large, one must be cautious when interpreting results using mean surface temperature from reanalysis.

A zonally-symmetric aquaplanet with a uniformly small mixed layer depth is clearly not a good idealization of the NH stormtrack. Donohoe & Battisti (2013) showed that in the NH extratropics, the zonal energy transport by the mean westerly winds damps the seasonal heating over land and amplifies it over ocean. Therefore, a zonal combination of small and large mixed layer depth may better reproduce the NH stormtrack. It may also better capture the role of stationary eddies, which generate down-gradient MSE fluxes and are important for stormtrack seasonality in the NH. Quantifying the impact of a zonally-dependent mixed layer depth is work in progress.

We show that dynamical changes in the Ferrel cell affect the seasonality of stormtracks in the small mixed layer depth limit. Currently, it is not clear how the Ferrel cell contribution scales with mixed layer depth and whether the small mixed layer depth limit is relevant to past zonally-symmetric climates such as Snowball Earth. A better understanding of the Ferrel cell contribution requires a connection between the MSE and momentum budgets. Recent work by Lachmy & Shaw (2018) has made progress in this direction but more work is needed. Alternatively, one could transform to potential temperature coordinates to remove the Ferrel cell but this complicates the surface boundary condition (Held & Schneider, 1999).

A limitation of the slab-ocean aquaplanet simulations used in this study is that the mixed layer depth is prescribed and there is no ocean energy transport. The addition of annual-mean ocean energy transport does not change the conclusions (not shown). However, recent observations show that the mixed layer depth in the SH varies seasonally between 30 m and 160 m (see 3.6.4, Fig. 3.30, Holte *et al.*, 2017), which is greater than the critical depth (10 m). Thus we do not expect the seasonal variations will affect our conclusions. Nevertheless, the impact of mixed layer depth seasonality will be quantified in future work.

Overall, our results show that surface fluxes modulate the seasonal evolution of zonal-mean stormtracks and provide an explanation for the small stormtrack seasonality in the SH. An assessment of the importance of surface fluxes for the stormtrack response to forcings on other timescales (increased CO_2, Last Glacial Maximum and Snowball Earth) is work in progress.

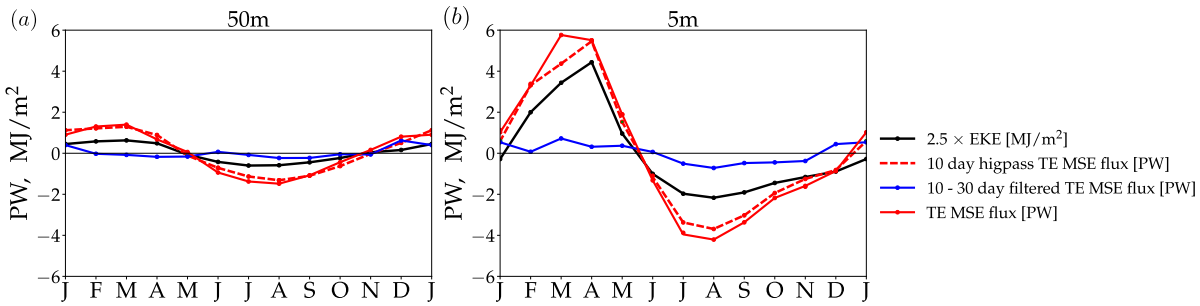

Figure 3.15: Seasonal stormtrack intensity as an anomaly relative to the annual mean defined using vertically integrated transient eddy MSE flux calculated using a monthly average (solid red), 10-day high-pass-filter MSE flux (dashed red), 10-30 day filter MSE flux (blue) and eddy kinetic energy (black). Data from Isca simulations with (a) 50 m and (b) 5 m slab-ocean mixed layer depth.

3.6 Appendices

3.6.1 Appendix A: Comparison of stormtrack metrics

In the MSE framework, stormtracks are defined using a monthly average. Defining the stormtrack using a monthly average is qualitatively similar to defining them using a 10-day high pass filter (compare solid and dashed red lines in Figs. 3.15 & 3.16). More specifically, the quasi-stationary (10-30 day filtered) transient eddy contribution is very small (blue lines, Figs. 3.15 & 3.16).

3.6.2 Appendix B: GFDL AM2

We performed zonally-symmetric slab-ocean aquaplanet simulations using GFDL AM2 to corroborate our results from the Isca model (Figs. 3.17 - 3.27). GFDL-AM2 and Isca mostly differ in their convection schemes and the inclusion of cloud radiative effects. The model results are robust for Isca and GFDL, thus the main conclusions are not dependent on convection scheme or the inclusion of cloud radiative effects.

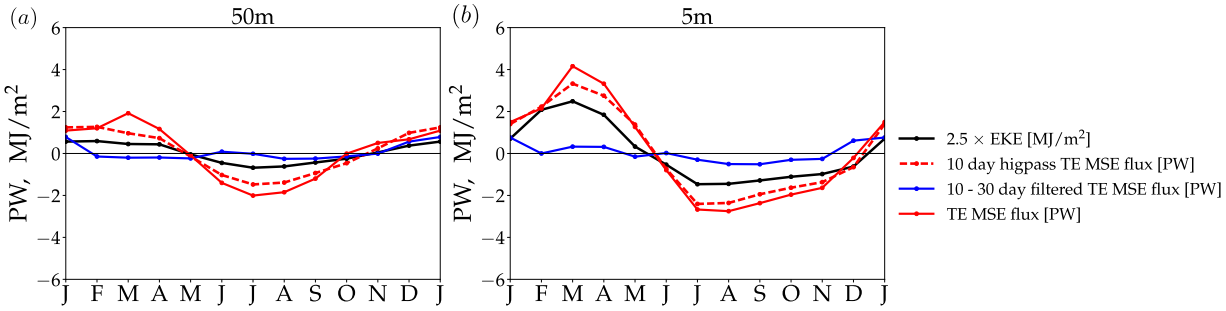

Figure 3.16: As in Fig. 3.15 but for GFDL simulations.

3.6.3 Appendix C: Mid-winter minimum

We found no mid-winter minimum in our zonally-symmetric slab-ocean aquaplanet simulations for large and small mixed layer depths for both Isca (Fig. C1) and GFDL (Fig. C2) simulations. In contrast, the zonal-mean stormtrack exhibits a very clear mid-winter minimum in the NH (Fig. 3.1b). In particular, the stormtrack is weak when net energy input suggests it should be large (compare red and magenta lines Fig. 3.1b) because of the compensating behavior of stationary eddies (blue line, Fig. 3.1b).

Recent studies reported midwinter minimums in zonally symmetric GCMs. For example, Yuval & Kaspi (2018) reported a midwinter minimum when prescribing the vertical temperature structure of the North Pacific sector in a zonally-symmetric dry dynamical core. Once again it is difficult to interpret those results because the seasonal mean temperature stormtrack relationship is not causal. Novak *et al.* (2019) reported a midwinter minimum in slab-ocean aquaplanet simulations with gray radiation with varied ocean energy transport. While their aquaplanet set up is similar to the one used here, we could not reproduce their results with RRTMG or gray radiation.

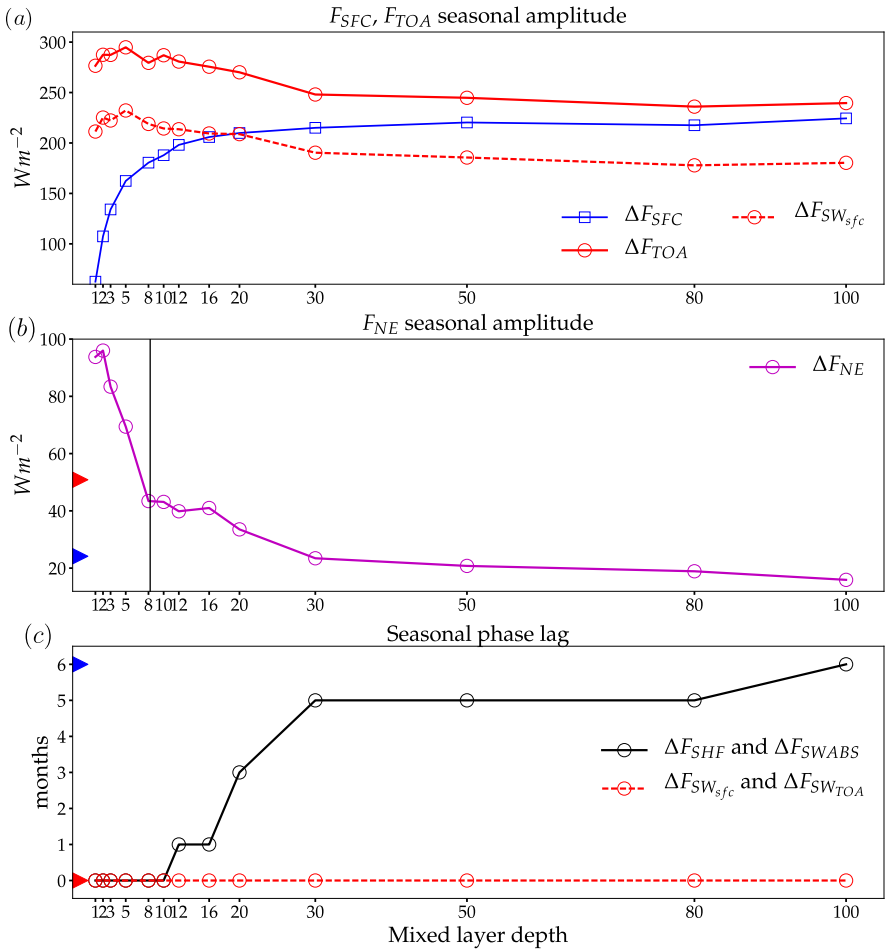

Figure 3.17: As in Fig. 3.2 but for GFDL simulations.

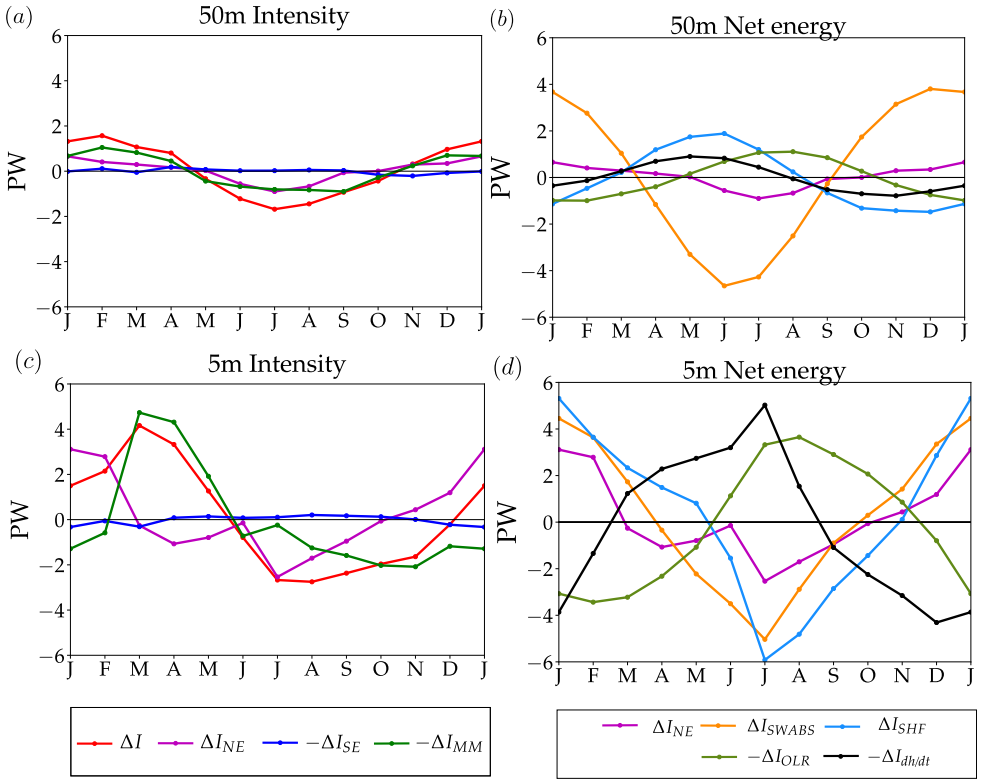

Figure 3.18: As in Fig. 3.3 but for GFDL simulations.

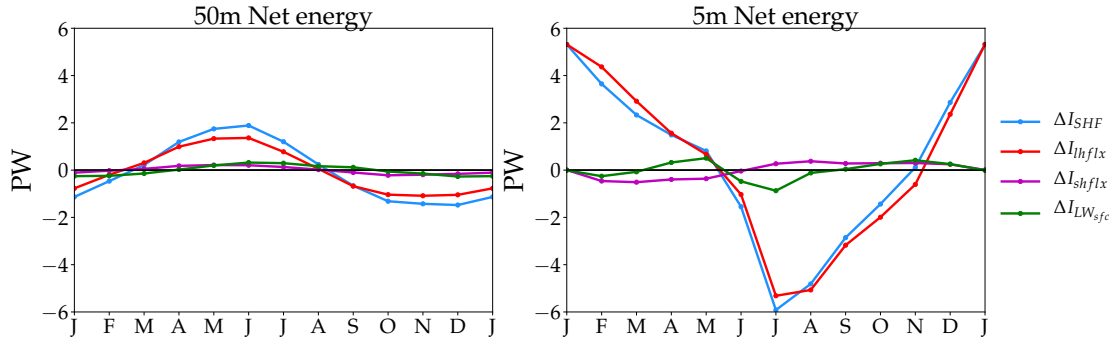

Figure 3.19: As in Fig. 3.4 but for GFDL simulations.

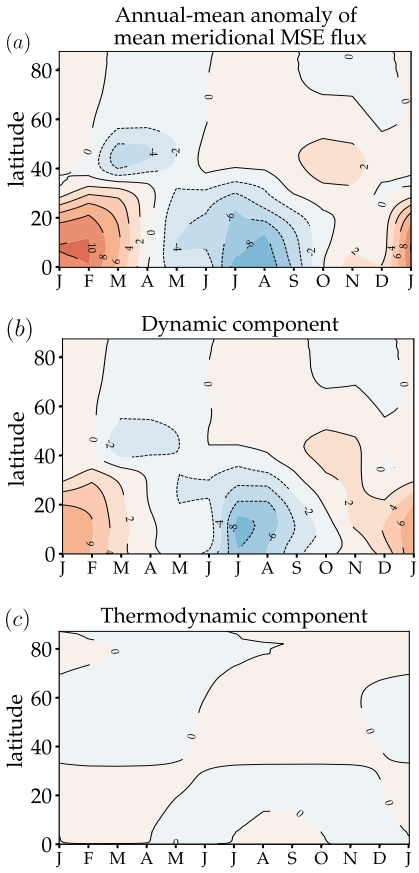

Figure 3.20: As in Fig. 3.6 but for GFDL simulations.

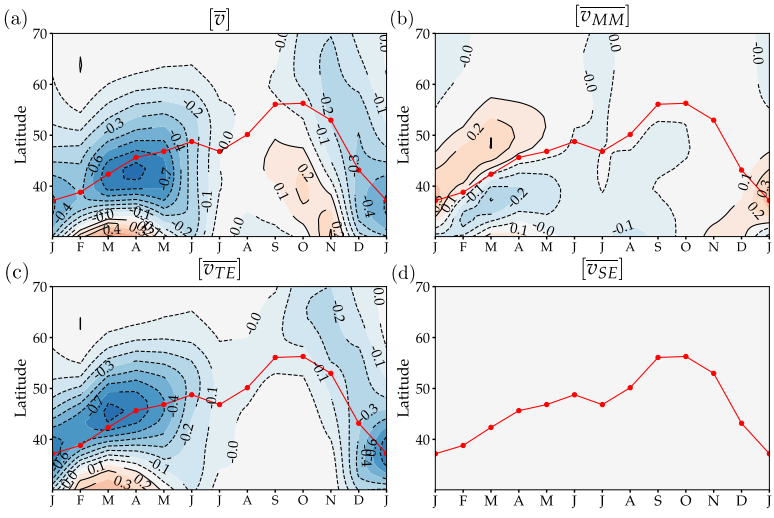

Figure 3.21: As in Fig. 3.7 but for GFDL simulations.

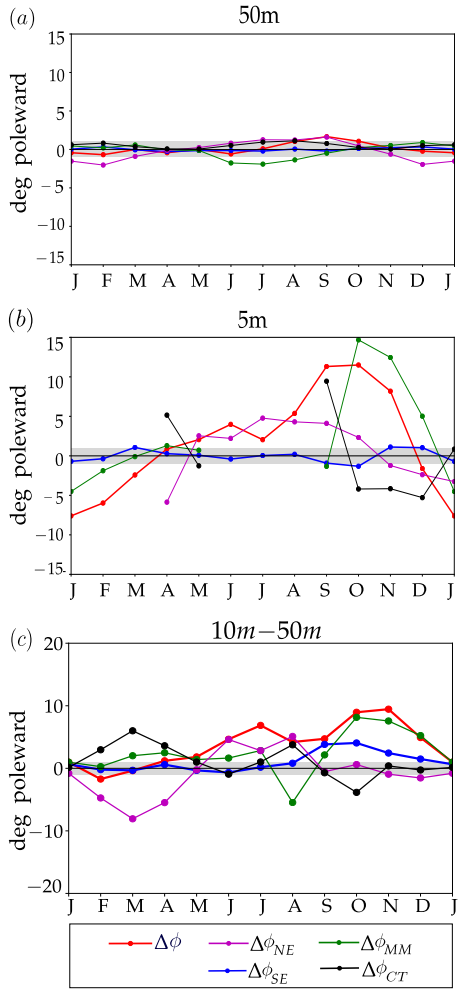

Figure 3.22: As in Fig. 3.8 but for GFDL simulations.

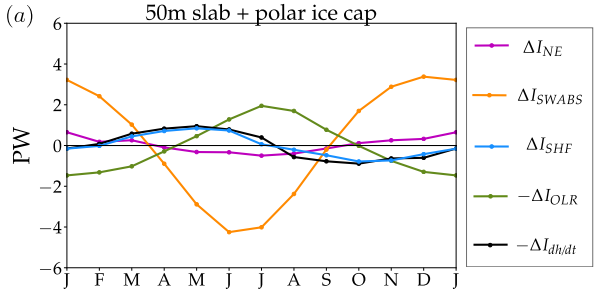

Figure 3.23: As in Fig. 3.9 but for GFDL simulations.

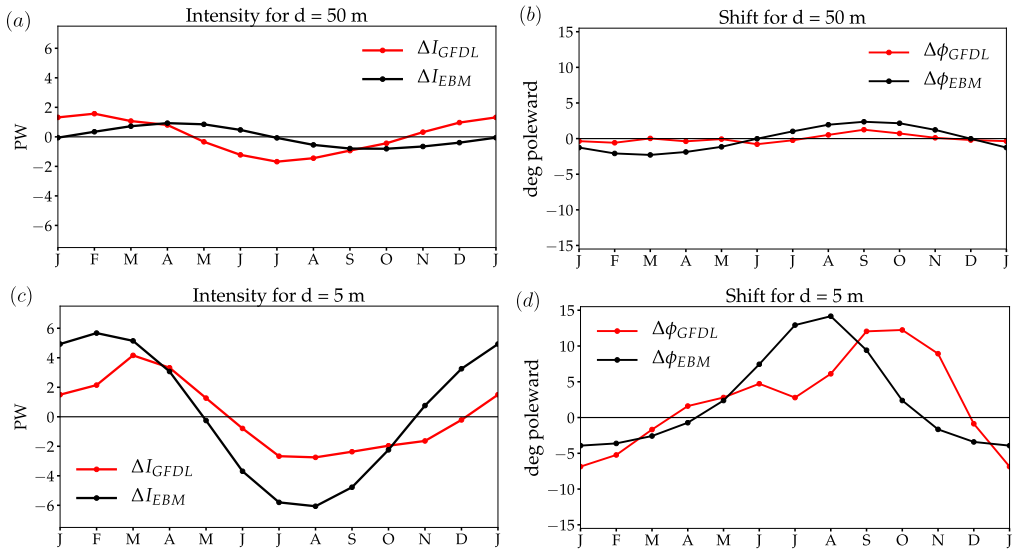

Figure 3.24: As in Fig. 3.10 but for GFDL simulations.

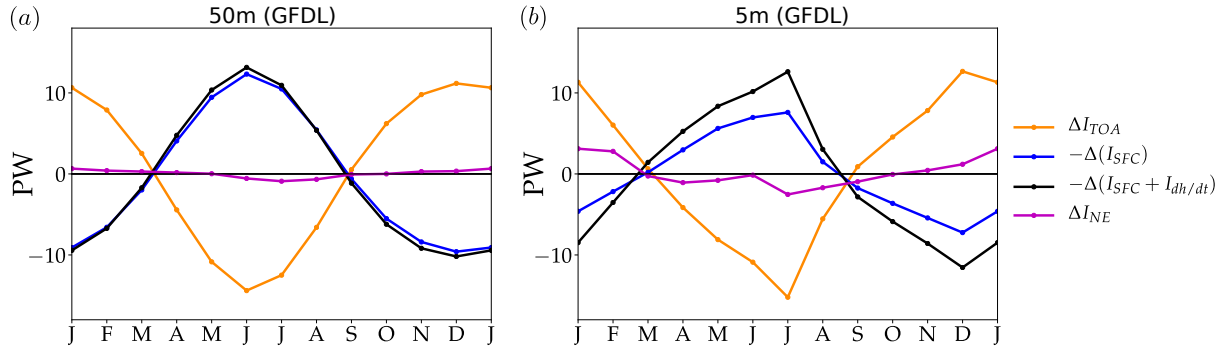

Figure 3.25: As in Fig. 3.11b,d but for GFDL simulations.

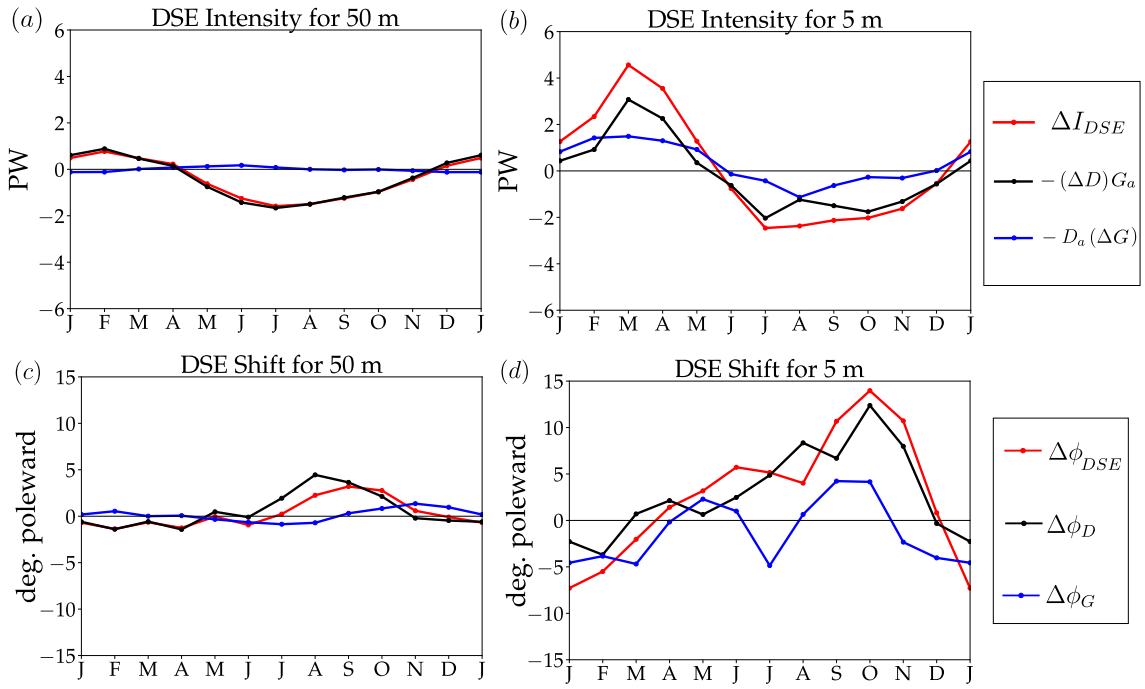

Figure 3.26: As in Fig. 3.12 but for GFDL simulations.

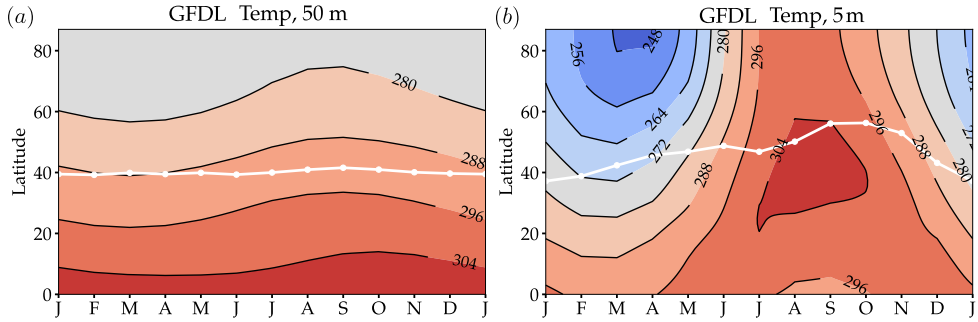

Figure 3.27: As in Fig. 3.13b,d but for GFDL simulations.

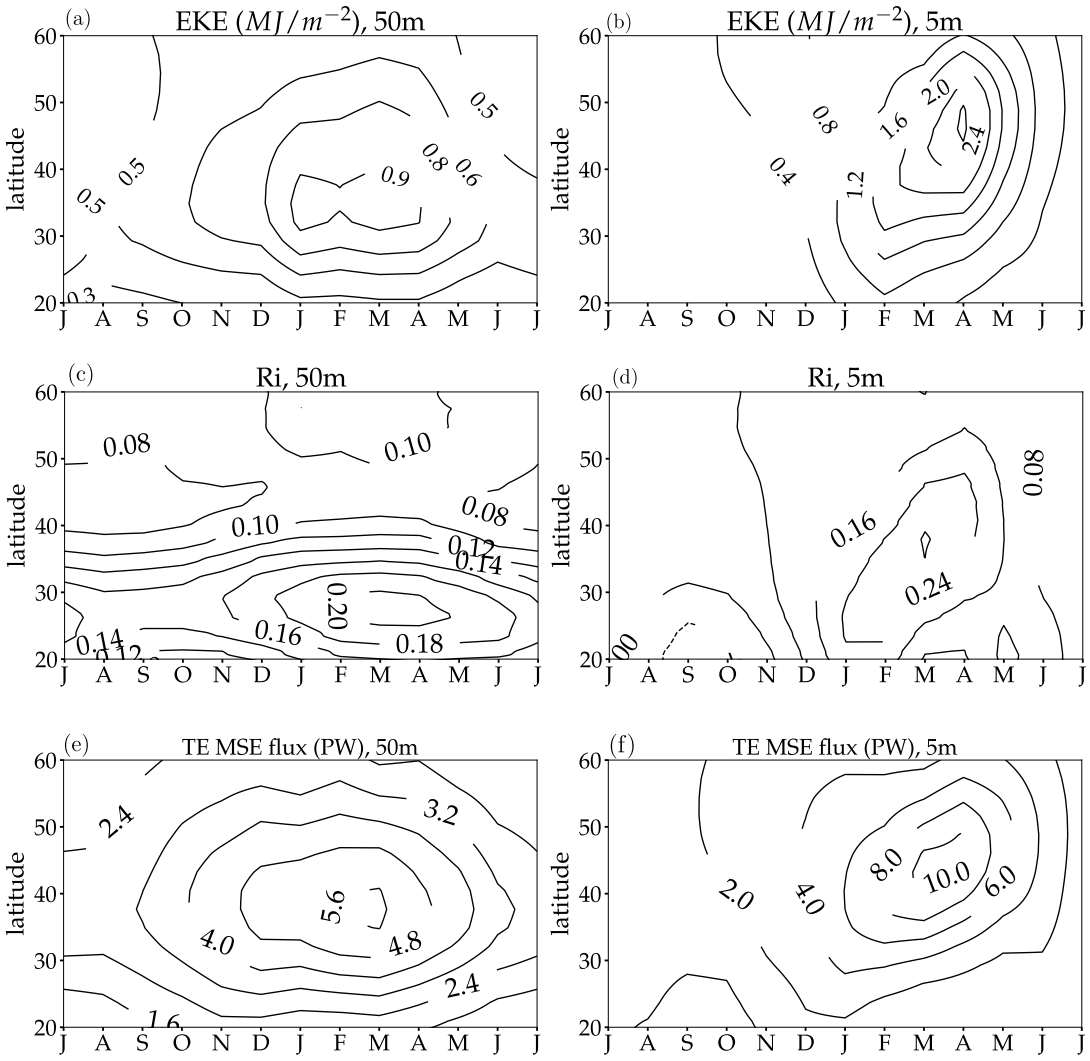

Figure 3.28: Seasonal evolution of (a,b) vertically integrated 10-day high pass filtered eddy kinetic energy (EKE), (c,d) Richardson number as defined in Nakamura (1992), and (e,f) vertically integrated transient eddy MSE flux. Data from Isca simulations for 50 m (left) and 5 m (right) slab-ocean mixed layer depth.

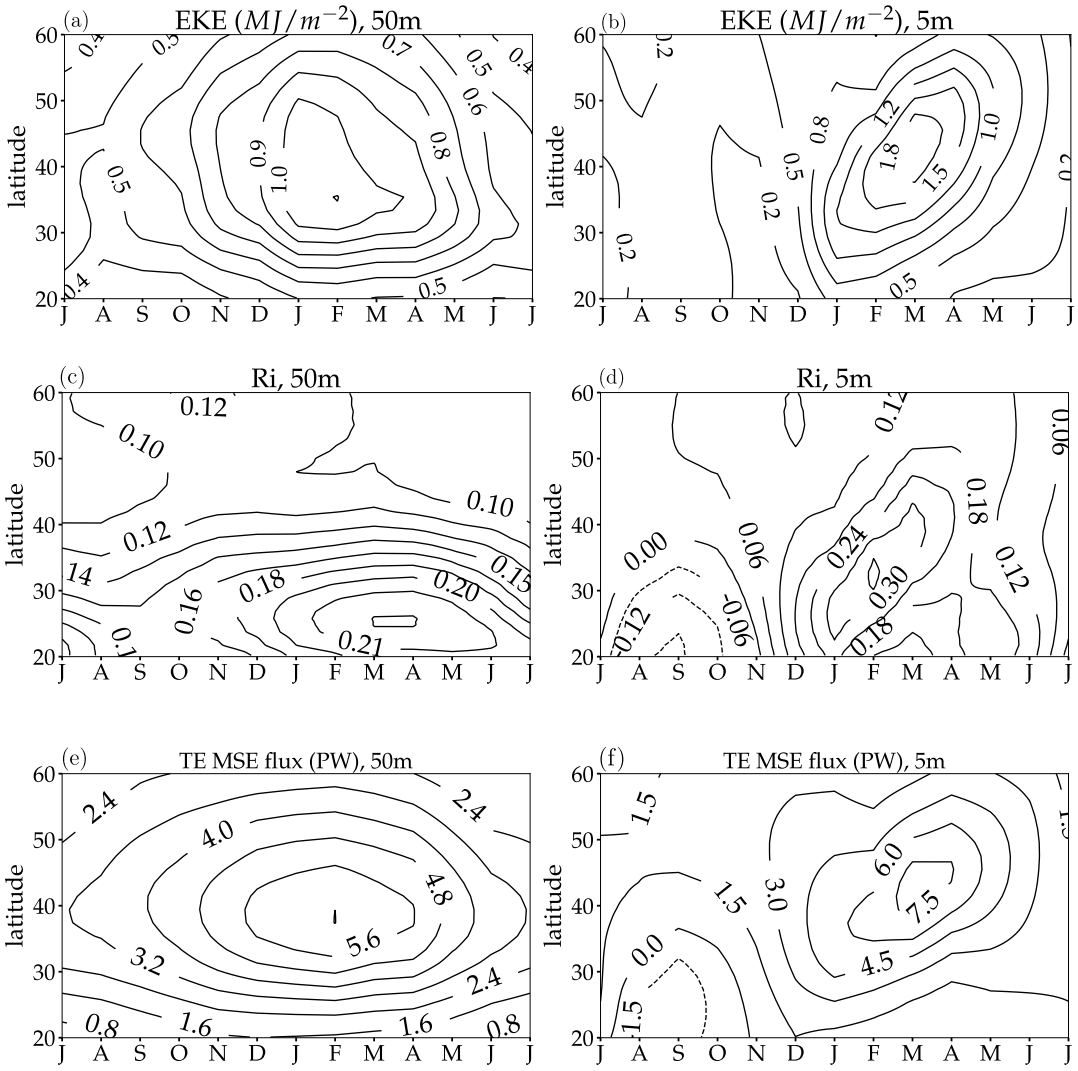

Figure 3.29: As in Fig. 3.28 but for GFDL simulations with 50 m (left) and 5m (right) slab-ocean mixed layer depth.

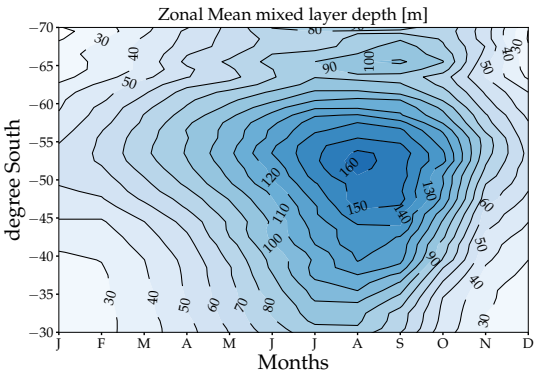

Figure 3.30: Seasonal evolution of zonal-mean and monthly mean mixed layer depth in the Southern Hemisphere based on density profiles. Data is obtained from a database of mixed layer properties computed from nearly 1,250,000 delayed-mode and real-time Argo profiles collected from 2000 to present (Holte *et al.*, 2017).

3.6.4 Appendix D: Seasonal evolution of SH mixed layer depth

The SH mixed layer depth based on density profiles from Holte *et al.* (2017) varies between between 30 m to 160 m in the extratropics (Fig. 3.30). This suggests that the mixed layer depth in the SH exceeds the critical depth of ~10m (see equation 3.8) throughout the seasonal cycle.

CHAPTER 4

INVESTIGATING PERSISTENT ANOMALIES IN THE WINTERTIME JET STREAM USING THE WAVE ACTIVITY BUDGET

4.1 Introduction

Atmospheric blocking represents a disruption of eastward migrating synoptic eddies and occurs due to persistent meandering of the jet stream that can last for a week or longer (Rex, 1950; Berggren *et al.*, 1949; Woollings *et al.*, 2010, 2018). Atmospheric blocks often form nearly stationary anticyclones (cyclones) that cause unusually high or cold temperatures in the midlatitudes resulting in significant societal impacts (Demirtaş, 2017).

Some of the proposed theories for formation and maintenance of atmospheric blocks include resonance between stationary Rossby waves and boundary forcing (Charney & DeVore, 1979; Tung & Lindzen, 1979), interaction between stationary waves and transient eddies (Berggren *et al.*, 1949; Green, 1977; Shutts, 1983; Luo *et al.*, 2019), instability/nonlinearity of low frequency waves (Swanson, 2000; Cash & Lee, 2000) and modon in a shear flow (McWilliams, 1980; Butchart *et al.*, 1988). Observational studies have also shown the important role for wave-mean flow interaction (Colucci, 1985; Mullen, 1987; Nakamura *et al.*, 1997; Colucci, 2001; Woollings *et al.*, 2008; Pelly & Hoskins, 2003a; Woollings *et al.*, 2008; Altenhoff *et al.*, 2008) and diabatic heating associated with moist processes (Pfahl *et al.*, 2015). However, what conditions precisely lead to blocking onset is not well understood. Lack of a definitive theory for blocking onset and disagreement among blocking indices (Barnes *et al.*, 2012, 2014) has posed a major challenge for the numerical weather prediction of the midlatitudes (Pelly & Hoskins, 2003b).

Recently, Nakamura & Huang (2018, hereafter NH18) proposed a semi-empirical theory for atmospheric blocking based on the conservation of finite-amplitude local wave activity

(LWA). LWA is the amplitude of a Rossby wave measured by the meridional displacement of quasigeostrophic potential vorticity from zonal symmetry and quantifies the wave's ability to modify angular momentum. (Huang & Nakamura, 2016; Nakamura & Huang, 2017, NH18). The 1D model proposed by NH18 suggests that atmospheric blocks are similar to a 'traffic-jam'. Similar to the traffic capacity of a highway, the jet stream has a maximum capacity for zonal LWA flux. Transient forcings like synoptic cyclones and diabatic heating may force the LWA to exceed a threshold flux and stall the cyclone traffic. At the threshold, an increasing LWA decelerates the westerly winds to the point that the zonal LWA flux stops growing, and blocking manifests as congestion of large-amplitude Rossby waves. NH18 draw this conclusion based on 38-year (1979-2016) average of column LWA budget for the exit regions of the storm tracks in the Northern Hemisphere (NH) winter. Subsequently, Paradise *et al.* (2019) use the conceptual traffic-jam model in hypothetical climate states and show that the blocking statistics are sensitive to the stationary wave amplitude, jet speed and transient forcings.

While the traffic-jam idea represents one of the possible mechanisms for block formation, properties of blocking vary widely from episode to episode: location, season, and persistence all add distinctive flavors to blocking events. Any given blocking event can deviate significantly from the canonical traffic jam description, depending on how the LWA budget materializes. The upstream seeding of LWA can vary significantly from event to event, and terms other than the convergence of the zonal flux of LWA (i.e. meridional convergence, baroclinic generation, diabatic sources) can contribute significantly to the growth of LWA in some events. Yet the LWA budget approach of Huang & Nakamura (2016, 2017) and NH18 provides a unifying theoretical framework for understanding the diverse properties of block formation.

In this chapter, we perform a thorough analysis of major persistent anomalies in the jet streams during the NH winter (ERA-I 1979-2018) and characterize the LWA budget during

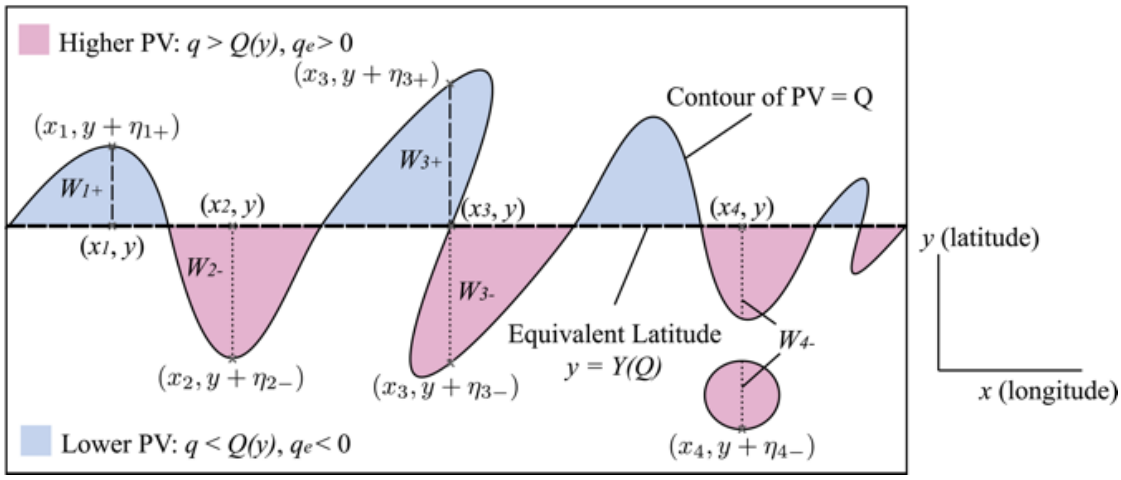

Figure 4.1: A schematic diagram illustrating how to compute the local finite-amplitude wave activity in Eq. (4.1). The wavy curve indicates a contour of PV, above which the PV values are greater than below. Inside the red lobes $q_e \geq 0$, and inside the blue lobes $q_e \leq 0$. Four points (x1, x2, x3, x4) with their meridional displacements (η_{1+}, η_{2-}, η_{3-}, η_{3+} and η_{4-}) are shown to illustrate how the domain of integral is chosen (adapted from Huang & Nakamura, 2016)

these events. We show that key ingredients of the traffic jam theory, such as the negative correlation between the zonal wind and LWA and an upper bound for the zonal LWA flux are widely recognized in the midlatitudes but the relative roles of LWA budget terms vary significantly depending on the locations, persistence of the events, and the growth and decay stages of the anomalous events. We restrict our attention to the boreal winter in this study. Comparisons with summer blocks and the Southern Hemisphere will be deferred to a future study.

4.2 Theory and methods

4.2.1 The Finite-Amplitude Local Wave Activity (LWA)

We use the finite-amplitude local wave activity (LWA) formalism to quantify the waviness of the jet stream. LWA is based on the conservation of quasigeostrophic potential vorticity (PV) (Nakamura & Zhu, 2010; Huang & Nakamura, 2016) and quantifies the amplitude of

Rossby wave as the meridional displacement of PV contour (q) from a hypothetical, zonally symmetric wave-free reference state (Q) (Huang & Nakamura, 2016):

$$\begin{aligned} A(x,y,z,t) = &\int_{W_-} q_e\left(x, y+y', z, t\right) dy' \\ &- \int_{W_+} q_e\left(x, y+y', z, t\right) dy' \\ W_+ :&0 \le y' \le \eta_+\left(x,y,z,t\right),\ q \le Q(y,z); \\ W_- :&0 \ge y' \ge \eta_-\left(x,y,z,t\right),\ q \ge Q(y,z); \end{aligned} \tag{4.1}$$

where x, y, z are longitude, latitude and pseudoheight respectively in cartesian coordinates, t is time, $q_e = q - Q$ is the eddy potential vorticity and η_+, η_- are meridional displacements of PV contours in the poleward and equatorward directions. See Fig. 4.1 for schematic. Here Q is the zonally symmetric, Lagrangian-mean reference state defined at equivalent latitude y (or ϕ in spherical coordinates). See Huang & Nakamura (2016) for the definition of reference state and equivalent latitude.

4.2.2 The LWA budget

The time evolution of column averaged LWA at a given latitude (ϕ) and longitude (λ) is governed by the LWA budget (Huang & Nakamura, 2017). Upon vertical averaging, the column budget is expressed as

$$\begin{aligned} \frac{\partial}{\partial t}\langle A\rangle cos\phi = \quad & \underbrace{-\frac{1}{acos\phi}\frac{\partial\langle F_\lambda\rangle}{\partial\lambda}}_{\text{zonal LWA flux convergence}} \quad \underbrace{+\frac{1}{acos\phi}\frac{\partial}{\partial\phi'}\langle u_e v_e cos^2(\phi+\phi')\rangle}_{\text{divergence of meridional eddy momentum flux}} \\ & \underbrace{+\frac{fcos\phi}{H}\left(\frac{v_e\theta_e}{\partial\widetilde{\theta}/\partial z}\right)_{z=0}}_{\text{meridional eddy heat flux near surface}} \quad \underbrace{+\langle\dot{A}\rangle cos\phi}_{\text{diabatic sources and sinks of LWA}} \end{aligned} \tag{4.2}$$

where $\langle(\dot{)}\rangle$ denotes density-weighted vertical averaging, (u, v, θ) denote the zonal, meridional wind velocities and potential temperature. The subscript e denotes the departure from the reference state (eddy). $\tilde{\theta}$ denotes the area-weighted average of potential temperature over the NH and a is radius of the Earth. The column averaged zonal LWA flux, $\langle F_\lambda \rangle$ can be further decomposed as

$$\langle F_\lambda \rangle = \underbrace{\langle u_{REF} A \cos\phi \rangle}_{F_1} \underbrace{- a\langle \int_0^{\Delta\phi} u_e q_e cos\left(\phi + \phi'\right) d\phi' \rangle}_{F_2} + \underbrace{\frac{cos\phi}{2} \left\langle v_e^2 - u_e^2 - \frac{R}{H} \frac{e^{-\kappa z/H}}{\partial\widetilde{\theta}/\partial z} \theta_e^2 \right\rangle}_{F_3} \quad (4.3)$$

where u_{REF} is the zonal wind speed of the wave-free reference state, $F_1 + F_3$ are LWA fluxes associated with the group propagation of the Rossby waves and F_2 represents nonlinear modification of the advective flux by large-amplitude waves (NH18).

4.2.3 Traffic-jam theory

NH18 applied Eqs. (4.2) & (4.3) to ERA-Interim reanalysis particularly in the exit region of North Atlantic (NA) and North Pacific (NP) storm track during boreal winter [December-January-February (DJF)] between 1979-2016. They identified three key empirical relations that form the basis of the traffic-jam model for atmospheric blocking.

The first is an anticorrelation between LWA and the local zonal wind. On synoptic time-scale the growth of wave amplitude occurs at the expense of local zonal wind and vice-versa. (Huang & Nakamura, 2017; Nakamura & Huang, 2017). This is expressed approximately as

$$\langle u \rangle \approx \langle u_{REF} \rangle - \alpha \langle A \rangle \quad (4.4)$$

where $\alpha \approx 0.3$ denotes the nonlinear interaction strength between LWA and the zonal wind (Figs. 2B,C in NH18). This is related to the fact that LWA quantifies an ability to modify the angular momentum of the flow (non-acceleration relation). The value of α is typically

smaller than 1 and depends on the baroclinicity of the flow and non-conservative processes. Second, on synoptic timescale $\frac{\partial \langle A \rangle}{\partial t}$ is dominated by zonal LWA flux convergence (NH18), i.e.

$$\frac{\partial}{\partial t} \langle A \rangle \cos\phi \approx -\frac{1}{a \cos\phi} \frac{\partial}{\partial \lambda} \langle F_\lambda \rangle , \tag{4.5}$$

suggesting that the storm track acts primarily as a waveguide.

Finally, using Eq. (4.5) and assuming $F_2 \approx (\langle u \rangle - \langle u_{REF} \rangle) \langle A \rangle \cos\phi$, NH18 identify nonlinear relationship in the reanalysis dataset between LWA and its zonal flux. Although the relationship is obscured by scatter, on average the zonal LWA flux exhibits a unimodal distribution with respect to LWA, which NH18 simplify as

$$\langle F_\lambda \rangle \approx \underbrace{\left(\langle u_{REF} \rangle + c_g \right) \langle A \rangle \cos\phi}_{F_1 + F_3} \underbrace{- \alpha \langle A \rangle^2 \cos\phi}_{F_2} \tag{4.6}$$

where c_g is the constant zonal group velocity in the reference state (Fig. 4 in NH18). The above relation suggests that $\langle F_\lambda \rangle$ maximizes at an intermediate value of wave activity defined by $\langle A_c \rangle = \frac{\langle u_{REF} \rangle + c_g}{2\alpha}$ such that for $\langle A \rangle > \langle A_c \rangle$, $\frac{d\langle F_\lambda \rangle}{d\langle A \rangle} < 0$ and vice versa. This means that when $\langle A \rangle > \langle A_c \rangle$ and where LWA increases in longitude $\left(\frac{\partial \langle A \rangle}{\partial \lambda} > 0 \right)$, LWA grows with time, i.e.

$$\begin{aligned} 0 < \frac{\partial}{\partial t} \langle A \rangle \cos\phi &\approx -\frac{1}{a\cos\phi} \frac{\partial \langle F_\lambda \rangle}{\partial \lambda} = -\frac{1}{a\cos\phi} \frac{\partial \langle A \rangle}{\partial \lambda} \frac{d\langle F_\lambda \rangle}{d\langle A \rangle} \\ &\approx -\frac{1}{a\cos\phi} \frac{\partial \langle A \rangle}{\partial \lambda} \frac{d[F_2]}{d\langle A \rangle} - \frac{1}{a\cos\phi} \frac{\partial \langle A \rangle}{\partial \lambda} \frac{d[(F_1 + F_3)]}{d\langle A \rangle} \end{aligned} \tag{4.7}$$

From Eq. (4.6), $\frac{d[(F_1+F_3)]}{d\langle A \rangle} > 0$ since $u_{REF} + c_g$ is generally positive and $\frac{d[F_2]}{d\langle A \rangle} < 0$. So the growth of LWA $\left(\frac{\partial}{\partial t} \langle A \rangle \cos\phi > 0 \right)$ is due to the convergence of the nonlinear flux F_2. The situation is opposite of the normal downflow advection in which convergence of $F_1 + F_3$ dominates the LWA tendency, and this causes 'traffic congestion' of wave activity.

NH18 go on to partition LWA into stationary and transient wave components and show

that the modulation of the jet speed by a forced stationary Rossby wave provides bottlenecks to the transient wave traffic and localizes block formation.

4.2.4 Definition of anomalous events and persistence

We evaluate the applicability of traffic-jam mechanism by a Track changes is on nalyzing all the persistent jet anomalies during the NH winter in ERA-Interim reanalysis data from 1979-2018. We examine the full LWA budget during these events on different timescales.

We define the anomalous wave activity events as $\langle A\cos\phi\rangle > 55ms^{-1}$. The choice may appear arbitrary but is reasonable because $\langle F_\lambda\rangle$ maximizes at an intermediate wave activity range of 50 to 60 ms^{-1} in the exit regions of the NP and NA storm track (see Fig. 4 of NH18), i.e. it is close to the threshold value in the midlatitudes.

In order to identify anomalous events and to quantify their persistence during boreal winter between 1979-2018, we employ a simple feature-tracking algorithm to the daily wave activity field [see Eq. (4.1)] for all regions of the NH storm track. The algorithm sequentially searches for overlapping contours of $\langle A\rangle\cos\phi = 55ms^{-1}$. Two consecutive contours 24 hours apart are considered to be part of the same event if their area of intersection is at least 60% of their average area. The search for overlapping contours is iterated in a time window of 25 days till no significant overlap is found. This process is repeated for all days during the DJF months of a given year. Events that persist for less than 3 days are discarded. The location of anomalous persistent events are identified by the centroid location of the contours and their persistence is defined by the number of consecutive overlapping days.

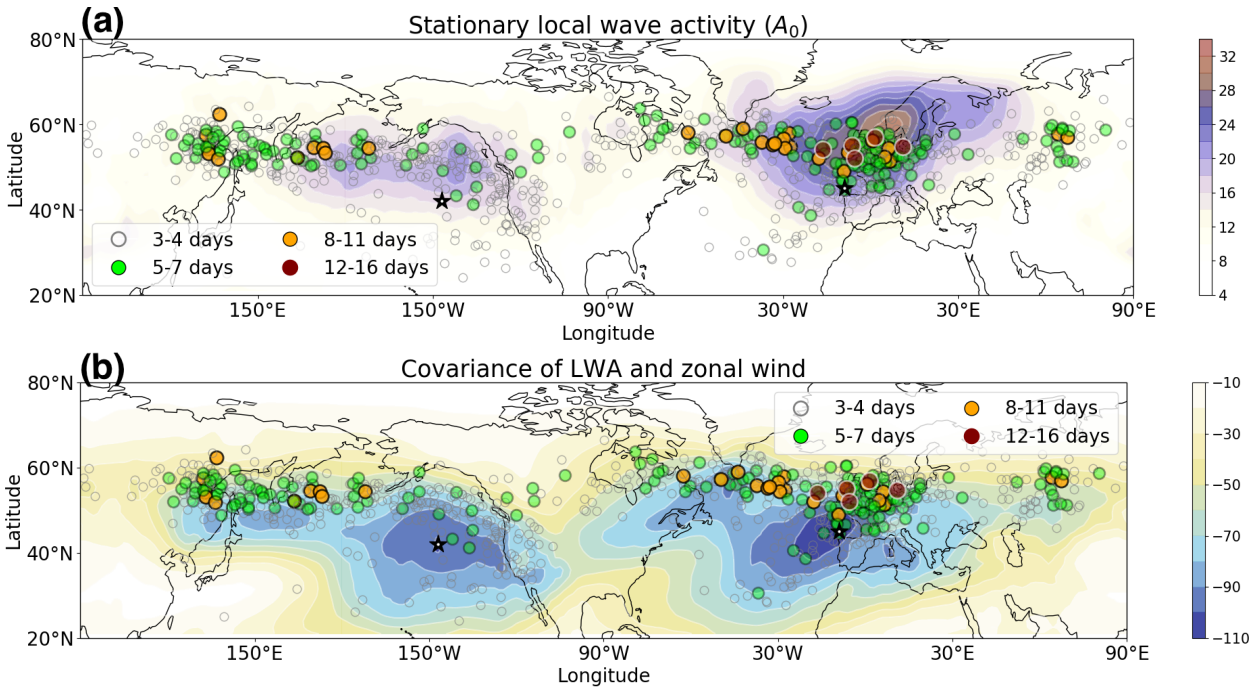

Figure 4.2: (a) Quasistationary LWA ($A_o \cos\phi$) in ms^{-1} and (b) the covariance between $\langle A \rangle$ and $\langle u \rangle$ in $m^2 s^{-2}$ in the boreal winter averaged for the years 1979-2018. Colored markers represent the location and persistence of anomalous wave activity events that occurred between 1979 and 2018 during boreal winter. The two black stars in (a) and (b) denote regions with maximum negative correlation between $\langle u \rangle$ and $\langle A \rangle \cos\phi$.

4.3 Results

4.3.1 Spatial distribution of anomalous events

A pertinent question that we seek to answer is, do all large wave activity events beyond a certain threshold lead to persistent blocks? Using the tracking algorithm described above, we identify all the anomalous wave activity events that occurred during boreal winter between 1979-2018. We find that majority of the short-lived events (3-4 days) are distributed roughly throughout the storm track (gray circles in Fig. 4.2). But the longer events (>5 days) form clusters over the preexisting quasi-stationary ridge of the NA and to a lesser extent the NP storm tracks (Held *et al.*, 2002; Wang & Ting, 1999) (Fig. 4.2a). In Fig. 4.2a, the quasi-stationary LWA ($A_0 \cos\phi$) is defined as the 40-year average of the minimum LWA

observed during DJF. This agrees well with the prediction of NH18 and Paradise *et al.* (2019). Recent modeling work by Narinesingh *et al.* (2020) also shows the importance of topographically forced stationary Rossby waves on the persistence of blocking. Additionally, the event clusters correspond to slightly north of the regions of maximum negative correlation between wave activity and zonal wind (Fig. 4.2b). The covariance is a measure of the nonlinear zonal LWA flux [Eqs (4.4) and (4.6)] and maximizes at the exit regions of the storm tracks (NH18). The spatial distribution of the persistent events are consistent with the previously identified regions where atmospheric blocks frequently form (Barriopedro *et al.*, 2006; Pelly & Hoskins, 2003a).

A closer analysis of the long-lived events show that they also capture a few key characteristics of atmospheric blocks (e.g. Nakamura (1994)). Figure 4.3 illustrates the composite lifecycle of 16 anomalous events that persisted for 7 days in the NA region. Table 4.1 lists all the events used in the composite. The anomalous wave activity (Fig. 4.3a) captures large-amplitude Rossby wave which is predominantly anticyclonic characterized by a persistent high pressure system (Fig. 4.3b) and local deceleration of the zonal wind (Fig. 4.3c).

However, not all anomalous events live long enough to be characterized as atmospheric blocks. Majority of the large wave activity events still dissipate in 3-4 days. This suggests that the critical value of LWA (55 ms^{-1}) used to identify persistent events may not exhibit a sharp threshold behavior, potentially due to contributions from processes other than zonal convergence of LWA flux such as diabatic processes and damping effects.

4.3.2 LWA budget covariances on different timescales

A key assumption behind the traffic-jam mechanism for block formation is that zonal convergence of LWA flux dominates the LWA variability on synoptic timescale (NH18). While previous work has focused on the exit region of NH storm tracks, in this section, we re-evaluate this assumption on different timescales for all locations of the storm track.

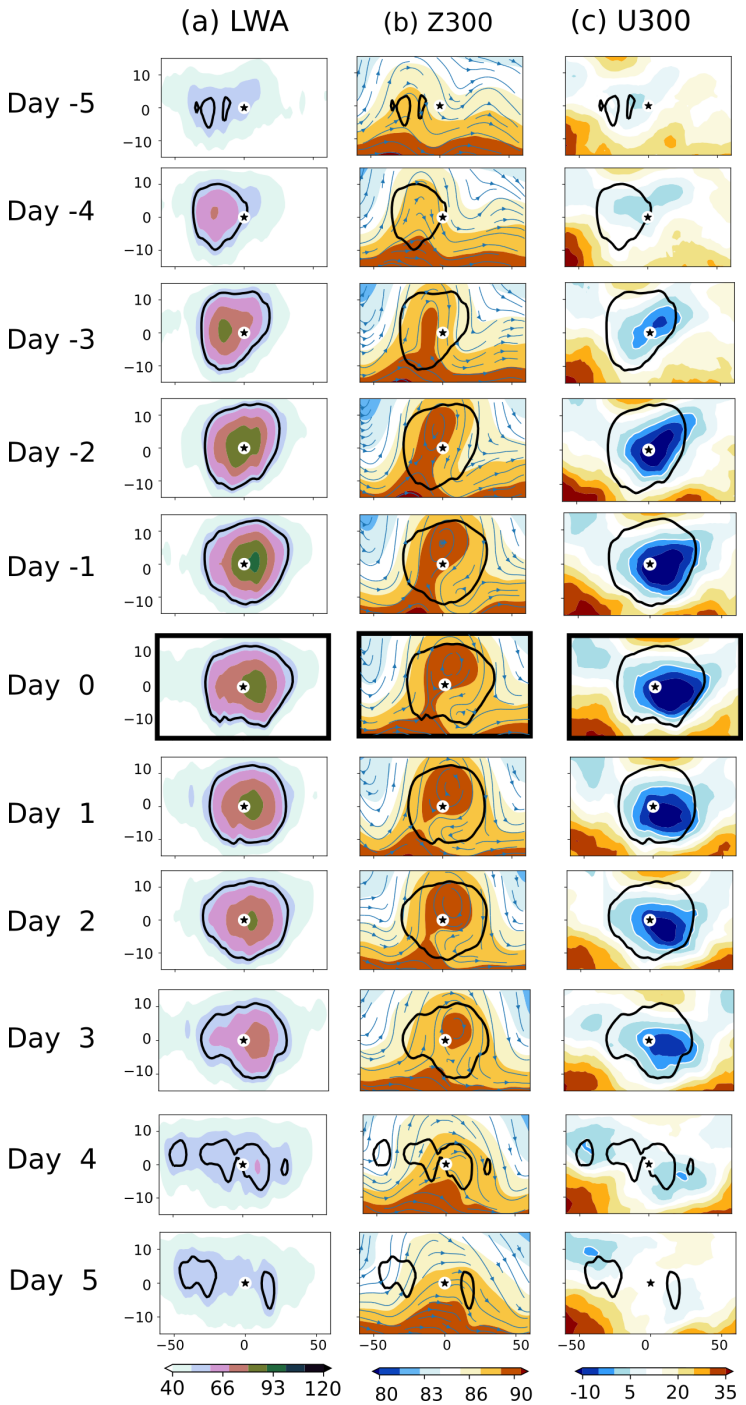

Figure 4.3: Composite 7-day lifecycle of anomalous events in the NA region during NH winter from 1979-2018 showing (a) $\langle A \rangle \cos\phi$ in ms^{-1}, (b) geopotential height at 300hPa in km (colors), zonal and meridional wind streams at 300hPa (blue contours) and (c) zonal wind speed at 300hPa in ms^{-1}. The black contours denote region where $\langle A \rangle \cos\phi = 55 ms^{-1}$. The x,y axes are longitude & latitude shifted with respect to the centroid location of the anomalous events at day 0 (black star).

Table 4.1: NA anomalous events with 7 day persistence

Event number	Peak date	Location
1	1981-Jan-30	3.0 E, 48.0 N
2	1982-Jan-16	9.0 E, 51.0 N
3	1986-Feb-20	37.5 W, 58.5 N
4	1992-Jan-12	12.0 W, 48.0 N
5	1995-Jan-19	33.0 E, 52.5 N
6	1999-Feb-1	1.5 W, 49.5 N
7	2001-Jan-14	0.0 E, 52.5 N
8	2001-Dec-22	40.5 W, 52.5 N
9	2003-Jan-7	21.0 W, 55.5 N
10	2006-Dec-22	3.0 E, 52.5 N
11	2007-Jan-25	27.0 W, 52.5 N
12	2010-Jan-11	13.5 W, 55.5 N
13	2011-Jan-3	55.5 W, 55.5 N
14	2013-Feb-25	6.0 W, 49.5 N
15	2016-Jan-1	28.5 E, 57.0 N
16	2017-Jan-19	3.0 E, 51.0 N

The change in LWA over time Δt is obtained by integrating the LWA budget Eq. (4.2) as follows:

$$\Delta\langle A\rangle\cos\phi = \underbrace{\mathbf{I}\left(-d_xF\right)}_{\mathbf{I}(-d_xF_1)+\mathbf{I}(-d_xF_2)+\mathbf{I}(-d_xF_3)} + \mathbf{I}\left(-d_yEP_y\right) + \mathbf{I}\left(-EP_z|_{z=0}\right) + \mathbf{I}\left(residual\right) \quad (4.8)$$

where $\mathbf{I}$ denotes time integral $\int_t^{t+\Delta t}(\,)\,dt$ and $\left(-d_xF,\ -d_yEP_y,\ -EP_z|_{z=0},\ residual\right)$ represent the RHS terms of the LWA budget [Eq. (4.2)] and $(-d_xF_1,\ -d_xF_2,\ -d_xF_3)$ represent the zonal convergence of the RHS terms in Eq. (4.3). We compute the variance of LWA (LHS) and its covariance with each of the RHS terms in Eq. (4.8) to identify the dominant contribution to LWA variability for different lengths of time.

For Δt = 1 day, variance of LWA, $\Delta\langle A\rangle\cos\phi$ (Fig. 4.4a) is widely dominated by its covariance with time-integrated zonal LWA flux convergence, $\mathbf{I}\left(-d_xF\right)$ in the storm track

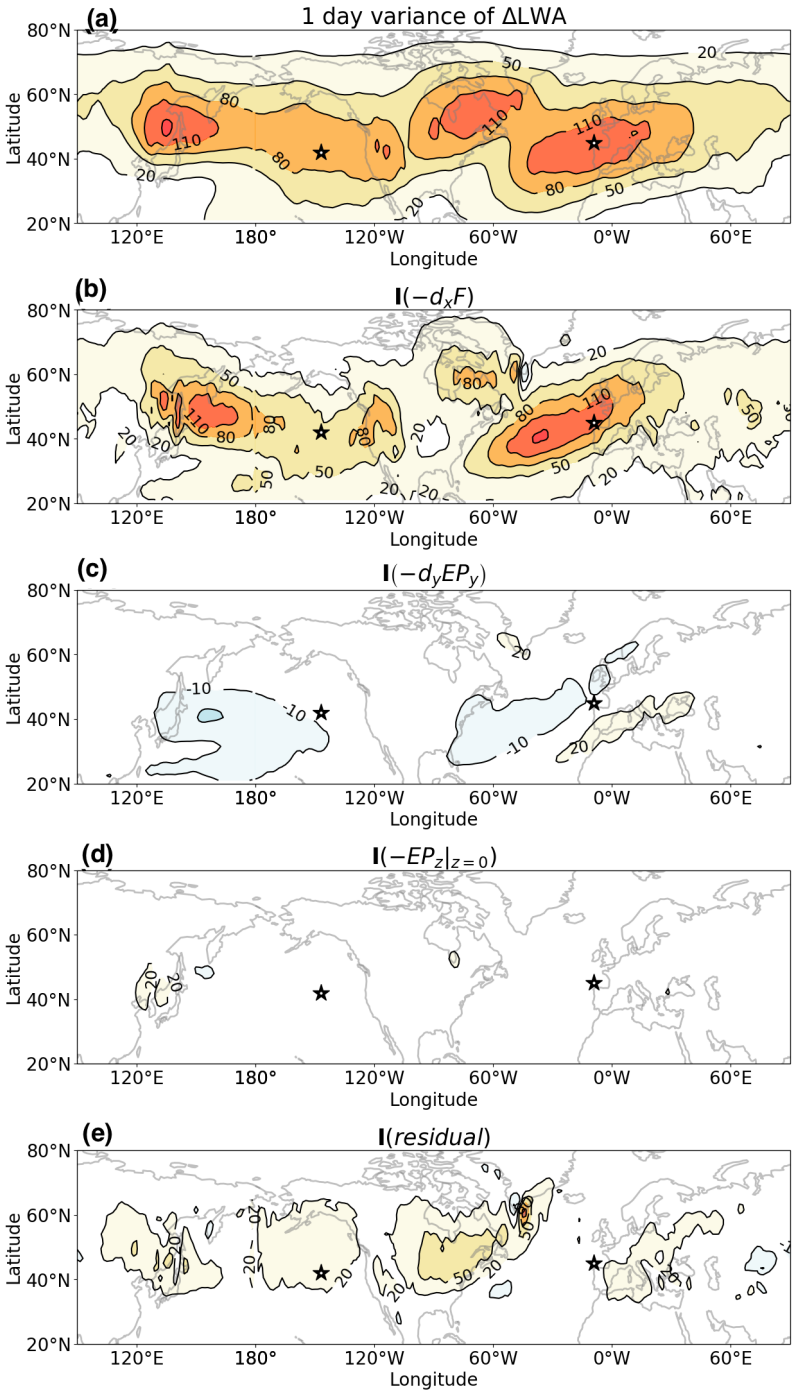

Figure 4.4: (a) 1-day variance of LWA and its covariance in $m^2 s^{-2}$ with the RHS terms of LWA budget, namely, (b) zonal convergence of LWA flux, (c) meridional convergence of EP flux, (d) near-surface meridional eddy heat flux and (e) diabatic sources and sinks [see Eq. (4.2)]. The black stars denote two locations in the exit regions of NP and NA storm track (same as in Fig. 4.2).

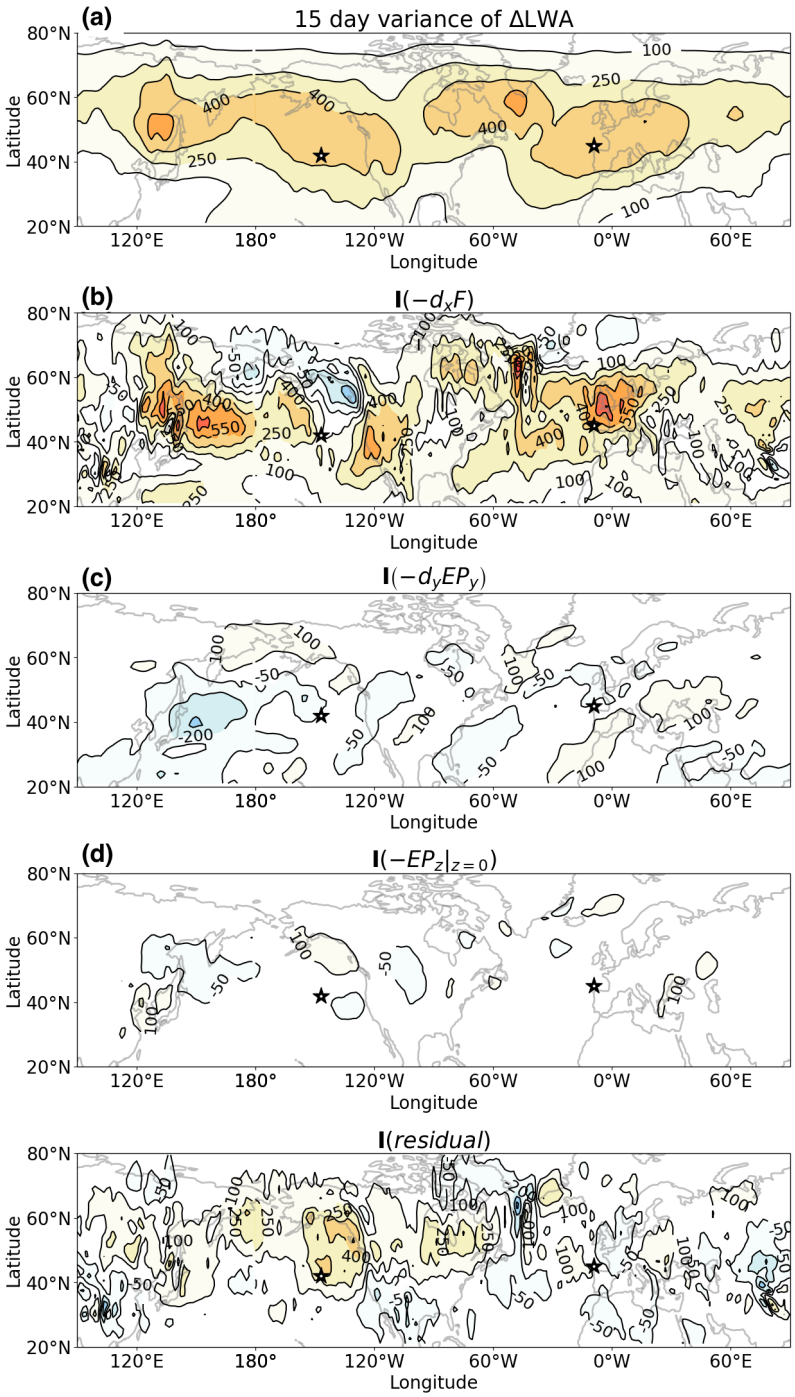

Figure 4.5: Same as in Fig. 4.4 but for 15-day variance and covariances.

regions (Fig. 4.4b). Whereas other terms including meridional divergence of eddy momentum fluxes, $\mathbf{I}\left(-d_y EP_y\right)$ and near-surface meridional eddy heat flux, $\mathbf{I}\left(-EP_z|_{z=0}\right)$ play much smaller role (Fig. 4.4c,d). The diabatic sources and sink term, $\mathbf{I}\left(residual\right)$ also contribute to LWA variance, albeit to a smaller extent over the north eastern portion of the North American continent, the southern tip of Greenland and the exit region of NP storm track (Fig. 4.4e). These results are consistent with Huang & Nakamura (2016, 2017).

However for $\Delta t = 15$ day, which approximately corresponds to the maximum duration of most persistent anomalous wave activity, we find that the relative contribution of $\mathbf{I}\left(-d_x F\right)$ to LWA variability reduces and other terms in the RHS of Eq. (4.8) gain importance. For example, the entrance and exit regions of NP storm track sees significant contribution from diabatic sources, whereas in the entrance region of the NA storm track, both the residual term and the convergence of the meridional LWA flux are negative, slightly offsetting the positive convergence of the zonal LWA flux. (Fig. 4.5).

Figure 4.6 illustrates the timescale dependence of the covariance terms at two locations of the NP and NA storm track exit. The covariance values are normalized by variance of $\Delta\langle A\rangle \cos\phi$, so all the terms in Fig. 4.6 a,c add up to 1. The terms that are closer to 1 explain maximum variance in $\Delta\langle A\rangle \cos\phi$.

In the NA region, the zonal convergence of LWA flux term, $\mathbf{I}\left(-d_x F\right)$ dominates the LWA variability up to a timescale of ~20 day (red line in Fig. 4.6a) while the rest of the terms are very small. For the most part, $\mathbf{I}\left(-d_x F\right)$ is dominated by the linear component of zonal LWA fluxes, $\mathbf{I}\left(-d_x F_1 - d_x F_3\right)$ (blue and red lines in Fig. 4.6b). Beyond 20 days, the diabatic source and sink term, $\mathbf{I}\left(residual\right)$ become important (black line in Fig. 4.6a). Additionally around ~18 day timescale, both linear, $\mathbf{I}\left(-d_x F_1 - d_x F_3\right)$ and nonlinear, $\mathbf{I}\left(-d_x F_2\right)$ components of zonal LWA flux contribute equally to the total flux convergence (blue and orange lines in Fig. 4.6b)[1]. This suggests that traffic-jam mechanism may be relevant only for very

1. The linear component of zonal LWA fluxes is due to group propagation of the Rossby waves and the nonlinear component is due to nonlinear modification of the flux by large-amplitude waves [see Eq. (4.3)].

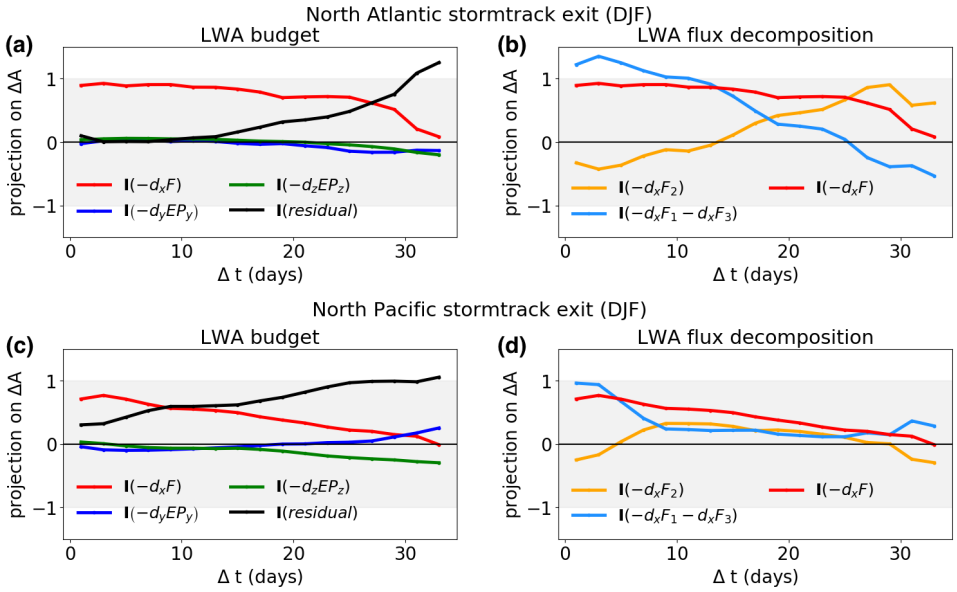

Figure 4.6: Covariance of LWA $(\Delta\langle A\rangle\cos\phi)$ with (a,c) RHS terms of the LWA budget [see Eq. (4.8)] and (b,d) decomposition of zonal LWA flux convergence as function of timescale at the exit region of NA (top) and NP storm track (bottom). The covariance values are normalized by $\langle\Delta A\cos\phi\rangle^2$. The gray shading denotes the region less than 1.

long timescales in the NA.

In the NP region, the zonal convergence of LWA flux term, $\mathbf{I}\left(-d_xF\right)$ dominates the LWA variability up to a very short timescale (<8 days). In contrast to the NA, the diabatic source term, $\mathbf{I}\left(residual\right)$ has significant contribution even on synoptic timescales (<10 days) (black and red lines in Fig. 4.6c). The rest of the terms $\mathbf{I}\left(-EP_z|_{z=0}\right)$, $\mathbf{I}\left(-d_yEP_y\right)$ are however small (Fig. 4.6c). Around 10 day timescale, the linear and non-linear components of LWA flux contribute equally to the total flux convergence (orange and blue lines in Fig. 4.6d). This suggests that in the Pacific region, the traffic jam mechanism may be acting at much shorter timescales than in the Atlantic.

Crossing of the blue and orange curves in Fig. 4.6b,d is a circumstantial evidence for traffic jam mechanism at work. Overall, the covariance analysis reveals the predominance of the zonal LWA flux in controlling LWA in the storm tracks but also suggests that the traffic-jam dynamics is timescale dependent.

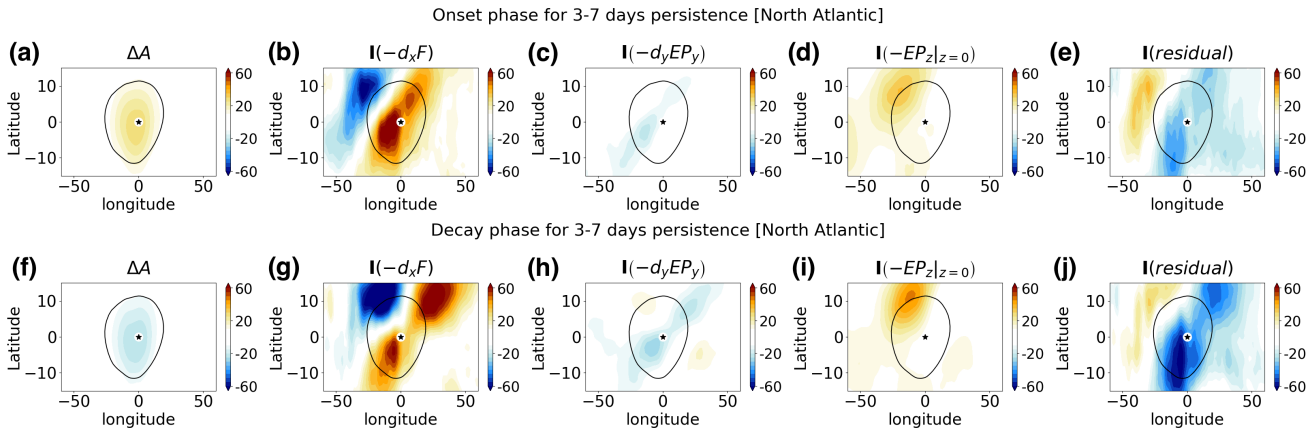

Figure 4.7: (a,f) Change in LWA and the corresponding change in RHS terms of the time integrated LWA budget [see Eq. (4.8)], namely, (b,g) zonal convergence of LWA flux, (c,h) meridional divergence of eddy momentum flux, (d,i) near surface meridional eddy heat flux and (e,j) diabatic sources and sinks of LWA during the onset (top) and decay (bottom) of short-lived (3-7 day) anomalous events in the NA storm track. The black contour represents $\langle\overline{A(t_{peak})}\rangle \cos\phi = 55\ ms^{-1}$ where $\overline{A(t_{peak})}$ denotes composite mean of LWA during the peak of events. The x,y axes are longitude & latitude shifted with respect to the centroid location of the anomalous events (black star).

4.3.3 Wave activity budget of anomalous events

The foregoing analysis underscores the general importance of the zonal propagation of LWA in the storm track regions, but it has been applied to uniformly sampled periods during the boreal winter. Here we apply the same analysis to composites of anomalous wave activity events to determine what controls their growth and decay.

We divide all the events identified in section 4.3.1 into two categories based on their persistence: (1) 3-7 days and (2) 8-16 days. Time-integrated LWA budget Eq. (4.8) is applied to composites of each category separately in their onset stage and decay stage. The onset stage is defined for $\Delta t = t_{peak} - t_{onset}$ and the decay stage is defined for $\Delta t = t_{decay} - t_{peak}$ where $t_{decay} - t_{onset}$ represents persistence of each event.

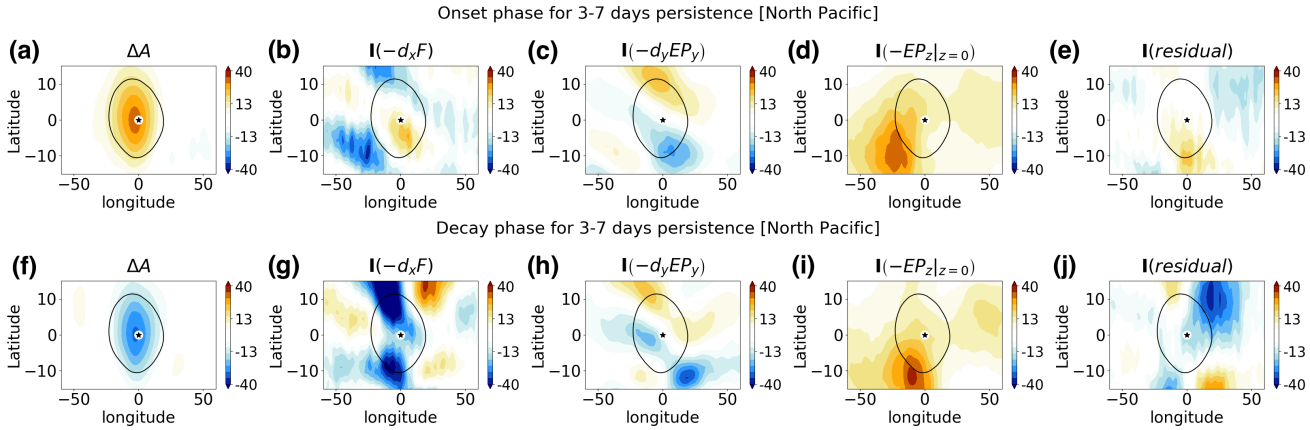

Figure 4.8: Same as in Fig. 4.7 but for short-lived (3-7 day) anomalous events in the NP storm track.

Short-lived anomalous events

A composite analysis of the short-lived (3-7 day) anomalous events in the NA and NP cluster are shown in Figs. 4.7 and 4.8 respectively. NA cluster includes events whose centroid locations are inside $60°W$ to $60°E$ longitude and 45N to 60N latitude. NP cluster includes events whose centroid locations are inside $120°E$ to $120°W$ longitude and 45N to 60N latitude (See Fig. 4.2). Refer Appendix B for the list of events in the two clusters.

During the onset stage of NA events, the increase of LWA, $\Delta\langle A\rangle\cos\phi$ (Fig. 4.7a) is predominantly balanced by positive contribution from zonal flux convergence, $\mathbf{I}\left(-d_xF\right)$ (Fig. 4.7b) and a smaller negative contribution from the residual term, $\mathbf{I}\left(residual\right)$ (Fig. 4.7e). Other terms including meridional divergence of eddy momentum flux, $\mathbf{I}\left(-d_yEP_y\right)$ and near surface meridional eddy heat flux $\mathbf{I}\left(-EP_z|_{z=0}\right)$ play no significant role in the growth of wave activity (Fig. 4.7c,d).

During the decay stage of NA events, the decrease of LWA, $\Delta\langle A\rangle\cos\phi$ (Fig. 4.7f) is largely due to the negative contribution from the residual term, $\mathbf{I}\left(residual\right)$ (Fig. 4.7j). This term likely represents dissipation of LWA by mixing process (local dissipation of enstrophy). Interestingly the contribution from the zonal flux convergence, $\mathbf{I}\left(-d_xF\right)$ is still positive, but

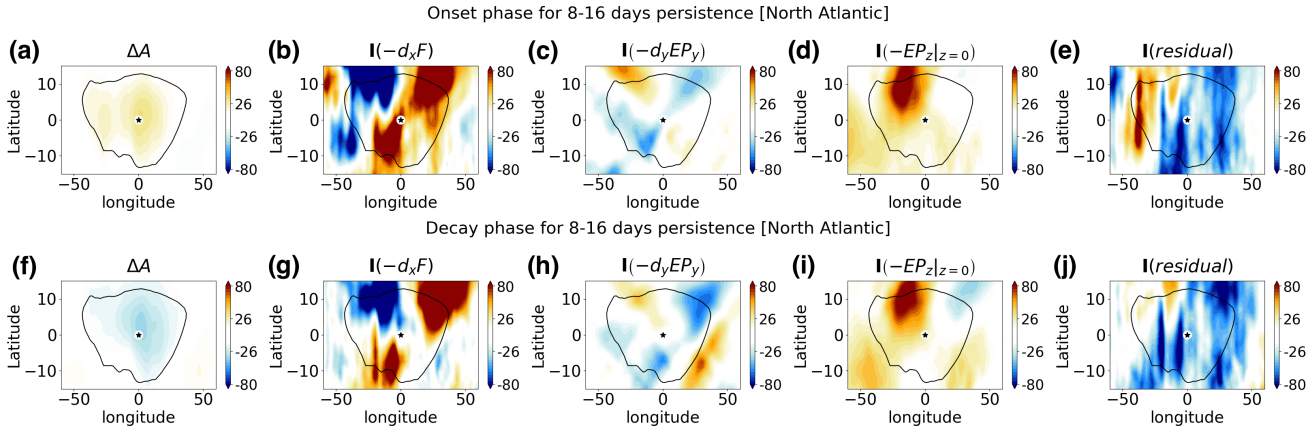

Figure 4.9: Same as in Fig. 4.7 but for persistent (8-16 day) anomalous events in the NA storm track.

it is overwhelmed by the negative residual term (Fig. 4.7j). Other terms including meridional divergence of eddy momentum flux, $\mathbf{I}\left(-d_y EP_y\right)$ and near surface meridional eddy heat flux $\mathbf{I}\left(-EP_z|_{z=0}\right)$ play no significant role in the decay phase of wave activity (Fig. 4.7h,i).

Contrary to the NA events, during the onset stage of the short-lived NP events, both zonal flux convergence, $\mathbf{I}\left(-d_x F\right)$ (Fig. 4.8b) and near surface meridional eddy heat flux $\mathbf{I}\left(-EP_z|_{z=0}\right)$ (Fig. 4.8d) contribute to the growth of LWA, $\Delta\langle A\rangle\cos\phi$. The magnitude of other terms including meridional divergence of eddy momentum flux, $\mathbf{I}\left(-d_y EP_y\right)$ and the residual term, $\mathbf{I}\left(residual\right)$ (Fig. 4.7c,e) are also comparable, but they do not contribute to the overall growth of the wave.

During the decay stage of the short-lived NP events, the decrease of LWA, $\Delta\langle A\rangle\cos\phi$ (Fig. 4.8f) sees a negative contribution from all the terms (particularly the convergence of the zonal LWA flux $\mathbf{I}\left(-d_x F\right)$) except the near-surface meridional eddy heat flux which remains positive $\mathbf{I}\left(-EP_z|_{z=0}\right)$ (Fig. 4.8g-i).

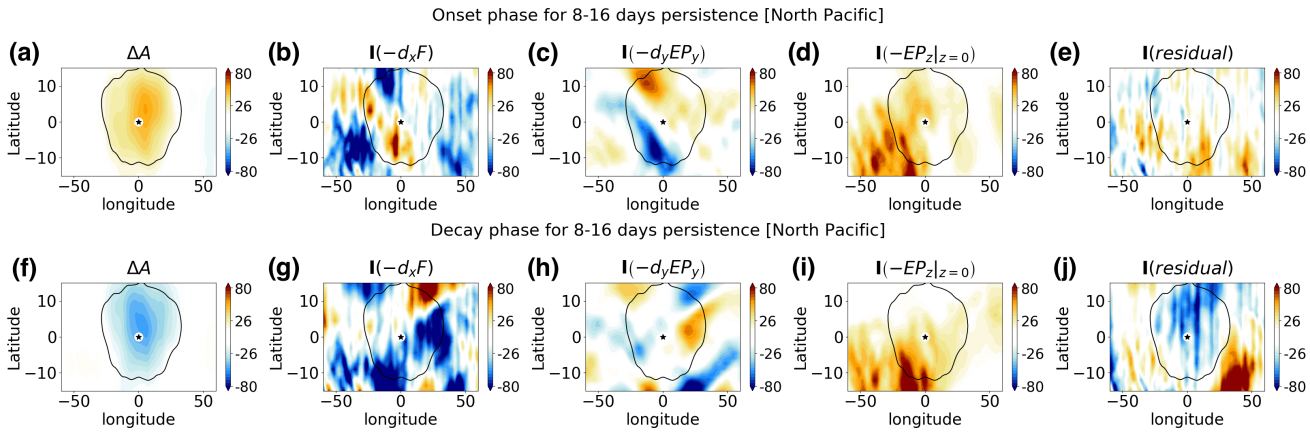

Figure 4.10: Same as in Fig. 4.9 but for persistent (8-16 day) anomalous events in the NP storm track.

Persistent anomalous events

A composite analysis of the persistent (8-16 day) events in the NA and NP clusters are shown in Figs. 4.9 and 4.10.

Similar to the short-lived events, the onset stage of the persistent events in NA region sees an increase in $\Delta\langle A\rangle\cos\phi$ (Fig. 4.9a) which is dominated by positive contribution from zonal flux convergence, $\mathbf{I}\left(-d_xF\right)$ (Fig. 4.9b) and damping effect from the $\mathbf{I}\left(residual\right)$ (Fig. 4.9e). However, the other two terms; $\mathbf{I}\left(-d_yEP_y\right)$ and $\mathbf{I}\left(-EP_z|_{z=0}\right)$ are not negligible. Particularly, the near-surface meridional eddy heat flux plays some role in the growth of the wave (Fig. 4.9d). During the decay stage of the persistent events, the flux distributions are similar to those during the growth stage, but their magnitude decreases overall, and this yields a net negative $\Delta\langle A\rangle\cos\phi$ (Fig. 4.9f). (Note that for the persistent events, the change in LWA is relatively small compared to the individual flux contributions.)

The persistent events in the NP region are qualitatively similar to the short-lived events except that each of the terms are relatively of higher magnitude (Compare Figs. 4.10 and 4.8). In summary, the composite analysis shows that for all the anomalous events in the NP and NA cluster, zonal convergence of LWA plays a dominant role in the growth of wave

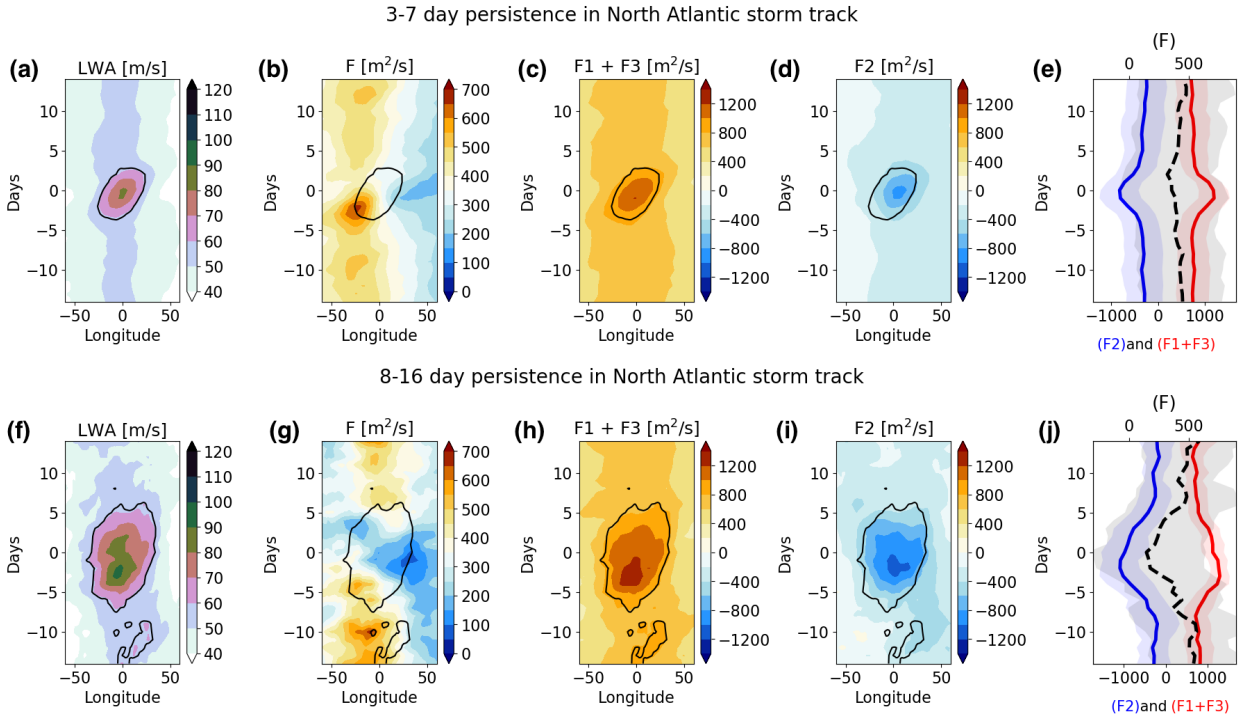

Figure 4.11: Composite longitude-time diagram of (a,f) LWA, (b,g) $\langle F_\lambda \rangle$, (c,h) F1 + F3 and (d,i) F2 in the NA storm track. (e,j) shows the 1D composite time evolution of the LWA fluxes shown in left but measured at the centroid of the events where the upper x axis is for $\langle F_\lambda \rangle$ (black dashed line) and bottom y axis is for F1+F3 (red line) and F2 (blue line). The red, blue and black curves are composite mean and the shading denotes 1 standard deviation from their mean values. Top row is for events with 3-7 days persistence and bottom row is for events with 8-16 day persistence. The black contours denote $\langle A \rangle cos\phi = 55ms^{-1}$. The x axes is longitude shifted with respect to the centroid location of the anomalous events

activity during the onset stage. Except for the short-lived events in the Pacific, the residual term[2] has a damping effect on wave activity. Near surface meridional eddy heat flux also aids in the growth of wave activity, albeit its effect is stronger in the NP region. The meridional eddy momentum flux divergence plays no significant contribution to the growth of anomalous wave activity.

2. The residual term involves all the non-conservative sources and sinks of LWA which includes diabatic heating, dissipation through mixing, radiative and Ekman damping.

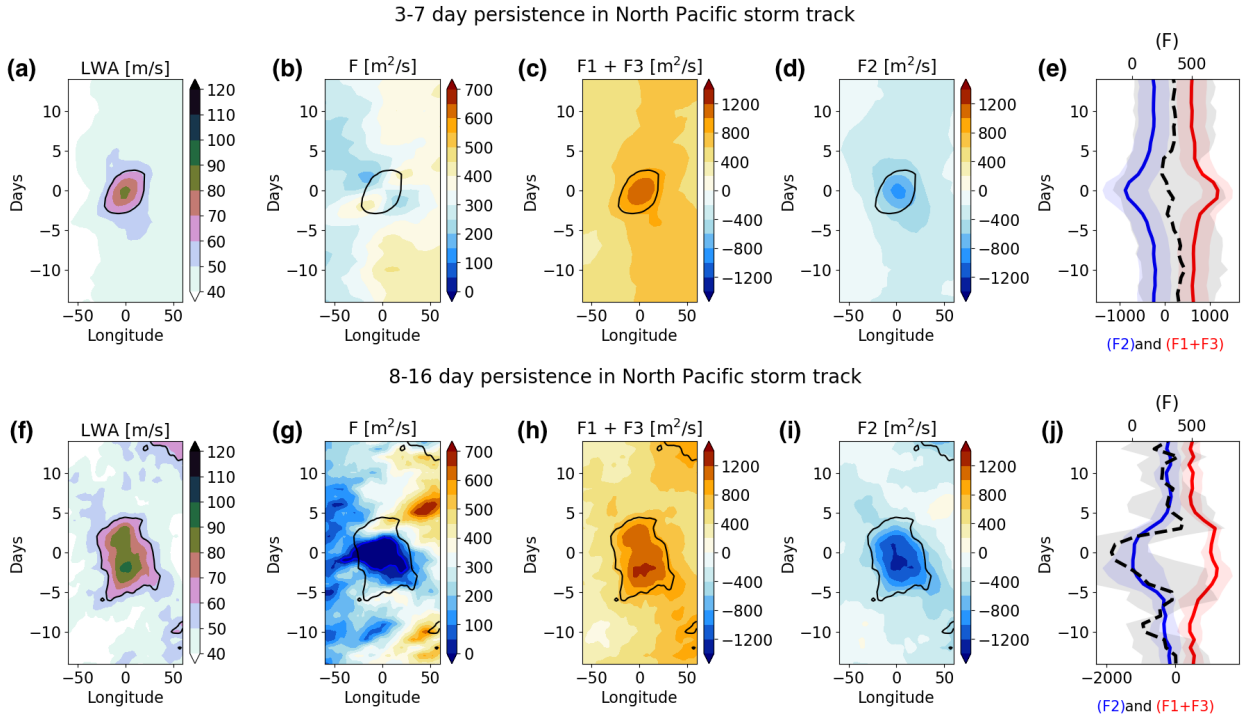

Figure 4.12: Same as in Fig. 4.11 but for NP storm track.

4.3.4 Zonal LWA flux evolution of anomalous events

While zonal convergence of LWA flux plays a dominant role during the onset of anomalous wave activity, a key question about the relevance of traffic-jam mechanism still remains: To what extent does the LWA flux exhibit a 'threshold behavior' as predicted by the traffic-jam theory? In other words, is the blocking onset marked by a maximum zonal LWA flux, followed by a precipitous drop in the flux as blocks mature? [See Eq. (4.6)]. To address this question, we analyze the composite time-evolution of LWA $\langle A\cos\phi\rangle$, LWA flux $\langle F_\lambda\rangle$ and its decomposition into linear (F_1+F_3) and nonlinear (F_2) components for both short-lived and persistent anomalous events in the NP and NA clusters (Figs. 4.11 and 4.12).

For the anomalous events of NA region, the increase in LWA around day 0, $\langle A\cos\phi\rangle$ (Figs. 4.11a,f) is accompanied by a corresponding increase in the linear component of the flux, F_1+F_3 (Figs. 4.11c,h). At the same time, the magnitude of negative nonlinear component, F_2

also increases (Figs. 4.11d,i). As a result of their partial compensation, the total zonal LWA flux maximizes shortly before the event in the immediate upstream (Figs. 4.11b,g). These observations qualitatively agree with the $\langle A \rangle$-$\langle F_\lambda \rangle$ relationship prescribed by the conceptual 'traffic-jam' model [see Eq. (4.6)].

However, for the short-lived events the negative increase of nonlinear component, F_2 is not large enough to fully compensate the positive increase of linear component, $F_1 + F_3$. As a result, the net LWA flux, $\langle F_\lambda \rangle$ around day 0 is weaker but not completely suppressed (Fig. 4.11b). On the other hand, in case of persistent events of the NA region, the magnitude of nonlinear component, F_2 around day 0 is large (Figs. 4.11h) and overcompensates the increase of flux due to linear component, $F_1 + F_3$ (Fig. 4.11g). As a result, the net LWA flux, $\langle F_\lambda \rangle$ is efficiently suppressed during the peak of the anomalous persistent event (Figs. 4.11f). The upper bound of the net LWA flux (F_{max}) for NA region is found to be $\approx 500 m^2 s^{-2}$.

The composite of events in the NP show similar time evolution of LWA and LWA fluxes compared to those in the NA. However, the upstream seeding of LWA flux is noticeably weaker than in the NA (Fig. 4.12). F_{max} for NP region is found to be $\approx 250 m^2 s^{-2}$.

In summary, in both the NA and Pacific regions, the LWA flux, $\langle F_\lambda \rangle$ is suppressed past the peak when blocks mature (See Figs. 4.11j and 4.12j). However, the suppression of the flux is incomplete for the short-lived anomalous (3-7 days) events due to partial compensation between linear and nonlinear LWA flux components (See Figs. 4.11e and 4.12e). The incomplete suppression of the flux and the short duration of blocks are arguably due to short-lived seeding of LWA flux from upstream. Complete, persistent blocking of a traffic requires a sustained influx of traffic from upstream.

4.4 Summary and discussion

The 1D traffic-jam model is a conceptual model for atmospheric blocking and is built on three key ingredients: 1) LWA and the zonal wind are anti-correlated where the regression slope

gives a measure of nonlinear interaction strength, 2) the column averaged LWA is driven by zonal convergence of LWA flux, and 3) there exists an upper bound for the zonal LWA flux beyond which the flux decreases with an increasing LWA due to nonlinear wave-flow interaction noted in section 4.3.4. The goal of this study is to quantify the extent to which the above descriptions hold in the real atmosphere for cases of large wave activity events.

We analyze the column-averaged LWA budget in DJF during the years 1979-2018 using ERA-Interim Reanalysis dataset. For synoptic timescales, the role of zonal LWA flux is of leading order of importance in the wave activity budget. However, for longer timescales (>15 days), other processes including diabatic heating and near-surface meridional eddy heat flux also play important role.

Motivated by results from NH18, we identify the anomalous large wave activity events using a feature-tracking algorithm with the criteria LWA > 55 ms^{-1}. We find that most of the anomalous persistent events form two clusters, one over the Euro-Atlantic sector and the other over the Pacific sector. The geographical distribution of these events is consistent with the climatology of atmospheric blocks found using other blocking indices (Tibaldi & Molteni, 1990; Barnes *et al.*, 2014). The clusters are also collocated with regions of stronger quasi-stationary wave activity and maximum anti-correlation of LWA and zonal wind. These results are consistent with NH18 and Paradise *et al.* (2019) which is suggestive of the fact that on an average large wave activity events become persistent by traffic-jam mechanism.

However, the traffic-jam mechanism is timescale- and location dependent. In the Euro-Atlantic sector, the zonal flux of LWA plays a dominant role up to around ~ 18 days beyond which the residual term becomes more important. The low-level eddy heat flux also becomes a source of LWA, albeit at much longer timescales (>30 days) at the entrance region of the storm track. The effect of the nonlinear zonal LWA flux is small on short timescales and it overtakes the linear effect at around 20 days. In contrast, in the Pacific sector, the linear and nonlinear LWA flux contributions become comparable around ~ 8 days. And overall there

is a much stronger influence of the residual term compared to the Atlantic. These results suggest that in the Atlantic sector, while zonal LWA flux generally plays more important role than in Pacific, but the nonlinear effect manifests at much longer timescales. These observations are consistent with Nakamura *et al.* (1997) who showed that the low-frequency dynamics plays a greater role in the formation of Euro-Atlantic blocks, whereas transient wave forcing plays more important role in the Pacific.

The residual term includes all the nonconservative processes that affect LWA, namely, damping through mixing (local dissipation of enstrophy) and wave activity source by diabatic heating (latent heating). The more significant role of the residual term during the growth phase of the anomalous events in the NP suggests that latent heating may be playing an important role during the growth of large wave activity events. Note the positive contribution of the residual term in Figs. 4.8e and 4.10e., and also in the upstream of the block in Fig. 4.9e. This is consistent with a recent work by Pfahl *et al.* (2015) who showed that in addition to horizontal advection of potential vorticity, the ascent from lower levels associated with the latent heating in clouds is equally important for the formation and maintenance of certain cases of atmosphere blocks. Although it is difficult to evaluate directly the contribution from diabatic heating to the anomalous wave activity event, the residual of the LWA budget appears to capture some aspects of it. However, the predominant role of the residual term during the life cycle of an anomalous event (in both regions) is to damp LWA, particularly during the decay phase of blocks, presumably associated with destruction of LWA by mixing. This lends support to the linear damping representation of LWA sink in NH18 and Paradise *et al.* (2019).

Finally, using composite analysis of the anomalous events, we show that most persistent events are associated with stronger nonlinear modification of large-amplitude Rossby waves. In such cases the total LWA flux is effectively suppressed. In contrast, the short-lived anomalous events are associated with weaker nonlinear component of LWA flux which results in

ineffective flux suppression, although even for these events the zonal LWA flux does reach a peak value, a tipping point for spontaneous accumulation of LWA. The fast dispersal of short-lived events may be attributed to a short supply of LWA input from the upstream to sustain LWA accumulation against damping.

In summary, we show that despite substantial variations among individual events most of the long-lived events exhibit essential elements of the canonical traffic-jam description. In the current climate, the exact value of LWA at which the zonal flux of LWA maximizes shows significant scatter between 50-60 ms^{-1}. However, a changing climate may shift this range significantly and affect the frequency/persistence of blocks (NH18, Paradise *et al.*, 2019). Therefore, this dynamical framework can be useful for understanding the trends of atmosphere blocking in past and future climate states (Woollings *et al.*, 2018).

Although the main goal of this study is to elucidate the LWA budgets associated with large, persistent wave events, the theoretical framework is applicable for a broad range of topics associated with the storm track dynamics. For example, Figs. 4.4 and 4.5 identify the regions in which diabatic heating is potentially important as a forcing mechanism of synoptic- to intra-seasonal scale disturbances. They also reveal a surprisingly small role of low-level meridional heat flux as a forcing mechanism. In future, the wave-activity budget will be used to evaluate the lifecycle of a cyclone to study the storm track dynamics.

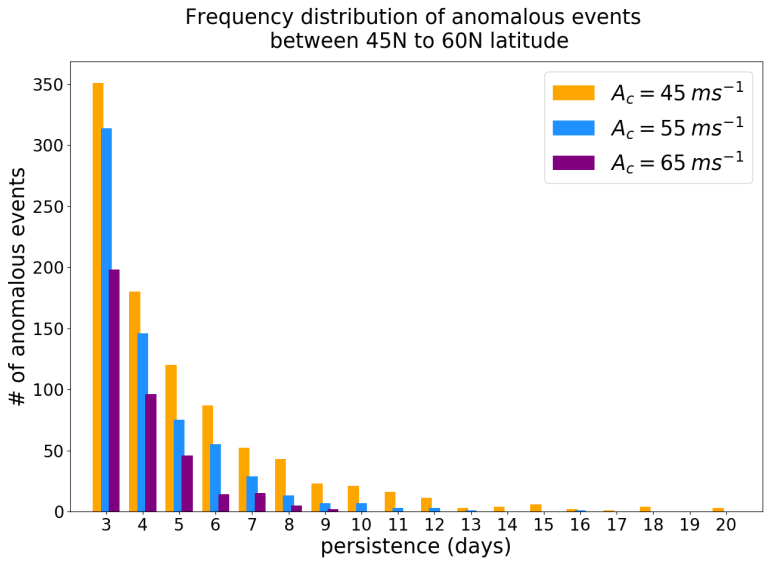

Figure 4.13: Frequency distribution of anomalous events for different threshold values

4.5 Appendices

4.5.1 Appendix A: Sensitivity of anomalous events to threshold value

Figure 4.13 shows the frequency distribution and Figure 4.14a,b shows the geographical distribution of anomalous events for different threshold values of local wave activity.

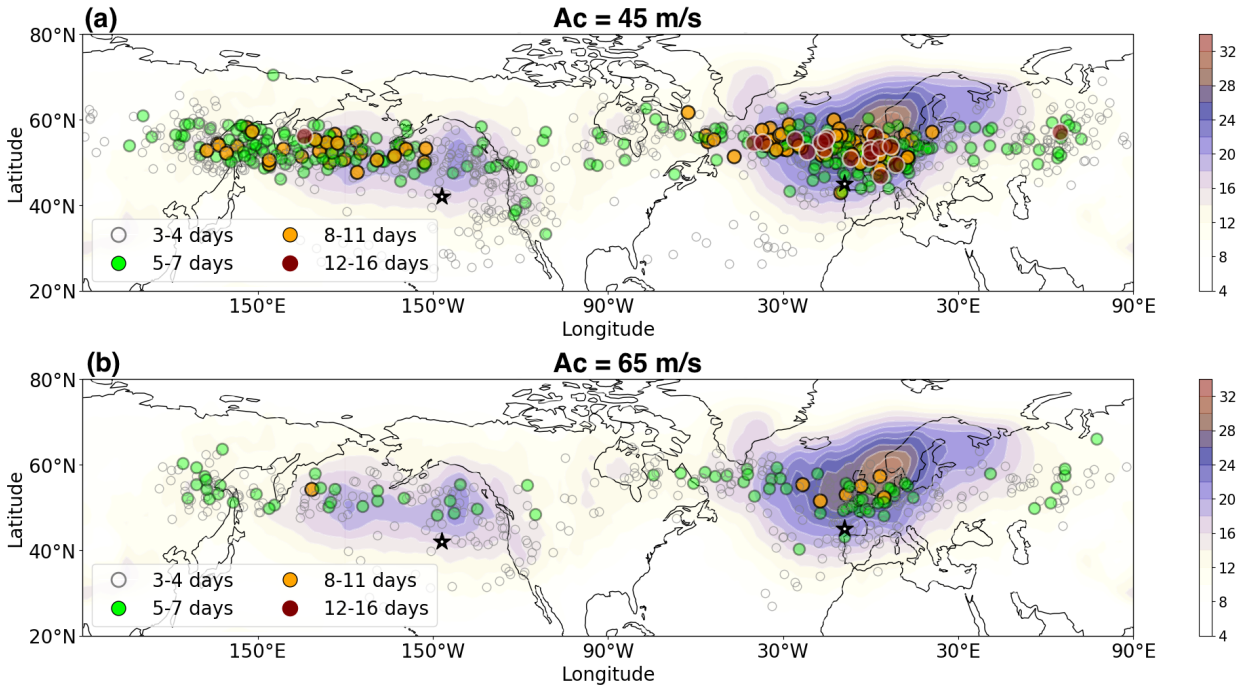

Figure 4.14: (a,b) Quasistationary LWA (color map) in ms^{-1} in the boreal winter averaged for the years 1979-2018. Colored markers represent the location and persistence of anomalous wave activity events obtained using (a) $\langle A \rangle \cos\phi = 45 ms^{-1}$ and (b) $\langle A \rangle \cos\phi = 65 ms^{-1}$.

CHAPTER 5

CONCLUSIONS

Extratropical storm tracks play a major role in shaping the Earth's climate by transporting energy, moisture and momentum through the atmosphere. Any change in their average position and intensity will have a major impact on the midlatitude weather and global climate.

In this thesis, we use energy and momentum conservation equations to study the dynamics of extratropical storm track on different timescales. The main goals of this thesis are (i) to develop a new energetic framework for storm track shift that can be connected to external radiative forcings, (ii) to provide a deeper understand about why storm tracks exhibit different hemispheric seasonality on Earth, and (iii) to improve our dynamical understanding of atmospheric block formation within the storm track.

In Chapter 2, we developed a new Moist Static Energy (MSE) framework for storm track position and used it to understand storm track shifts in response to seasonal insolation, El Niño minus La Niña conditions and two hypothetical warming scenarios. We found that:

- The net energy input in the atmosphere is not a dominant contribution for storm track shifts across the timescales considered.

- The stationary eddy contribution dominates the storm track shift in response to seasonal insolation, El Niño minus La Niña conditions, and increased CO_2 over land in the Northern Hemisphere.

- The mean meridional circulation contribution dominates the shift in response to increased sea surface temperature during boreal winter in Northern Hemisphere and during May and October in the Southern Hemisphere.

- The equatorward storm track shift in response to El Niño minus La Niña conditions

during boreal winter involves a different regime than the poleward shift in response to increased CO_2 even though the tropical upper troposphere warms in both cases.

In Chapter 3, we use the MSE framework with idealized modelling experiments to explain why storm tracks exhibit hemispheric asymmetry in seasonal timescale even though both hemisphere receive roughly the same solar insolation.

- We start with an assumption that Southern Hemisphere is like a large mixed layer depth regime due to greater ocean coverage and the Northern Hemisphere is like a small mixed layer depth regime due to relatively larger land coverage.

- We then define a critical mixed layer depth d_c using scaling analysis and hypothesize that 1) large mixed layer depths ($d > d_c$) produce surface heat fluxes that are out of phase with shortwave absorption and 2) small mixed layer depths ($d < d_c$) produce surface heat fluxes that are in phase with shortwave absorption. By MSE balance, storm track seasonality must be small for large mixed layer depth and it should be large for small mixed layer depth.

- We establish the casual role of surface fluxes in modulating storm track seasonality by varying the mixed layer depth in (1) a zonally symmetric slab-ocean aquaplanet with zero ocean energy transport and (2) a 1D energy balance model with fixed diffusivity.

- We show that the aquaplanet simulations confirm the large mixed layer depth hypothesis and yield a useful idealization of the SH storm track.

- However, the small mixed layer limit does not yield a useful idealization of the NH storm track due to larger contribution of the Ferrel cell and atmospheric storage.

- We show that the EBM qualitatively supports the aquaplanet results.

In Chapter 4, we used the finite amplitude local wave activity budget and performed a careful analysis of major persistent anomalies in the jet streams during the Northern

Hemisphere winter. The main goal of this study was to identify signatures of traffic-jam mechanism during the onset of persistent anomalies. We found that:

- The role of zonal LWA flux is of leading order of importance in the wave-activity budget for synoptic timescales. However, for longer timescales (>15 days), other processes including diabatic heating and near-surface meridional eddy heat flux also play important role.

- Using an LWA threshold of 55m/s in a feature-tracking algorithm yields a reasonable distribution of persistent jet anomalies that resemble winter-time atmosphere blocks in terms of their geographical distribution and persistence.

- Most of the anomalous persistent events form two clusters over the Euro-Atlantic sector and the Pacific sector which are collocated with regions of stronger quasi-stationary wave activity and maximum anti-correlation of LWA and zonal wind.

- The influence of zonal LWA flux in the North Atlantic sector is dominant for longer timescale (up to ~20 days), whereas in the Pacific sector, both diabatic heating and zonal LWA flux are equally important in the wave activity budget.

- Most persistent events are associated with stronger nonlinear modification of large-amplitude Rossby waves. In such cases the total LWA flux is effectively suppressed and the events show 'threshold behavior'. In contrast, the short-lived anomalous events are associated with weaker nonlinear component of LWA flux which results in ineffective flux suppression. Such cases do not exhibit 'threshold behavior'.

- Overall, the results suggest that on an average large wave-activity events become persistent by traffic-jam mechanism. The fast dispersal of some anomalous events may be attributed to damping effects from non-conservative processes like dissipation through mixing, radiative & Ekman damping and dissipation due to meridional eddy momentum flux divergence.

This thesis advances our understanding about storm track dynamics on different timescales. Chapter 2 introduces a new moist static energy framework which is a first attempt to make a quantitative connection between storm track shift and radiative forcing. Chapter 3 successfully uses the framework in idealized modelling experiments to explain hemispheric asymmetry in storm track seasonality. However, our new framework has a much wider scope of application. In future, it can be used along with other theoretical frameworks to study storm track changes in response to different anthropogenic forcings, namely, ozone hole recovery, black carbon warming or in a snowball earth. Finally, chapter 4 evaluates a relatively new traffic-jam model for wintertime atmosphere blocking using reanalysis dataset. The simplicity of the model and its effectiveness in application to realistic meteorological dataset is encouraging. In future, it can be used with realistic climate change simulations from Coupled Model Intercomparison Project - Phase 6 to test several hypothesis about future projections of atmosphere blocking.

REFERENCES

Adam, O., Bischoff, T., & Schneider, T. 2016a. Seasonal and interannual variations of the energy flux equator and ITCZ. Part I: Zonally averaged ITCZ position. *J. Climate*, **29**, 3219–3230.

Adam, O., Bischoff, T., & Schneider, T. 2016b. Seasonal and interannual variations of the energy flux equator and ITCZ. Part II: Zonally varying shifts of the ITCZ. *J. Climate*, **29**, 7281–7293.

Altenhoff, Adrian M., Martius, Olivia, Croci-Maspoli, Mischa, Schwierz, Cornelia, & Davies, Huw C. 2008. Linkage of atmospheric blocks and synoptic-scale Rossby waves: a climatological analysis. *Tellus A: Dynamic Meteorology and Oceanography*, **60**(5), 1053–1063.

Anderson, GFDL Global Atmospheric Model Development Team, Jeffrey L, Balaji, V, Broccoli, Anthony J, Cooke, William F, Delworth, Thomas L, Dixon, Keith W, Donner, Leo J, Dunne, Krista A, Freidenreich, Stuart M, *et al.* 2004. The new GFDL global atmosphere and land model AM2-LM2: Evaluation with prescribed SST simulations. *J. Climate*, **17**(24), 4641–4673.

Barnes, Elizabeth A, Slingo, Julia, & Woollings, Tim. 2012. A methodology for the comparison of blocking climatologies across indices, models and climate scenarios. *Climate dynamics*, **38**(11-12), 2467–2481.

Barnes, Elizabeth A., Dunn-Sigouin, Etienne, Masato, Giacomo, & Woollings, Tim. 2014. Exploring recent trends in Northern Hemisphere blocking. *Geophysical Research Letters*, **41**(2), 638–644.

Barpanda, Pragallva, & Shaw, Tiffany A. 2017. Using the moist static energy budget to understand storm-track shifts across a range of time scales. *J. Atmos. Sci.*, **74**(8), 2427–2446.

Barpanda, Pragallva, & Shaw, Tiffany A. 2020. Surface Fluxes Modulate the Seasonality of Zonal-Mean Storm Tracks. *Journal of the Atmospheric Sciences*, **77**(2), 753–779.

Barriopedro, David, García-Herrera, Ricardo, Lupo, Anthony R., & Hernández, Emiliano. 2006. A Climatology of Northern Hemisphere Blocking. *Journal of Climate*, **19**(6), 1042–1063.

Berggren, R., Bolin, B., & Rossby, C.-G. 1949. An Aerological Study of Zonal Motion, its Perturbations and Break-down. *Tellus*, **1**(2), 14–37.

Betts, Alan K, & Miller, Martin J. 1993. The Betts-Miller scheme. *Pages 107–121 of: The representation of cumulus convection in numerical models*. Springer.

Bischoff, T., & Schneider, T. 2014. Energetic constraints on the position of the intertropical convergence zone. *J. Climate*, **27**, 4937–4951.

Bischoff, T., & Schneider, T. 2016. The equatorial energy balance, ITCZ position, and double ITCZ bifurcations. *J. Climate*, **29**, 2997–3013.

Bordoni, Simona, & Schneider, Tapio. 2008. Monsoons as eddy-mediated regime transitions of the tropical overturning circulation. *Nature Geosc.*, **1**(8), 515.

Brayshaw, D. J., Hoskins, B., & Blackburn, M. 2008. The Storm-Track Response to Idealized SST Perturbations in an Aquaplanet GCM. *J. Atmos. Sci.*, **65**, 2842–2860.

Brayshaw, D. J., Hoskins, B., & Black, E. 2010. Some physical drivers of changes in the winter storm tracks over the North Atlantic and Mediterranean during the Holocene. *Phil. Trans. R. Soc. A*, **368**, 5158–5223.

Butchart, N., Haines, K., & Marshall, J. C. 1988. A Theoretical and Diagnostic Study of Solitary Waves and Atmospheric Blocking. *Journal of the Atmospheric Sciences*, **46**(13), 2063–2078.

Butler, A. H., Thompson, D. W. J., & Heikes, R. 2010. The Steady-State Atmospheric Circulation Response to Climate Change-like Thermal Forcings in a Simple General Circulation Model. *J. Climate*, **23**, 3474–3496.

Cash, Benjamin A., & Lee, Sukyoung. 2000. Dynamical Processes of Block Evolution. *Journal of the Atmospheric Sciences*, **57**(19), 3202–3218.

Ceppi, P., & Hartmann, D. L. 2015. Connections Between Clouds, Radiation, and Midlatitude Dynamics: A Review. *Curr. Clim. Change Rep.*, **1**, 94–102.

Chang, E. 2001. GCM and Observational Diagnoses of the Seasonal and Interannual Variations of the Pacific Storm Track during the Cool Season. *J. Atmos. Sci.*, **58**, 1784–1800.

Chang, E., Lee, S., & Swanson, K. K. 2002. Storm Track Dynamics. *J. Climate*, **15**, 2163–2183.

Charney, Jule G., & DeVore, John G. 1979. Multiple Flow Equilibria in the Atmosphere and Blocking. *Journal of the Atmospheric Sciences*, **36**(7), 1205–1216.

Chen, G., & Held, I. M. 2007. Phase speed spectra and the recent poleward shift of Southern Hemisphere surface westerlies. *Geophys. Res. Lett.*, **34**.

Colucci, Stephen J. 1985. Explosive Cyclogenesis and Large-Scale Circulation Changes: Implications for Atmospheric Blocking. *Journal of the Atmospheric Sciences*, **42**(24), 2701–2717.

Colucci, Stephen J. 2001. Planetary-Scale Preconditioning for the Onset of Blocking. *Journal of the Atmospheric Sciences*, **58**(8), 933–942.

Dee, D. P., Uppala, S. M., Simmons, A. J., Berrisford, P., Poli, P., Kobayashi, S., Andrae, U., Balmaseda, M. A., Balsamo, G., Bauer, P., Bechtold, P., Beljaars, A. C. M., van de Berg, L., Bidlot, J., Bormann, N., Delsol, C., Dragani, R., Fuentes, M., Geer, A. J., Haimberger, L., Healy, S. B., Hersbach, H., Hólm, E. V., Isaksen, L., Kållberg, P., Köhler, M., Matricardi, M., McNally, A. P., Monge-Sanz, B. M., Morcrette, J.-J., Park, B.-K., Peubey, C., de Rosnay, P., Tavolato, C., Thépaut, J.-N., & Vitart, F. 2011. The ERA-Interim reanalysis: configuration and performance of the data assimilation system. *Quarterly Journal of the Royal Meteorological Society*, **137**(656), 553–597.

Delworth, Thomas L, Broccoli, Anthony J, Rosati, Anthony, Stouffer, Ronald J, Balaji, V, Beesley, John A, Cooke, William F, Dixon, Keith W, Dunne, John, Dunne, KA, *et al.* 2006. GFDL's CM2 global coupled climate models. Part I: Formulation and simulation characteristics. *J. Climate*, **19**(5), 643–674.

Demirtaş, Meral. 2017. The large-scale environment of the European 2012 high-impact cold wave: prolonged upstream and downstream atmospheric blocking. *Weather*, **72**(10), 297–301.

Donohoe, A., & Battisti, D. S. 2013. The seasonal cycle of atmospheric heating and temperature. *J. Climate*, **26**, 4962–4980.

Donohoe, A., Frierson, D. M. W., & Battisti, D. S. 2014. The effect of ocean mixed layer depth on climate in slab ocean aquaplanet experiments. *Clim. Dynamics*, **43**, 1041–1055.

Dwyer, J., & O'Gorman, P. A. 2016. Moist formulations of the Eliassen-Palm flux and their connection to the surface westerlies. *J. Atmos. Sci.*, in press.

Fasullo, J. T., & Trenberth, K. E. 2008. The annual cycle of the energy budget. Part I: Global mean and land-ocean exchanges. *J. Climate*, **21**, 2297–2312.

Freidenreich, SM, & Ramaswamy, V. 1999. A new multiple-band solar radiative parameterization for general circulation models. *Journal of Geophysical Research: Atmospheres*, **104**(D24), 31389–31409.

Gates, W. L., Boyle, J. S., Covey, C., Dease, C. G., Doutriaux, C. M., Drach, R. S., Fiorino, M., Gleckler, P. J., Hnilo, J. J., Marlais, S. M., Phillips, T. J., Potter, G. L., Santer, B. D., Sperber, K. R., Taylor, K. E., & Williams, D. N. 1999. An Overview of the Results of the Atmospheric Model Intercomparison Project (AMIP I). *Bull. Amer. Met. Soc.*, **80**, 29–55.

Geen, Ruth, Lambert, FH, & Vallis, GK. 2018. Regime change behavior during Asian monsoon onset. *J. Climate*, **31**(8), 3327–3348.

Gerber, E., & Son, S.-W. 2014. Quantifying the Summertime Response of the Austral Jet Stream and Hadley Cell to Stratospheric Ozone and Greenhouse Gases. *J. Climate*, **27**, 5538–5559.

Green, JSA. 1977. The weather during July 1976: Some dynamical considerations of the drought. *Weather*, **32**(4), 120–126.

Grise, K. M., Son, S.-W., Correa, G. J. P., & Polvani, L. M. 2014. The response of extratropical cyclones in the Southern Hemisphere to stratospheric ozone depletion in the 20th Century. *Atmos. Sci. Lett.*, **15**, 29–36.

Hawcroft, M. K., Shaffrey, L. C., Hodges, K. I., & Dacre, H. F. 2012. How much Northern Hemisphere precipitation is associated with extratropical cyclones? *Geophysical Research Letters*, **39**(24).

He, J., & Soden, B. J. 2016. Does the Lack of Coupling in SST-Forced Atmosphere-Only Models Limit Their Usefulness for Climate Change Studies? *J. Climate*, **29**, 4317–4325.

He, J., Soden, B. J., & Kirtman, B. 2014. The robustness of the atmospheric circulation and precipitation response to future anthropogenic surface warming. *Geophys. Res. Lett.*

Held, I. M., & Schneider, T. 1999. The Surface Branch of the Zonally Averaged Mass Transport Circulation in the Troposphere. *J. Atmos.Sci.*, **56**, 1688–1697.

Held, I. M., Ting, M., & Wang, H. 2002. Northern Winter Stationary Waves: Theory and Modeling. *J. Climate*, **15**, 2125–2144.

Held, Isaac M. 2019. 100 Years of Progress in Understanding the General Circulation of the Atmosphere. *Meteorological Monographs*, **59**(04), 6.1–6.23.

Holte, James, Talley, Lynne D, Gilson, John, & Roemmich, Dean. 2017. An Argo mixed layer climatology and database. *Geophys. Res. Lett.*, **44**(11), 5618–5626.

Hoskins, B. J., & Hodges, K. I. 2005. A New Perspective on Southern Hemisphere Storm Tracks. *Journal of Climate*, **18**(20), 4108–4129.

Hoskins, Brian J., & Hodges, Kevin I. 2002. New Perspectives on the Northern Hemisphere Winter Storm Tracks. *Journal of the Atmospheric Sciences*, **59**(6), 1041–1061.

Hoskins, Brian J, & Valdes, Paul J. 1990. On the existence of storm-tracks. *J. Atmos. Sci.*, **47**(15), 1854–1864.

Huang, Clare S. Y., & Nakamura, Noboru. 2016. Local Finite-Amplitude Wave Activity as a Diagnostic of Anomalous Weather Events. *Journal of the Atmospheric Sciences*, **73**(1), 211–229.

Huang, Clare S. Y., & Nakamura, Noboru. 2017. Local wave activity budgets of the wintertime Northern Hemisphere: Implication for the Pacific and Atlantic storm tracks. *Geophysical Research Letters*, **44**(11), 5673–5682.

Kalnay, E., & Coauthors. 1996. The NCEP/NCAR 40-year reanalysis project. *Bull. Amer. Met. Soc.*, **77**, 437–472.

Kang, S. M., & Polvani, L. M. 2011. The interannual relationship between the latitude of the eddy-driven jet and the edge of the Hadley cell. *J. Climate*, **24**, 563–568.

Kaspi, Y., & Schneider, T. 2013. The Role of Stationary Eddies in Shaping Midlatitude Storm Tracks. *J. Atmos. Sci.*, **70**, 2596–2613.

Kidston, J., & Vallis, G. K. 2012. The Relationship between the Speed and the Latitude of an Eddy-Driven Jet in a Stirred Barotropic Model. *J. Atmos. Sci.*, **69**, 3251–3263.

Kushner, Paul J, & Held, Isaac M. 1998. A test, using atmospheric data, of a method for estimating oceanic eddy diffusivity. *Geophys. Res. Lett.*, **25**(22), 4213–4216.

Lachmy, O., & Shaw, T. A. 2018. Connecting the Energy and Momentum Flux Response to Climate Change Using the Eliassen-Palm Relation. *J. Climate*, **31**, 7401–7416.

Lee, S., & Feldstein, S. B. 2013. Detecting Ozone- and Greenhouse Gas- Driven Wind Trends with Observational Data. *Science*, 10.1126/science.1225154.

Li, C., & Battisti, D. S. 2008. Reduced Atlantic Storminess during Last Glacial Maximum: Evidence from a Coupled Climate Model. *J. Climate*, **21**, 3561–3579.

Lorenz, D. J. 2014. Understanding Midlatitude Jet Variability and Change Using Rossby Wave Chromatography: Poleward-Shifted Jets in Response to External Forcing. *J. Atmos. Sci.*, **71**, 2370–2389.

Lorenz, D. J., & DeWeaver, E. 2007. Tropopause height and zonal wind response to global warming in the IPCC scenario integrations. *J. Geophys. Res.*, **112**.

Lu, J., Chen, G., & Frierson, D. M. W. 2008. Response of the zonal mean atmospheric circulation to El Niño versus global warming. *J. Climate*, **21**, 5835–5851.

Lu, J., Chen, G., & Frierson, D. M. W. 2010. The position of the midlatitude storm track and eddy-driven westerlies in aquaplanet AGCMs. *J. Atmos. Sci.*, **67**, 3984–4000.

Lu, J., Sun, L., Wu, Y., & Chen, G. 2014. The Role of Subtropical Irreversible PV Mixing in the Zonal Mean Circulation Response to Global Warming-Like Thermal Forcing. *J. Climate*, **27**, 2297–2316.

Luo, Dehai, Zhang, Wenqi, Zhong, Linhao, & Dai, Aiguo. 2019. A Nonlinear Theory of Atmospheric Blocking: A Potential Vorticity Gradient View. *Journal of the Atmospheric Sciences*, **76**(8), 2399–2427.

Manabe, S., & Terpstra, T. B. 1974. The effects of mountains on the general circulation of the atmosphere as identified by numerical experiments. *J. Atmos. Sci.*, **31**, 3–42.

Marshall, J., Donohoe, A., Ferreira, D., & McGee, D. 2013. The ocean's role in setting the mean position of the Inter-Tropical Convergence Zone. *Clim. Dyn.*

Mbengue, C., & Schneider, T. 2013. Storm track shifts under climate change: What can be learned from large-scale dry dynamics. *J. Climate*, **26**, 9923–9930.

Mbengue, C., & Schneider, T. 2017. Storm track shifts under climate change: Toward a mechanistic understanding using local mean available potential energy. *J. Atmos. Sci.*, **74**, 93–110.

Mbengue, Cheikh, & Schneider, Tapio. 2018. Linking Hadley circulation and storm tracks in a conceptual model of the atmospheric energy balance. *J. Atmos. Sci.*, **75**(3), 841–856.

McLandress, C., Shepherd, T. G., Scinocca, J. F., Plummber, D. A., Sigmond, M., Jonsson, A. I., & Reader, M. C. 2011. Separating the Dynamical Effects of Climate Change and Ozone Depletion. Part II: Southern Hemisphere Troposphere. *J. Climate*, **24**, 1850–1868.

McWilliams, James C. 1980. An application of equivalent modons to atmospheric blocking. *Dynamics of Atmospheres and Oceans*, **5**(1), 43 – 66.

Ming, Y., Ramaswamy, V., & Chen, G. 2011. A Model Investigation of Aerosol-Induced Changes in Boreal Winter Extratropical Circulation. *J. Climate*, **24**, 6077–6091.

Mlawer, Eli J, Taubman, Steven J, Brown, Patrick D, Iacono, Michael J, & Clough, Shepard A. 1997. Radiative transfer for inhomogeneous atmospheres: RRTM, a validated correlated-k model for the longwave. *Journal of Geophysical Research: Atmospheres*, **102**(D14), 16663–16682.

Moorthi, Shrinivas, & Suarez, Max J. 1992. Relaxed Arakawa-Schubert. A parameterization of moist convection for general circulation models. *Mon. Wea. Rev.*, **120**(6), 978–1002.

Mullen, Steven L. 1987. Transient Eddy Forcing of Blocking Flows. *Journal of the Atmospheric Sciences*, **44**(1), 3–22.

Nakamura, Hisashi. 1992. Midwinter suppression of baroclinic wave activity in the Pacific. *J. Atmos. Sci.*, **49**(17), 1629–1642.

Nakamura, Hisashi. 1994. Rotational evolution of potential vorticity associated with a strong blocking flow configuration over Europe. *Geophysical Research Letters*, **21**(18), 2003–2006.

Nakamura, Hisashi, Nakamura, Mototaka, & Anderson, Jeffrey L. 1997. The Role of High- and Low-Frequency Dynamics in Blocking Formation. *Monthly Weather Review*, **125**(9), 2074–2093.

Nakamura, Noboru, & Huang, Clare S. Y. 2017. Local Wave Activity and the Onset of Blocking along a Potential Vorticity Front. *Journal of the Atmospheric Sciences*, **74**(7), 2341–2362.

Nakamura, Noboru, & Huang, Clare S. Y. 2018. Atmospheric blocking as a traffic jam in the jet stream. *Science*, **361**(6397), 42–47.

Nakamura, Noboru, & Zhu, Da. 2010. Finite-Amplitude Wave Activity and Diffusive Flux of Potential Vorticity in Eddy–Mean Flow Interaction. *Journal of the Atmospheric Sciences*, **67**(9), 2701–2716.

Narinesingh, V., Booth, J. F., Clark, S. K., & Ming, Y. 2020. Atmospheric blocking in an aquaplanet and the impact of orography. *Weather and Climate Dynamics*, **1**(2), 293–311.

Neelin, J. D., & Held, I. M. 1987. Modeling tropical convergence based on the moist static energy budget. *Mon. Wea. Rev.*, **115**, 3–12.

Novak, L., Schneider, T., & Chaalal, F. Ait. 2019. Midwinter Suppression of Zonally Symmetric Storm Tracks. *J. Atmos. Sci.*, submitted.

O'Gorman, P. A. 2010. Understanding the varied response of the extratropical storm tracks to climate change. *Proc. Nat. Acad. Sci.*, **107**, 19176–19180.

O'Gorman, P. A., & Schneider, T. 2008. Energy of Midlatitude Transient Eddies in Idealized Simulations of Changed Climates. *J. Climate*, **21**, 5797–5806.

Papritz, Lukas, & Spengler, Thomas. 2015. Analysis of the slope of isentropic surfaces and its tendencies over the North Atlantic. *Quarterly Journal of the Royal Meteorological Society*, **141**(693), 3226–3238.

Paradise, Adiv, Rocha, Cesar B., Barpanda, Pragallva, & Nakamura, Noboru. 2019. Blocking Statistics in a Varying Climate: Lessons from a "Traffic Jam" Model with Pseudostochastic Forcing. *Journal of the Atmospheric Sciences*, **76**(10), 3013–3027.

Park, H.-S., Xie, S.-P., & Son, S.-W. 2013. Poleward Stationary Eddy Heat Transport by the Tibetan Plateau and Equatorward Shift of Westerlies during Northern Winter. *J. Atmos. Sci.*, **70**, 3288–3301.

Peixoto, J. P., & Oort, A. H. 1992. *Physics of climate*. New York, NY: American Institute of Physics.

Pelly, J. L., & Hoskins, B. J. 2003a. A New Perspective on Blocking. *Journal of the Atmospheric Sciences*, **60**(5), 743–755.

Pelly, Joanna L., & Hoskins, Brian J. 2003b. How well does the ECMWF Ensemble Prediction System predict blocking? *Quarterly Journal of the Royal Meteorological Society*, **129**(590), 1683–1702.

Perlwitz, J., Pawson, S., Fogt, R. L., Nielsen, J. E., & Neff, W. D. 2008. Impact of stratospheric ozone hole recovery on Antarctic climate. *Geophys. Res. Lett.*, 10.1029/2008GL033317.

Pfahl, Stephan, & Wernli, Heini. 2012. Quantifying the Relevance of Cyclones for Precipitation Extremes. *Journal of Climate*, **25**(19), 6770–6780.

Pfahl, Stephan, Schwierz, Cornelia, Croci-Maspoli, Mischa, Grams, Christian M, & Wernli, Heini. 2015. Importance of latent heat release in ascending air streams for atmospheric blocking. *Nature Geoscience*, **8**(8), 610–614.

Polvani, L. M., Waugh, D., Correa, G. J. P., & Son, S.-W. 2011. Stratospheric Ozone Depletion: The Main Driver of Twentieth-Century Atmospheric Circulation Changes in the Southern Hemisphere. *J. Climate*, **24**, 795–812.

Rex, Daniel F. 1950. Blocking Action in the Middle Troposphere and its Effect upon Regional Climate. *Tellus*, **2**(4), 275–301.

Roberts, Chris D, Palmer, Matt D, Allan, Richard P, Desbruyeres, Damien G, Hyder, Pat, Liu, Chunlei, & Smith, Doug. 2017. Surface flux and ocean heat transport convergence contributions to seasonal and interannual variations of ocean heat content. *Journal of Geophysical Research: Oceans*, **122**(1), 726–744.

Rose, Brian EJ. 2018. Climlab: A python toolkit for interactive, process oriented climate modeling. *J. Open Source Software*, **3**(24), 659.

Schneider, T. 2006. The General Circulation of the Atmosphere. *Annu. Rev. Earth Planet. Sci.*

Schneider, T., & Bordoni, S. 2008. Eddy-Mediated Regime Transitions in the Seasonal Cycle of a Hadley Circulation and Implications for Monsoon Dynamics. *J. Atmos. Sci.*, **65**, 915–934.

Schneider, T., Bischoff, T., & Haug, G. H. 2014. Migrations and dynamics of the intertropical convergence zone. *Nature*.

Seager, R., Harnik, N., Kushnir, Y., Robinson, W., & Miller, J. 2003. Mechanisms of Hemispherically Symmetric Climate Variability. *J. Climate*, **16**, 2960–2978.

Seager, Richard, Naik, Naomi, & Vecchi, Gabriel A. 2010. Thermodynamic and dynamic mechanisms for large-scale changes in the hydrological cycle in response to global warming. *J. Climate*, **23**(17), 4651–4668.

Shaw, T. A. 2014. On the Role of Planetary-Scale Waves in the Abrupt Seasonal Transition of the Northern Hemisphere General Circulation. *J. Atmos. Sci.*, **71**, 1724–1746.

Shaw, T. A., & Voigt, A. 2015. Tug of war on summertime circulation between radiative forcing and sea-surface warming. *Nature Geosc.*, 10.1038/NGEO2449.

Shaw, T. A., & Voigt, A. 2016a. Land dominates the regional response to CO_2 direct radiative forcing. *Geophys. Res. Lett.*, 10.1002/2016GL071368.

Shaw, T. A., & Voigt, A. 2016b. Understanding the Links between Subtropical and Extratropical Circulation Responses to Climate Change Using Aquaplanet Model Simulations. *J. Climate*, **29**, 6637–6657.

Shaw, T. A., Voigt, A., Kang, S. M., & Seo, J. 2015. Response of the intertropical convergence zone to zonally asymmetric subtropical surface forcings. *Geophys. Res. Lett.*, 10.1002/2015GL066027.

Shaw, T. A., Baldwin, M., Barnes, E. A., Caballero, R., Garfinkel, C. I., Hwang, Y.-T., Li, C., O'Gorman, P. A., Rivière, G., Simpson, I. R., & Voigt, A. 2016. Storm track processes and the opposing influences of climate change. *Nature Geosc.*

Shaw, Tiffany A, Barpanda, Pragallva, & Donohoe, Aaron. 2018. A Moist Static Energy Framework for Zonal-Mean Storm-Track Intensity. *J. Atmos. Sci.*, **75**(6), 1979–1994.

Shutts, GJ. 1983. The propagation of eddies in diffluent jetstreams: Eddy vorticity forcing of 'blocking' flow fields. *Quarterly Journal of the Royal Meteorological Society*, **109**(462), 737–761.

Son, S.-W., & Lee, S. 2005. The response of westerly jets to thermal driving in a primitive equation model. *J. Atmos. Sci.*, **62**, 3741–3757.

Son, S.-W., Polvani, L. M., Waugh, D. W., Akiyoshi, H., Garcia, R., Kinnison, D., Pawson, S., Rozanov, E., Shepherd, T. G., & Shibata, K. 2008. The Impact of Stratospheric Ozone Recovery on the Southern Hemisphere Westerly Jet. *Science*, 10.1126/science.1155939.

Stevens, B., Giorgetta, M., Esch, M., Mauritian, T., Crueger, T., Rast, S., Salzmann, M., Schmidt, H., Bader, J., Block, K., Brokopf, R., Fast, I., Kinne, S., Kornblueh, L., Lohmann, U., Pincus, R., Reichler, T., & Roeckner, E. 2013. Atmospheric component of the MPI-M Earth System Model: ECHAM6. *J. Adv. Model. Earth Syst.*, **5**, 146–172.

Swanson, K. L. 2000. Stationary Wave Accumulation and the Generation of Low-Frequency Variability on Zonally Varying Flows. *Journal of the Atmospheric Sciences*, **57**(14), 2262–2280.

Tandon, N. F., Gerber, E. P., Sobel, A. H., & Polvani, L. M. 2013. Understanding Hadley Cell Expansion versus Contraction: Insights from Simplified Models and Implications for Recent Observations. *J. Climate*, **26**, 4304–4321.

Thompson, D. W. J., Solomon, S., Kushner, P. J., England, M. H., Grise, K. M., & Karoly, D. J. 2011. Signatures of the Antarctic ozone hole in Southern Hemisphere surface climate change. *Nature Geosc.*

Tibaldi, Stefano, & Molteni, Franco. 1990. On the operational predictability of blocking. *Tellus A*, **42**(3), 343–365.

Trenberth, K. E., & Stepaniak, D. P. 2003a. Covariability of Components of Poleward Atmospheric Energy Transports on Seasonal and Interannual Timescales. *J. Climate*, **16**, 3692–3705.

Trenberth, K. E., & Stepaniak, D. P. 2003b. Seamless Poleward Atmospheric Energy Transports and Implications for the Hadley Circulation. *J. Climate*, **16**, 3706–3722.

Tung, K. K., & Lindzen, R. S. 1979. A Theory of Stationary Long Waves. Part I: A Simple Theory of Blocking. *Monthly Weather Review*, **107**(6), 714–734.

Vallis, G. K. 2006. Atmospheric and Oceanic Fluid Dynamics Fundamentals and Large-scale Circulation. *Cambridge University Press*.

Vallis, G. K., Colyer, G., Geen, R., Gerber, E., Jucker, M., Maher, P., Paterson, A., Pietschnig, M., Penn, J., & Thomson, S. I. 2018. Isca, v1.0: a framework for the global modelling of the atmospheres of Earth and other planets at varying levels of complexity. *Geoscientific Model Development*, **11**(3), 843–859.

Wang, H., & Ting, M. 1999. Seasonal Cycle of the Climatological Stationary Waves in the NCEP-NCAR Reanalysis. *J. Atmos. Sci.*, **56**, 3892–3919.

Woollings, Tim, Hoskins, Brian, Blackburn, Mike, & Berrisford, Paul. 2008. A New Rossby Wave–Breaking Interpretation of the North Atlantic Oscillation. *Journal of the Atmospheric Sciences*, **65**(2), 609–626.

Woollings, Tim, Hannachi, Abdel, & Hoskins, Brian. 2010. Variability of the North Atlantic eddy-driven jet stream. *Quarterly Journal of the Royal Meteorological Society*, **136**(649), 856–868.

Woollings, Tim, Barriopedro, David, Methven, John, Son, Seok-Woo, Martius, Olivia, Harvey, Ben, Sillmann, Jana, Lupo, Anthony R, & Seneviratne, Sonia. 2018. Blocking and its response to climate change. *Current climate change reports*, **4**(3), 287–300.

Yamada, R., & Pauluis, O. 2016. Momentum balance and Eliassen-Palm flux on moist isentropic surfaces. *J. Atmos. Sci.*, **73**, 1293–1314.

Yin, J. H. 2005. A consistent poleward shift of the storm tracks in simulations of 21st century climate. *Geophy. Res. Lett.*, **32**.

Yuval, Janni, & Kaspi, Yohai. 2018. The relation between the seasonal changes in jet characteristics and the Pacific midwinter minimum in eddy activity. *Geophys. Res. Lett.*, **45**, 9995–10002.